Optical Waveguide Sensor based on Gratings and Metamaterials for Refractive Index Sensing

by

Yixuan Wu

A dissertation submitted to the Graduate Faculty of
Auburn University
in partial fulfillment of the
requirements for the Degree of
Doctor of Philosophy

Auburn, Alabama
August 8, 2020

Keywords: optical waveguide, gratings, metamaterials, biosensor, refractive index

Copyright 2020 by Yixuan Wu

Approved by

Mark L. Adams, Chair, Associate Professor of Electrical and Computer Engineering
Robert Dean, McWane Professor of Electrical and Computer Engineering
Guofu Niu, Alumni Professor of Electrical and Computer Engineering
Stuart Wentworth, Associate Professor of Electrical and Computer Engineering

Abstract

Optical waveguide sensors based on gratings and metamaterials for refractive index (RI) sensing are introduced in this Ph.D. dissertation. A waveguide is a structure which can guide light based on total internal reflection. When a waveguide is applied as an optical sensor, it uses different forms of light–matter interactions to measure or quantify molecules, and be used in biological and chemical applications. A diffraction grating is an optical element with a periodic structure which diffracts incident light into several beam in different directions based on the properties of the light. Metamaterials are engineered materials designed to have properties that do not occur naturally.

In this work, gratings are applied to interact with incident light and to produce changes in the phase and amplitude of the output light. When it is combined with a waveguide, a diffraction grating coupled waveguide based biosensor can be designed. When the light is input with an angle to the biosensor, the grating not only diffracts the light, but allows the light to effectively couple with the waveguide thus providing interaction with the analyte of interest.

A Bragg gratings waveguide (BGW) is a waveguide with periodic structures of RI along the waveguide core. When the light is incident normal to the BGW, the light will be confined to generate a resonance. Two waveguide biosensors based on Bragg gratings are designed. The double sided Bragg gratings waveguide (DSBGW) based biosensor uses Bragg gratings in silicon on insulator (SOI) wafer to measure the target analyte. The light will interact with the gratings and the analyte surrounding the waveguide, and the change of RI of analyte will lead to a change in the resonance peak of the spectrum. Compared with DSBGW, when the waveguide is also coupled with a slot, the double sided Bragg gratings in slot waveguide (DSBGISW) based biosensor is designed and can achieve better performance.

Metal gratings when patterned appropriately can act as a metamaterial. When a liquid-core waveguide and gold/dielectric metamaterial are integrated in the biosensor design, it produces resonance in the waveguide when the light interacts with the metamaterial structure in the core. The sensor is able to detect a liquid analyte by converting the change in the RI of the analyte to a shift of resonance peak in the output spectrum. The different light guiding properties of the structure will determine the peaks in the spectrum and enhance the sensitivity. A metamaterial based biosensor has been characterized through simulation and experimentation.

Acknowledgments

I would like to thank my research advisor Dr. Adams for giving me the opportunity to pursue my Ph.D. degree under his guidance and supervision and supporting my work and personal development. I appreciate his support, encouraging influence and shared vision throughout my years in Auburn. Further, my many thanks goes to my committee members, Dr. Dean, Dr. Niu and Dr. Wentworth for their support. I enjoyed having them as instructors in multiple classes that expanded my knowledge in the technical areas as well. I would also like to express gratitude to Dr Easley as my outside committee member.

My many thanks also goes to Dr. Hamilton, John Sellers and William Baugh for their help in microfabrication. And special thanks to Dr. Peng, Dr. Samani for their valuable input on my project research. I especially would like to give thanks to Tamara Isaacs-Smith, Shiqiang Wang, Vaibhav Gupta, Baha Yakupoglu and Simin Zou for their helping on the operation of lab equipments. My gratitude also extend to my lab-mates, Yuan Meng, Craig Prather, Michael Bolt, Brent Bottenfield, George Hughes, Daylon Hester, for their research support, advice and encouragement.

I would like to thank my brilliant, beautiful and amazing girlfriend, Mengfei Yang, for her constant encouragement and unwavering support, and to my parents Wenwei Yu and Gongyuan Wu, my grandparents Renjie Yu and Luan Gu, for all their selfless love, constant support and sacrifice both financially and emotionally. Words do not do justice to how thankful I am of them.

Table of Contents

List of Figures

List of Tables

List of Abbreviations

AMZI asymmetric Mach-Zehnder Interferometer

ARROW anti-resonant reflecting optical waveguide

BGW Bragg gratings waveguide

BSA bovine serum albumin

CRP C-reactive protein

DGSW double sided grating waveguide

DSBGISW double sided Bragg gratings in slot waveguide

DSBGW double sided Bragg gratings waveguide

EBL e-beam lithography

FFPI fiber-based Fabry-Perot interferometer

FOM figure of merit

FPI Fabry-perot interferometer

FSRS free spectral ranges

GMR Guided mode resonance

IgE immunoglobulin E

IgG Immunoglobulin G

ITO Indium Tin oxide

LMR LMR

LPCVD low pressure chemical vapour deposition

LPFGs long period fiber gratings

LPGs long period gratings

LRSPR long range surface plasmon

MCLW metal clad leaky waveguide

MDGCW microfluidic diffraction grating coupled waveguide

MEMS microelectromechanical systems

MZI Mach-Zehnder interferometer

NC nitrocellulose

PC photonic crystal

PCF photonic crystal fiber

PDMS polydimethylsiloxane

PECVD plasma-enhanced chemical

PMMA polymethyl methacrylate

PSA prostate specific antigen

RCA Radio Corporation of America

RIE reactive ion etching

SMF single-mode fiber

SNR signal to noise ratio

SOI silicon on insulator

SPA staphylococcal protein A

SPR surface plasmon resonance

ssDNA single-stranded DNA

SWGs subwavelength gratings

TE transverse electric

TM transverse magnetic

TMCS trimethylchlorosilane

WGM whispering-gallery

Chapter 1

Introduction

An optical waveguide is a physical structure which can confine the light and guide electromagnetic waves. When the light propagates in a rectangular waveguide, the waveguide can support both transverse electric (TE) and transverse magnetic (TM) modes. The electric field is transverse to the propagation direction in the TE mode while the magnetic field is transverse to the propagation direction in the TM mode. Commonly for a dielectric waveguide, it consists of a high refractive index (RI) medium as the core which is surrounded by a low RI medium as the cladding. A standing wave occurs due to total internal reflection as light propagates through the structure. As shown in Figure 1.1, the RI of the core is n_1 and the RI of the cladding is n_2, with the relation of $n_1 < n_2$. Total internal reflection takes place when θ, the incidence angle, is larger than the critical angle θ_c, which satisfies Eq. (1.1):

$$\sin\theta_c = \frac{n_2}{n_1} \tag{1.1}$$

An evanescent wave is produced when the light propagates into the cladding around the core [23], as shown in Figure 1.2. The intensity of evanescent wave decays exponentially with distance from the interface, which can be represented as Eq. (1.2):

$$I_z = I_i^{-z/d} \tag{1.2}$$

where I_z is the intensity at a perpendicular distance z from the interface, I_i is the intensity at the interface, and d is penetration depth which can be defined by Eq. (1.3), where λ_o is wavelength of incident light in vacuum, n_1 is the RI of the higher refractive index medium

while n_2 represents the lower RI.

$$d = \lambda_o / 4\pi (n_1{}^2 sin^2\theta - n_2{}^2)^{-1/2} \tag{1.3}$$

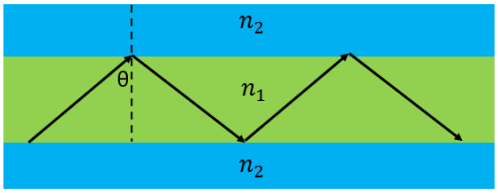

Figure 1.1: An illustration of the basic structure and principle of a dielectric waveguide. The light propagates along the waveguide and is confined in the core by the total internal reflection.

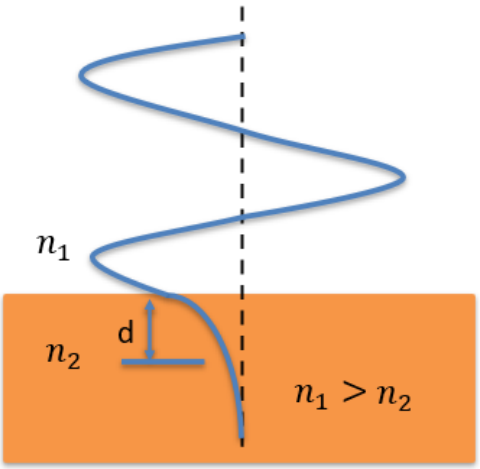

Figure 1.2: An illustration of the evanescent wave profile. The intensity of evanescent wave decays exponentially with distance from the interface of n_1 and n_2. The evanescent wave allows light that propagates in the waveguide to interact with materials outside of the cladding thus providing a sensing mechanism.

In recent decades, optical waveguides have been developed for many promising practical applications and have exhibited exotic physical properties. One of these promising applications is an optical biosensor based on guided waves. A biosensor is a device used for detection of biological and chemical analytes [24]. Biosensors are widely used for applications in health care such as disease detection, environmental testing, food quality control, and pregnancy tests. An optical biosensor using the characteristics of light propagation is

a good alternative to the conventional non-optical analytical devices [25, 26, 27]. It has advantages including high specificity, fast response, and minimal reagent usage. Compared with conventional non-optical devices, it can bring accurate, direct, real-time and label-free results of the detection. A label-free biosensor senses the analyte of interest without introducing a secondary transduction mechanism. Label-free optical biosensing is a powerful method to detect biological elements as the sensing mechanism does not affect the structure of the analyte. Several kinds of such biosensors have been developed, including evanescent waveguide biosensor[1], photonic crystal biosensors [28], and ring resonator biosensors [29], etc. One of the most common measuring schemes is to measure the change of the RI of the target analyte [30, 31]. When the RI is changed by the existence of the analyte of interest, a change in the measured spectrum of the biosensor is observed. By using a well characterized light source, such as a laser or a light emitting diode (LED), the light transmitted from the biosensor contains the RI information of the reagent. Such information is conveyed by the phase shift and the amplitude change of the input light. The sensitivity of the biosensor is directly correlated to the detected spectrum change.

For an optical waveguide biosensor, the sensitivity, the quality factor and the limit of detection (LOD) play important roles in evaluating the sensor's performance. In the detection of biological analytes, bulk sensitivity and surface sensitivity are the two main parameters which describe the performance of the optical biosensor. Bulk sensitivity is determined by either the wavelength shift, phase shift or light intensity divided by the change of bulk RI unit [32]. The surface sensitivity is related to the bulk sensitivity, the decay length of evanescent wave, the resonant slope, and the difference of RI between the surface monolayer and the surrounding environment [33]. It can be calculated by the wavelength shift divided by the thickness of the adhesion layer. Quality factor is a dimensionless parameter to describe the resonance of the optical biosensor. Better resonance of the biosensor will lead to higher observed quality factor. The LOD is defined as the minimum amount of the target analyte present to produce a detectable signal. Optical biosensors are particularly well suited

for non-genetic based assays such as label-free direct assays and labeled fluorescence assays. For label-free assays, the changes detected correspond directly with a physcial or chemical change in the analyte. While in a labeled fluorescence assay, the analyte interacts with a particular fluorophore to produce a highly specific optical signature. The measurements in both categories are related to structure of the sensor and the input light. Chapter 2 is a literature review of optical waveguide biosensors based on RI scheme.

In this work, we simulate a microfluidic diffraction grating coupled waveguide (MDGCW) based biosensor. A diffraction grating is an optical device containing a periodic structure that can divide and diffract light composed of different wavelengths into several beams travelling in different directions. The structure consists of one left grating coupler, one waveguide and one right grating coupler. The light is input from left grating coupler into the waveguide, and then the light will propagate in the waveguide and output from the right grating coupler. The binding layer is formed under the waveguide and its different RI will lead to the different coupling efficiency in grating coupler and different light guiding properties in waveguide. The biosensor performance related to the grating and the binding layer are discussed in Chapter 3. The Bragg gratings, a kind of periodic structure, are built with corrugations on the outside sidewalls of the waveguide. Two optical waveguide bisensors based on Bragg gratings are simulated and fabricated in Chapter 4. DSBGW is a kind of Bragg gratings waveguide that was used to measure the RI analyte around the silicon waveguide. Compared with DSBGW, DSBGISW is designed based on slot waveguide with better resonance. How the parameters of Bragg gratings, waveguide and slot influence the performance of both sensors are discussed. In Chapter 5, a metamaterial / liquid-core waveguide microfluidic optical biosensor is introduced. As the basic structure of this sensor, gold gratings are deposited on a glass wafer to form the metamaterial. The simulation, fabrication and experimental steps are shown in the chapter. RI liquids are measured by the sensor and experimental results are well matched to the simulation with high sensitivity and good repeatability. Chapter 6 is the conclusion of these biosensors for refractive index sensing.

Chapter 2

Literature review

A basic waveguide based optical biosensor uses the interaction of the light confined in the core with the target analyte surrounding the core to obtain the resonance shift of the wavelength in the output spectrum. The basic principle of detection shared by these sensors is based on the propagation of light in the sensor structure. The effective refractive index of the sensor changes as the RI of the measured material in the sensor structure changes. This chapter reviews the basic principle and new developments for the optical waveguide biosensors based on RI sensing. The waveguide biosensors based on interferometers, photonic crystals, ring resonators, gratings, long range surface plasmon resonance and lossy resonance modes are reviewed and discussed in this chapter. Furthermore, the integration of two or three complementary methods in one waveguide biosensor, for instance a ring resonator biosensor based on gratings which brings advantages of the methods to improve the performance of the sensor, is also reviewed.

2.1 Evanescent Waveguide Biosensors

Evanescent waveguide biosensors employ the evanescent wave to detect the interaction between the light and the measured sample. The depth of the evanescent wave into the sample analyte is significant for these sensors [34, 35]. Silicon [36], SU-8 [37], polydimethylsiloxane (PDMS) [38], and Chalcogenide glass [39] have all been used as the core of evanescent waveguide biosensors.

A metal clad leaky waveguide (MCLW) biosensor based on evanescent wave applies nitrocellulose (NC) as an adlayer to immobilize and detect C-reactive protein (CRP). The NC film is fabricated on the sensor surface by spin-coating. The penetration depth is not

significantly influenced by the coated NC film and the sensitivity is decreased by only 9%. The pixel resolution of the sensor achieves 1.35×10^{-4} RIU/pixel and CRP in human serum can be detected in a range of 0.1-10 μg/mL in concentration [40]. Purniawan *et al.* have introduced an evanescent waveguide based on TiO_2 core to detect *Escherichia coli* (*E. coli*) [1]. The schematic of this sensor is shown in Figure 2.1. The TiO_2 waveguide has been fabricated as a freestanding structure by atomic layer deposition to improve its sensitivity and compactness. It is designed to measure the concentrations of isopropyl alcohol and ethanol diluted in water with the sensitivity of 1.34 and 0.85 dB/%(v/v), respectively. Making measurement in several different drain fluids in Luria Broth (LB) medium, the normalized sensitivity is found to be 0.99 per %. As another example, an anti-resonant reflecting optical waveguide (ARROW) has been introduced as an evanescent wave biosensor based on porous silicon to detect the bovine serum albumin (BSA) molecules [41]. ARROW provides better overlap between the light field and the biomolecules attachment since the light is confined in the core which has low RI.

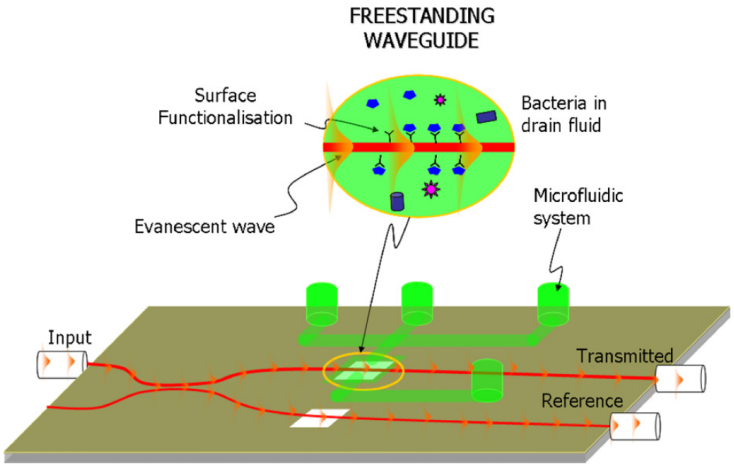

Figure 2.1: A schematic diagram illustrating an evanescent wave coupled sensor based on a TiO_2 core as a freestanding structure to detect *E. coli*. As the *E. coli* binds to the waveguide structure the transmitted light intensity changes. Reprinted from [1] with permission from Elsevier.

Sim *et al.* have introduced a birefringent waveguide which makes use of the evanescent field to detect Listeria monocytogenes at concentrations as low as 10^6 CFU/mL [42]. The

waveguide is fabricated by general integrated circuit processes including lithography, plasma-enhanced chemical vapor deposition (PECVD), RF sputtering, and reactive ion etching (RIE). The sensitivity is optimized by controlling the length of the TiO_2 film, which is overlaid with the waveguide platform. An evanescent waveguide biosensor based on micro-capillaries has been introduced by Liu *et al.* to test specific DNA sequences [43]. The tubing wall in the sensor as the sensing element, which has short length and thin thickness, is spliced between two single-mode fibers to achieve a strong evanescent field. Complementary DNA can be distinguished in the concentrations ranging from 2.5 to 10 μM with a maximum sensitivity of 628.975 nm/RIU.

Rau *et al.* have introduced a biosensor where the evanescent wave from a silicon prism is coupled to a waveguide [44]. A liquid-filled prism coupled metal-clad waveguide has also been reported by Yadav *et al.* [45]. The hollow rectangular prism placed within the aqueous solution behaves as a cavity and the sensitivity can be enhanced to 353.23 °/RIU.

Optical fiber sensors based on evanescent wave also has been widely studied for the detection of biology samples such as cells, foods [46] and viruses [47], etc. Fiber based sensors have been created by depositing a polymer [48] or coating nanostructured material on the fiber [49] to enhance the performance of the sensor. In addition to these structures, a fiber biosensor based on evanescent wave coupling which employs a three-layer structure to improve the evanescent field and to increase penetration depth has been shown [50]. The three-layer sturcture is composed of bottom, interface, and surface layers. The surface layer is made of Canada blasm in xylene doped with GeO_2. The sensor provides a sensitivity of -0.0613/ng/L for Immunoglobulin G (IgG) measurment and an LOD of 0.2 ng/L with high luminous intensity. Another example is a D-shaped step-index fiber optical biosensor based on a four-layer structure which has been designed to measure glucose and IgG by Xin *et al.* [51]. The sensitivity can be -0.077 $(\mu g/L)^{-1}$ when detecting IgG.

Coating nanometer-thick metal oxide films on the fiber core can produce the lossy mode resonance (LMR) effect. The resonance is caused when the light propagates in a thin film

of which the real part of the permittivity is positive and larger in magnitude than its own imaginary part and the real part of the media surrounding the thin film [52, 53]. A D-shaped single-mode fiber (SMF) based on LMR has been introduced by Chiavaioli *et al.* [2], as shown in Figure 2.2. The sensor is is fabricated by coating SnO_2 on the D-shaped SMF through DC sputtering. The LOD can be as low as 0.15 ng/L for detection of IgG. A fiber optical biosensor designed by Tien *et al.* improves the performance by coating TiO_2 nanofilm on the surface of a D-shaped fiber to obtain the LMR can enhance the sensitivity to 4122 nm/RIU [54]. Another group has shown a D-shaped fiber coated with Indium Tin Oxide (ITO) to produce LMR, such that the sensitivity can be increased to 304360 nm/RIU with the resolution of 3.28 $\times 10^{-9}$ [55].

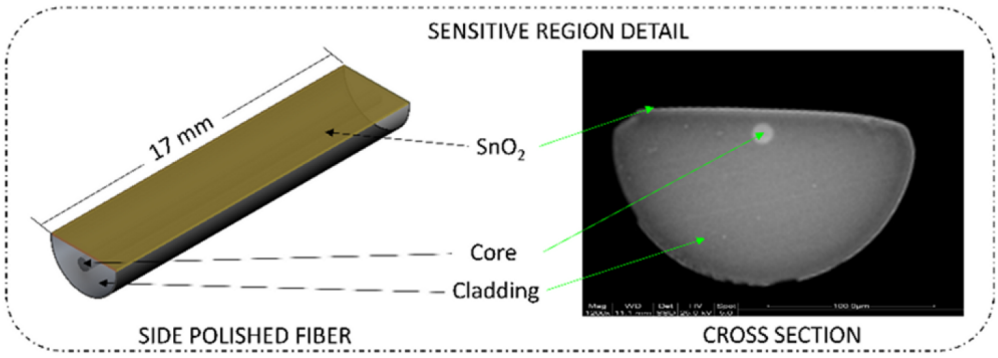

Figure 2.2: Sensitive region of the D-shaped fiber optic biosensor based on a lossy mode resonance effect. A thin film of SnO_2 is deposited on the 17-mm-long side-polished sensitive region by DC sputtering system. Reprinted from [2] with permission from ACS.

The analytes and performance comparison of these evanescent waveguide biosensors mentioned above are summarized chronologically in Table 2.1.

2.2 Surface Plasmon Resonance Waveguide Biosensors

Surface plasmon resonance (SPR) has been originally demonstrated by Otto [56] and Kretschmann *et al.* [57]. SPR-based biosensors have been reported in the literature for many biological applications including food allergens [58] and disease diagnosis [59]. For an SPR sensor, the resonance is produced between a metal film and the surrounding measurable

Table 2.1: Analytes and performance comparison of evanescent waveguide biosensors.

Year	Sample	Sensitivity	LOD	Concentration	Resolution	Ref.
2012	Ethanol, isopropyl alcohol (IPA), and *E. coli*	0.85 dB/%(v/v) for Ethanol 1.34 dB/%(v/v) for IPA	NA	NA	NA	[1]
2012	Phenylethylamine	0.87 dB/(mol L^{-1})	NA	NA	NA	[39]
2012	Listeria monocytogenes	NA	NA	10^{-6} CFU/mL	NA	[42]
2014	CRP	NA	NA	0.1-10 μg/mL	NA	[40]
	& Glycerol	NA	NA	NA	1.35×10^{-4} RIU/pixel	
2015	Glucose	NA	10 nM	NA	NA	[48]
2015	DNA	NA	NA	2.5 to 10 μM	NA	[43]
2016	RI liquid	304360 nm/RIU	3.28×10^{-9}	NA	NA	[55]
2016	IgG	-0.0613/ng/L	0.2 ng/L	NA	NA	[50]
2016	DS-DNA	NA	NA	5-400 μM	NA	[49]
	& ATP	NA	NA	5–200 μM	NA	
2017	IgG & glucose	-0.077 $(\mu g/L)^{-1}$	NA	NA	NA	[51]
2017	CRP	NA	0.0625 mg/L	NA	NA	[53]
2018	RI liquid	4122 nm/RIU	NA	NA	NA	[54]
2018	RI liquid	353.23 °/RIU	NA	NA	NA	[45]
2018	IgG	NA	0.15 ng/L	NA	NA	[2]
2018	*E. coli*	NA	NA	10^2 CFU/mL	NA	[37]
2019	RI liquid	NA	NA	NA	7×10^{-6}	[38]

target. The basic principle of an SPR sensor is based on the change in the RI of target [60]. A simple SPR biosensor is made up of only one dielectric film and a single metal layer. Compared with SPR, long range surface plasmon resonance (LRSPR), which can be seen as SPR based on waveguide, is produced when the light is excited in a metastructure consisting of a metal layer as the core and two surrounding optically semi-infinite dielectric layers, so that the light can propagate over an appreciable length [3]. The basic LRSPR structure and its supporting modes are illustrated in Figure 2.3, where $\varepsilon_{r,2}$ is the relative permittivity of metal, and $\varepsilon_{r,1}$ and $\varepsilon_{r,3}$ are relative permittivities of the dielectric media around the metal. To match the RI of the biologically compatible analyte of the sensor, Teflon [61, 62], CYTOP [63, 64, 65, 66] or ppPFOE [67] can be used as the dielectric layers to sandwich the metal with the measurable medium.

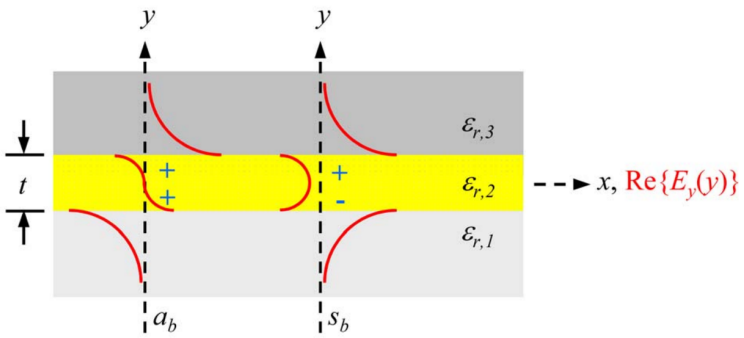

Figure 2.3: A schematic diagram of a metal slab consisting of a thin metal film (yellow) of thickness t and relative permittivity $\varepsilon_{r,2}$ bounded by optically semi-infinite dielectrics (claddings, grey) of relative permittivities $\varepsilon_{r,1}$ and $\varepsilon_{r,3}$ (asymmetric mode a_b when $\varepsilon_{r,1} > \varepsilon_{r,3}$ or $\varepsilon_{r,1} < \varepsilon_{r,3}$; symetric mode s_b when $\varepsilon_{r,1} = \varepsilon_{r,3}$) which are necessary to support the long range surface plasmon resonance mode. Mode propagation occurs along the +z axis (perpendicular up from the page). Reprinted from [3] with permission from OSA.

An LRSPR optical biosensor coated with gold and embedded in CYTOP, as shown in Figure 2.4, applies direct and sandwich assays to detect human cardiac troponin I (cTnI) protein with the LODs of 430 pg/mL and 28 pg/mL, respectively [4]. Another LPSPR optical biosensor to detect human red blood cells has been introduced by Krupin *et al.* [68]. The detection of cells bearing A-antigen (A and AB red blood cells) has been verified and the LOD of A red blood cells can be lower than 3×10^{-5} cells/mL. With the help of enzyme-linked immunosorbent assay, an LRSPR biosensor based on CYTOP can be designed to measure non-structural 1 (NS1) protein, which is one of the most important proteins of Dengue virus [69]. The LOD can reach 5.73 pg/mm^2.

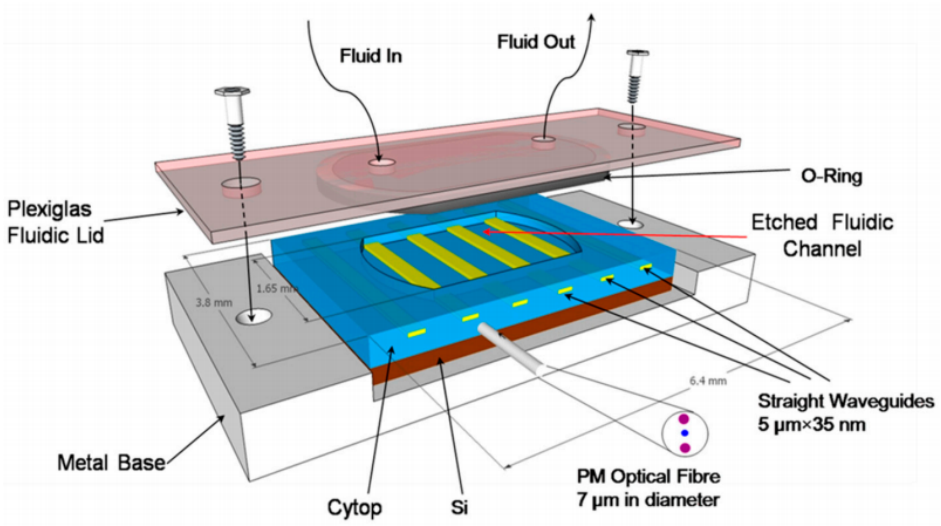

Figure 2.4: A schematic diagram of an LPSPR optical biosensor on a metal base with a fluidic channel. A fluidic cavity is obtained by etching the top CYTOP down to the gold strips. Reprinted from [4] with permission from MDPI.

To address the problem that the RI of the tested analyte must be close to the RI of the dielectric layer, a symmetrical LRSPR biosensor based on MgF_2/Au/MgF_2/analyte structure has been presented by Shi *et al*. [70]. The MgF_2 film is deposited by evaporation and the gold film is deposited by magnetron sputtering system. The sensitivities of the sensor in the fluid analyte and in the air are 5.5×10^5 pixels/RIU and 2.3×10^5 pixels/RIU, respectively, while the LODs are 8.1×10^{-8} RIU and 3.5×10^{-7} RIU, respectively. The system demonstrates an LOD of *E. coli* of 103 CFU/mL.

LRSPR can also be applied in the fiber sensor application. An LRSPR optical biosensor based on hollow fiber (HF) has been introduced by Jiang *et al*. [5]. As shown in the schematic diagram in Figure 2.5, the dielectric layer (OC300) is coated on the silver layer inside the supporting tube and the core of fiber is used as the sensing medium. Employing the methods of chemical deposition and liquid-phase coating, LRSPR is supported in the structure of cladding layer-silver layer-delectric layer. The figure of merit (FOM) of the sensor can be enhanced to 78 RIU^{-1} on average. The sensitivity reaches more than 4500 nm/RIU. Another LRSPR side-polished fiber optical biosensor is designed to measure BSA by coating with

MgF_2 and silver film which enhances the concentration sensitivity to 0.765 nm/(mg/mL) [71].

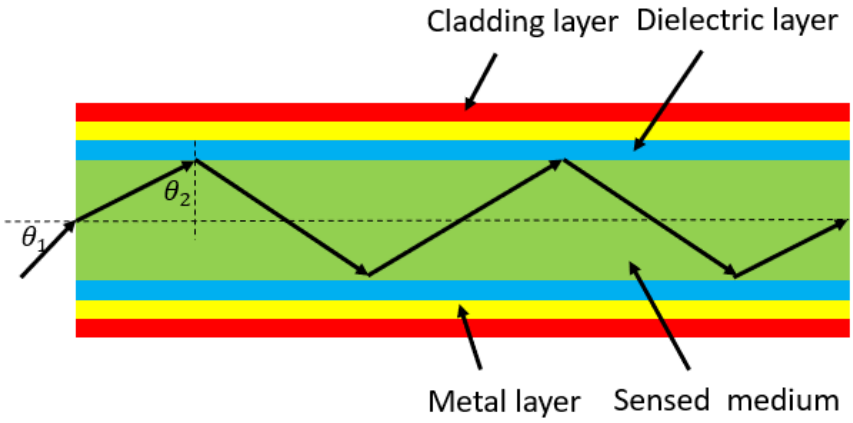

Figure 2.5: A schematic diagram of an LRSPR sensor based on hollow fiber. A metal layer (silver here) is deposited on the inner surface of the cladding and a dielectric layer is coated on inner surface of the metal layer. The LRSPR is supported in the dielectric/metal/cladding layer and analytes are sensed through the core. Reproduced from [5] with permission from OSA.

The analytes and performance comparison of these SPR-based waveguide biosensors mentioned above are summarized chronologically in Table 2.2.

2.3 Grating Coupler Biosensors

Grating couplers are common optical components for introducing light into on-chip photonic structures and were initially presented by Dakss *et al.* [72]. They are used extensively for optical interconnections and especially for optical device integration. A classical optical grating structure is made of periodic slits in an opaque medium. Each slit is regarded as an independent source of light which interferes with one another to generate the classical diffraction pattern. A binary grating, used as a basic coupling structure, consisting of an array of narrow periodic thin rectangular ridges of alternating RI. Mathematically this effect can be described by (2.1) for reflection and transmission:

$$d(n_t \sin \psi_t - n_i \sin \psi_i) = m\lambda \tag{2.1}$$

Table 2.2: Analytes and performance comparison of SPR-based waveguide biosensors.

Year	Sample	Sensitivity	LOD	FOM	Ref.
2007	RI liquid	NA	2.5×10^{-8}	NA	[61]
2009	RI liquid	59000 nm/RIU	NA	NA	[62]
	and *E. coli* HB101P	λ shift: 5.5 nm	NA	NA	
2013	RI liquid	NA	2.3×10^{-6} RIU for RI	NA	[64]
	and red blood cell	NA	12 pg/mm^2 for BSA	NA	
2013	RI liquid	NA	3.5×10^{-7} for RI	NA	[70]
	and *E. coli*	NA	103 CFU/mL for *E. coli*	NA	
2014	Red blood cell	NA	$< 3\times10^{-5}$ cells/mL	NA	[68]
2015	RI liquid	NA	NA	92.3 RIU^{-1}	[67]
2015	RI liquid	NA	NA	78 RIU^{-1}	[5]
2016	Non-structural 1 protein	NA	5.73 pg/mm^2	NA	[69]
2018	BSA	NA	2×10^{-3} for RI	NA	[65]
2018	BSA	NA	10 pg/mL	NA	[66]
2019	BSA	0.765 nm/(mg/mL)	NA	NA	[71]
2019	Human cardiac troponin I (cTnI) protein	NA	430 pg/mL for direct assay 28 pg/mL for sandwich assay	NA	[4]

where d is the grating period, n_t is the refractive index of the transmitted medium and n_i is the refractive index of the incidence medium. λ is the wavelength of the light, ψ_i is the coupling angle, and ψ_t is the angle that the light propagates in the grating coupler.

A grating coupler biosensor is a structure that combines a grating coupler with a waveguide to test bio-analytes, such as protein [73] and bacteria [74]. When the analyte is bonded to the structure, the effective index of the structure is changed and will influence the mode of the light coupled and guided.

Guided mode resonance (GMR) is a resonance phenomenon taking place when a diffracted order of grating excites a guided mode of a waveguide that again couples out of the waveguide and interferes with the zeroth order reflected light [75, 76]. A waveguide grating biosensor based on angle interrogation of microelectromechanical systems (MEMS) mirror can achieve an LOD of 2.5 nM for the detection of goat-anti-mouse IgG [77]. The grating has been fabricated by interference lithography and dry etching into the substrate by RIE. Compared with the biosensor based on SOI, cores of porous silicon [78], Ta_2O_5 [79], and polymer gratings [80] have also been demonstrated. Mizutani *et al*. have introduced a grating waveguide

sensor based on gold film [80]. The gold film acts as a mirror and the light is fully reflected by the structure when phase matching occurs. A double-sided grating waveguide (DGSW) biosensor based on sub-surface cavities has been introduced by Li *et al.* [81]. An injection molding process was used to transfer gratings onto a polymer substrate and the TiO_2 waveguide layer was sputtered onto the patterned substrate to form the DGSW struture. The structure of double-sided grating can support varied coupling angles and positions without affecting detection sensitivity. A camera system incorporating multi-LED systems and a grating sensor based on GMR has been reported to detect the CD40 ligand antibody with the system LOD of 168 pM (24 ng/mL) [82]. Another GMR waveguide biosensor compatible with CMOS camera based on chirped gratings can achieve the RI sensitivity of 137 nm/RIU and the LOD of 267 pM to test IgG [83].

Subwavelegnth gratings (SWGs) are a kind of metamaterial which can be employed on biosensors to enhance the performance. With the help of traditional electron-beam lithography techniques, an optical biosensor based on SWGs and waveguide has been introduced by Takashima *et al.* [84]. In such a sensor, the incidence light is normal to the waveguide and the SWGs excite the modes to produce dual resonance peaks to detect the target analyte. The sensor can obtain a RI resolution of 7.65×10^{-4}.

A slot waveguide biosensor based on phase-shifted Bragg gratings has been demonstrated by Wang *et al.* [6], with a modified sandwich assay shown in Figure 2.6. The light is concentrated in the low-index slot to increase the field overlap with the sensing medium. Bragg gratings are used to improved the quality factor. The sensor, which is compatible with standard CMOS fabrication, is realized by 193-nm deep-ultraviolet lithography and dry etching. With this structure, a sensitivity can be achieved at 340 nm/RIU with the qualtify factor of 1.5×10^{-4}.

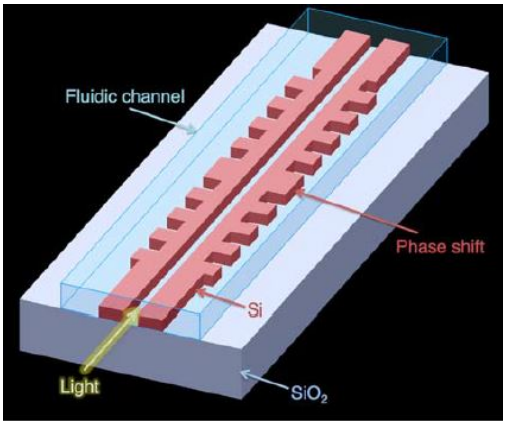

Figure 2.6: A schematic diagram of the silicon photonic biosensor integrated with microfluidic channel. The Bragg grating is on the sidewalls of the slot waveguide and a phase shift is formed in the middle of the gratings. The grating structure helps improve the quality factor thus enhancing the sensitivity. Reprinted from [6] with permission from Wiley-VCH.

Furthermore, grating structures can be also applied in the liquid core waveguide sensor [85]. The metal gratings inside the waveguide can lead to the change of guiding properties of the waveguide for TE mode light and obtain the sensitivity greater than 1280 nm/RIU.

Biosensors based on optical fiber with gratings have also been developed in recent years [86]. The gratings in the fiber can be Bragg gratings [87], long period gratings [88], and tilted gratings [89], etc. Bragg gratings can be fabricated by laser inscription [90] or UV inscription [91]. They can provide high accuracy, good stability and small sizes. An optical biosensor based on etched fiber Bragg gratings obtains a bulk sensitivity of 17.4 nm/RIU and the detection of Thrombin has been verified [92]. Another fiber biosensor based on bare fiber Bragg grattings has been introduced by Srinivasan *et al.* [7], as shown in Figure 2.7. After functionlization, anti-*E. coli* antibody is immobilized on the surface of the bare fiber. The binding of *E. coli* can result in a 25-pM wavelength shift.

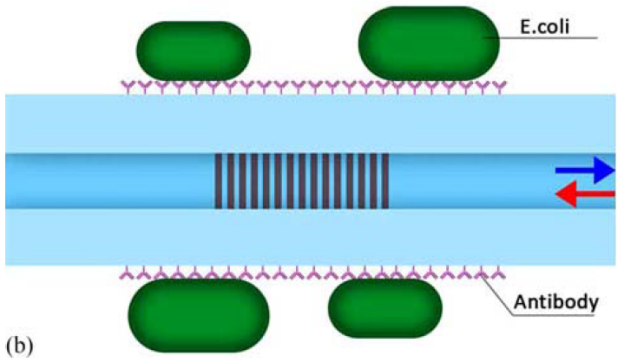

Figure 2.7: A schematic diagram of the grating region after antibody immobilization and *E. coli* binding on the bare fiber Bragg grating biosensor. *E. coli* binding shifts the output spectrum of the transmitted light proportional to the amount of binding. Reprinted from [7] with permission from Wiley-VCH.

Optical biosensors based on long period fiber gratings (LPFGs) rely on long period gratings (LPGs) to enhance the light coupling between the core mode and cladding modes [86, 88]. Coating films such as silica core gold shell nanoparticles [93] or employing glucose oxidase (GOx) encapsulated zeolitic imidazole framework [94] have shown performance improvement of the biosensor. Both examples are able to increase the surface area exposed to the analytes. An optical fiber biosensor based on LPGs to measure biotinylated Bovine Serum Albumin has been developed by Esposito *et al.* [95]. Coated with Polycarbonate and Graphene Oxide film, the sensor obtains an LOD of lower than 0.2 aM for detection of BSA. Another optical biosensor based on LPGs has been developed by Chiavaioli *et al.* [8], as shown in Figure 2.8. The LPGs are fabricated in a SMF utilizing a point-to-point inscription with the help of a KrF pulsed Excimer laser. Through coating solgel-based titania-silica thin film and carrying out an IgG/anti-IgG assay, an LOD of 8 μg/L is achieved.

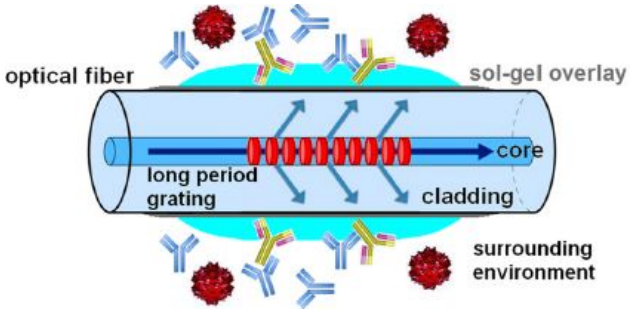

Figure 2.8: A schematic diagram of the grating region after an assay binding process for an LPFGs-based biosensor. A Sol-gel film is coated on the surface of the fiber to allow analyte binding. Reprinted from [8] with permission from ACS.

When the gratings in the fiber are tilted, the light is guided by the cladding mode instead of core mode with narrow band spectral resonances. By tilting the gratings, additional surface area is exposed for functionalization to increase binding sites thus improving the sensitivity. The tilted fiber grating is fabricated by UV inscription with a scanning phase-mask [96]. The sensitivity can also be improved by coating metal films on the gratings which increases the resonance for a fiber biosensor [97]. An optical fiber sensor based on tilted fiber gratings has been described by Guo *et al.* to measure urinary protein variations [98]. By coating silver film on surface to excite a slightly weakened SPR and to excite the cladding mode to tunnel near cut-off, the sensitivity of protein concentration is 5.5 dB/(mg/mL) while the LOD is 1.5×10^{-3} mg/mL.

The analytes and performance comparison of these grating coupler biosensors mentioned above are summarized chronologically in Table 2.3.

2.4 Interferometers

2.4.1 Mach-Zehnder Interferometers (MZI)

An interferometer is a measurement tool consisting of two distinct optical paths or arms in which the light passing through the arms is recombined to produce an interference pattern. A common interferometer is the Mach-Zehnder interferometer (MZI) in which the light source is split into two beams which travel along a test path and a control path, respectively. The

Table 2.3: Analytes and performance comparison of grating coupler biosensors.

Year	Sample	Sensitivity	LOD	Resolution	Concentration	Ref.
2009	RI	110 nm/RIU	NA	NA	NA	[76]
	and Streptavidin	λ shift: 1 nm	NA	NA	NA	
2011	IgG	1 pg/mm^2	NA	NA	NA	[79]
2011	3-APTES,	1090 nm/RIU	NA	NA	NA	[78]
	DNA and PNA	NA	1 μm for PNA	NA	NA	
2013	RI and biological	340 nm/RIU	NA	NA	NA	[6]
	sandwich assay	λ shift: 4 nm	NA	NA	NA	
2014	*E. coli* outer membranes proteins	NA	NA	NA	0.1-10 nM	[88]
2014	Human acute leukemia cells	180 nm/RIU	2×10^{-5}	NA	NA	[99]
2015	RI liquid, DNP /	NA	NA	5.3×10^{-6}	NA	[81]
	anti-DNP interaction	NA	7.81×10^{-8} g/mL	/RIU	NA	
2015	RI liquid and IgG	NA	8 μg/L	NA	NA	[8]
2015	C-reactive protein	NA	0.01 mg/L	NA	NA	[87]
2016	IgG	NA	2.5 nM	NA	NA	[77]
2016	Urinary protein	5.5 dB/(mg/mL)	1.5×10^{-3} mg/mL	NA	NA	[98]
2016	CK7 peptidets	NA	0.4 nM	NA	NA	[97]
2016	Streptavidin	6.9 nm/(ng/mm^2)	19 pg/mm^2	NA	NA	[93]
2017	RI liquid	0.608π phase shift per 10^{-4} RI change	NA	NA	NA	[75]
2017	RI liquid	16 nm/RIU	NA	NA	NA	[90]
2017	RI liquid and IgG	137 nm/RIU	267 pM for IgG	NA	NA	[83]
2017	*E. coli*	λ shift: 25 pM	NA	NA	NA	[7]
2017	CD40 ligand	NA	168 pM	NA	NA	[82]
2018	RI	17.4 nm/RIU	NA	NA	NA	[92]
	and Thrombin	NA	NA	NA	19-80 nM	
2018	Glucose	0.24 nm/mM	NA	NA	0-8 mM	[96]
2018	BSA	NA	$<$ 0.2 aM	NA	0.1–1000 aM	[95]
2019	RI liquid	NA	NA	7.65×10^{-4}	NA	[84]
2019	Glucose	0.5 nm/mM	NA	NA	NA	[94]

light is then recombined to produce a phase shift at the detector [100, 101]. A basic MZI biosensor based on a Y coupled waveguides has a measure arm and a reference arm to test the phase shift, as shown in Figure 2.9 [9]. The phase shift can be described by (2.2):

$$\triangle\phi = \frac{2\pi}{\lambda} \triangle N_{eff} L \tag{2.2}$$

where λ is the wavelength of the input light, N_{eff} is the effective RI of the propagating mode and L is length of the sensitive window. The phase difference between the two arms results in the interference effect. MZI biosensors typically functionalize the measure arm to bind the analyte of interest. The phase shift changes with different analytes such as protein [102], bacteria [103], and toxin [104]. MZI devices can be fabricated with SOI [105], CMOS-compatible Si_3N_4 [106][107], polymers [108], organic-inorganic films [109], and liquid core waveguides [110]. The design of an MZI sensor based on broad band illumination is another approach to enhance the performance [111, 112]. In the broad-band MZI sensor, the light propagating in the sensor has two modulated polarization characteristic sinusoids which can be deconvoluted [113]. A broad-band MZI sensor has been introduce by Psarouli *et al.* [10], in which the integration of LED device and MZI interferometer is shown in Figure 2.10. Through dual polarization analysis with a broad-band input light and an modulated output light, this sensor can be used to detect mouse IgG, BSA and biotinylated-BSA by phase shift. MZI sensitivity can further be enhanced by combining the MZi structure with a slot waveguide [114]. Its oxide layer and Si_3N_4 layer were deposited by plasma-enhanced chemical vapour deposition (PECVD) and low pressure chemical vapour deposition (LPCVD), and its slot was created by the reactive ion etching (RIE) process. An MZI optical biosensor based on a double-slot hybrid-plasmonic waveguide as the sensing area has achieved the sensitivity of 1061 nm/RIU [115]. Cascaded MZI devices have also been studied recently. An optical biosensor based on cascaded MZI has been developed by Bhardwaj *et al.* [116]. The sensor detects glucose with the RI ranging from 1.333 to 1.349 with the sensitivity of 380 nm/RIU. When a reference MZI is cascaded after a sensing MZI based on slot waveguide, the surface sensitivity is enhanced to 60 nm/(ngmm^{-2}) and the LOD is 0.155 (pgmm^{-2}) utilizing the Vernier effect [117].

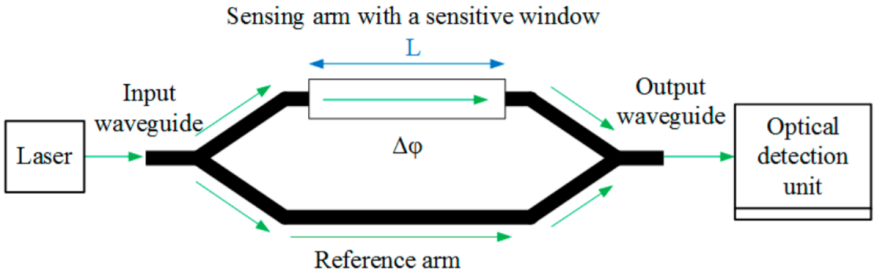

Figure 2.9: A schematic diagram of a basic Mach-Zehnder interferometer (MZI) sensor based on waveguide. The interference pattern at the optical detection unit changes as light in the sensing window interacts with the analyte of interest. Reprinted from [9] with permission from MDPI.

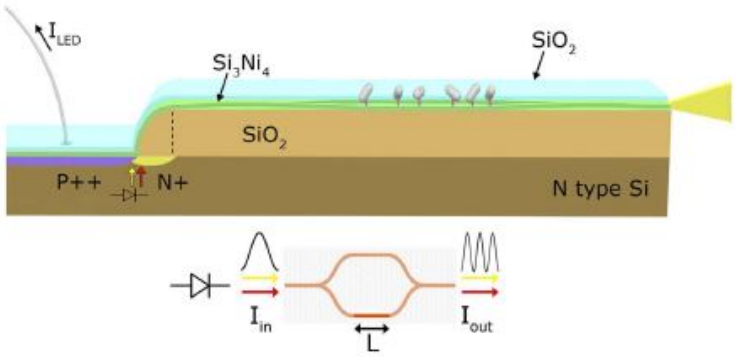

Figure 2.10: A schematic diagram of the integration of a avalanche-type LED device, a MZI and a silicon nitride rib waveguide. The image underneath shows the photonic diagram that illustrates the influence of the analyte on the the output light. As analyte binds to the sensing arm the interference pattern changes at the output. Reprinted from [10] with permission from Nature Publishing Group.

Compared with traditional MZI biosensors, asymmetric Mach-Zehnder Interferometer (AMZI) biosensors have different Y couplers and different lengths of waveguides, which allows for easier fabrication and functionalization [118, 119]. When a thin film composed of polytetrafluoroethylene (PTFE) and Ta_2O_5 is deposited on the surface of the AMZI by ion beam sputtering, the sensitivity factor is enhanced and the LOD is around 10^{-3} RIU [120]. Another AMZI has been developed by Chalyan *et al.* [121]. In this sensor, the asymmetry is achieved by adding a small path in reference arm with the sensitivity of 10^4 rad/RIU. Aflatoxin M1 (AFM1) detection has been verified with this design. Furthermore, a optical

biosenosr based on a three-port interferometer has achieved the sensitivity of 13051 rad/RIU with an LOD of 2.76×10^{-8} RIU [122].

When an MZI biosensor is based on optical fiber, it usually offers high sensitivity and ease of fabrication [123]. An fiber-based MZI has been designed by Li *et al.* [124]. By using femtosecond laser beam to inscript the localized regions and using HF solution to etch the laser-modified regions to enhance the interaction of the tested analytes with the core light, the sensor achieves the sensitivity of -10055 nm/RIU with an LOD of 3.5×10^{-5} RIU for RI liquid detection, and the sensitivity of -38.9 nm/(mg/mL) with an LOD of 2.57×10^{-4} mg/mL for BSA solution. A fiber-based MZI biosensor has been introduced by Wang *et al.* [125] in which one single mode fiber is spliced into two segments of single mode fibers with large core-offset. The bulk sensitivity can reach 13936 nm/RIU for salt solutions and the LOD is 47 ng/ml for human-IgG. Another MZI sensor has been designed by tapering a single mode fiber [11], as shown in Figure 2.11. The down-tapered region can excite a few leaky modes that interfere with the core mode at the upper-taper region, achieving a sensitivity of 4234 nm/RIU in the RI range from 1.4204 to 1.4408.

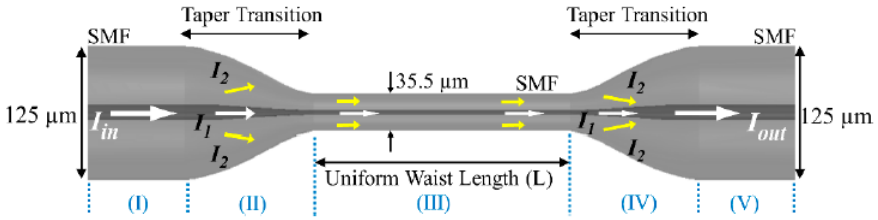

Figure 2.11: A schematic diagram of the internal structure of an MZI biosensor based on long uniform tapering technique. A few leaky modes can be excited in the tapered region which interfere with the core mode providing a simple, self-contained sensing mechanism. Reprinted from [11] with permission from MDPI.

Different types of optical fiber spliced into two fibers are also reported, such as S-shaped fiber [126], no-core fiber [127], and a fiber based on seven-cores with a ball symmetrical structure [128]. Besides the shapes of the fiber, different shapes of cavity also influence the performance of the MZI fiber sensors, such as U-shaped cavity [129], V-shaped cavity and

rectangular-shaped cavity [130], which can all be fabricated using a femtosecond laser. The sensor based on rectangular-shaped cavity has the sensitivity of -17503.73 nm/RIU, since its remaining fiber core has smaller effective RI.

The analytes and performance comparison of these MZI biosensors mentioned above are summarized chronologically in Table 2.4.

2.4.2 Fabry-Perot, Sagnac and Bimodal Interferometers

A Fabry-Perot interferometer (FPI) consists of two reflectors and can be seen as a resonator where the coupled light is reflected in the cavity to produce resonance, as illustrated in Figure 2.12. The path difference δ is defined as

$$\delta = (2\pi/\lambda)2nl\cos\theta \tag{2.3}$$

where l is the length of the cavity, λ is the wavelength, n is the RI of the cavity, and θ is the incident angle of the light, and the path difference is an integral number of the wavelength for maximum transmission. A fiber-based Fabry-Perot interferometer (FFPI) sensor has been shown by creating a micro-cavity with end faces of high reflectance onto a optical fiber [131]. In the application of FFPI biosensor, the phase of the interference in the fiber is proportional to the optical length which is related to the micro-cavity length and the RI of the measured analyte [132].

Table 2.4: Analytes and performance comparison of MZI biosensors.

Year	Sample	Sensitivity	LOD	Resolution	Concentration	Ref.
2008	RI liquid	NA	NA	$> 4\times10^{-6}$	NA	[110]
2012	RI liquid	1730 2π/RIU	1.29 $\times10^{-5}$ ng/mL	NA	NA	[117]
	and PSS/PAH	7.16 nm/ngmm^2	1.3 pgmm^2	NA	NA	
2013	RI liquid,	1864π RIU	NA	NA	NA	[114]
	Streptavidin,	1 pg/mL	NA	NA	NA	
	and methylation	NA	NA	NA	$>$ 1 nM	
	of DAPK gene					
2014	RI liquid	20 μm/RIU	10^{-6}-10^{-7} RIU	NA	NA	[112]
2014	RI liquid	1100 nm/RIU	1.8×10^{-6}	NA	NA	[126]
2014	RI liquid, IgG	592 rad/RIU	10^{-5} RIU	NA	NA	[119]
	and BSA					
2014	RI liquid	1500 nm/RIU	NA	NA	NA	[102]
	and gelatin	2.42141 nm/%W/V	NA	NA	NA	
2015	S-protein /	NA	NA	NA	$>$ 3 ng/mL	[106]
	peptide interaction					
2015	IgG	NA	NA	NA	0.025-66.7 nM	[10]
	and BSA	NA	32 pM for TE 40 pM for TM	NA	NA	
2015	IPA solution	1061 nm/RIU	NA	NA	NA	[115]
2016	RI liquid	-17503.73 nm/RIU	NA	NA	NA	[130]
2016	Glucose solution	NA	0.003 RIU	NA	NA	[108]
2016	Glucose solution	NA	10^{-5} RIU	NA	NA	[118]
2016	Glucose solution	380 nm/RIU	NA	NA	NA	[116]
2016	Glucose solution	10^3 rad/RIU	5×10^{-7} RIU	NA	NA	[121]
	and Aflatoxin M1					
2016	ssDNA	NA	0.0001 pM/μL	NA	NA	[129]
2017	Glucose solution	NA	10^{-3} RIU	NA	NA	[120]
2017	RI liquid	160 nm/RIU	2.8×10^{-6} RIU	NA	NA	[105]
2017	RI liquid	13051 rad/RIU	2.76×10^{-8} RIU	NA	NA	[122]
2017	RI liquid	-10,055 nm/RIU	3.5×10^{-5} RIU	NA	NA	[124]
	and BSA	-38.9 nm/(mg/mL)	2.57×10^{-4} mg/mL	NA	NA	
2017	C-reactive protein	NA	2.1 ng/mL	NA	NA	[111]
2018	RI liquid	$>$ 10000 nm/RIU	NA	NA	NA	[127]
2018	RI liquid	82.7 nm/RIU	NA	NA	NA	[123]
	and IgG	10.4 nm/(mg/mL)	NA	NA	NA	
2018	RI liquid	13936 nm/RIU	NA	1.44×10^{-6}	NA	[125]
	and IgG	NA	47 ng/mL	NA	NA	
2018	RI liquid	15000 nm/RIU	NA	NA	NA	[103]
	and *E. coli* C3000	NA	100 CFU/mL	NA	NA	
2018	RI liquid	5200 rad/RIU	0.01 ng/mL	NA	NA	[104]
	and ochratoxin A					
2018	*E. coli* solution	2×10^{-4}	20 pg/mm^{-3}	NA	NA	[109]
2019	RI liquid	4234 nm/RIU	NA	NA	NA	[11]

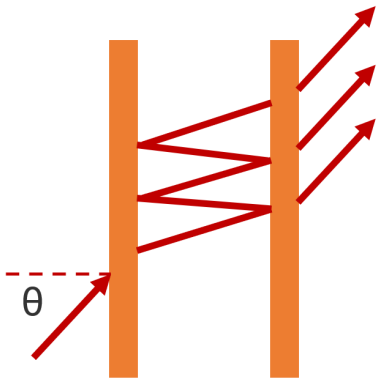

Figure 2.12: A Fabry-Perot etalon is formed by placing two reflectors a precise distance apart. Light waves can only pass through the cavity when they are in resonance with it. This filtering property forms the basis for numerous sensors.

An Fiber-Optic Fabry-Perot interferometer based sensor has been introduced by Li *et al.* [12], as shown in Figure 2.13. A sensitivity greater than 1160 nm/RIU has been demonstrated by using sputtering system to coat gold film on an open micro-cavity to produce a total-reflection mirror. Furthermore, additional biosensors based on various optical fiber structures have been reported in recent years including sandwiching a silica tube by two fibers [133], producing a small cavity on a single mode fiber by focused ion beam milling [134], inserting a cavity with a lateral offset [135] and drilling a micro-hole in the fiber [136]. Compared with conventional FPI biosensors, Xu *et al.* have implemented a tiny segment of capillary tube into two segments of single mode fibers to produce a cascaded FPI with three reflecting surfaces [137]. The reflected intensity is monitored by this sensor which has achieved the sensitivity of 216.37 dB/RIU. The Vernier effect is applied in FPI to enhance the free spectral range as well. With this sensor system combining the sensing FPI with a reference FP etalon, the Vernier effect is produced by the slight difference in the free spectral ranges (FSRs) of the two FPIs [138]. The wavelength sensitivity of 23794.6 nm/RIU is reported with 4602.3 dB/RIU intensity sensitivity.

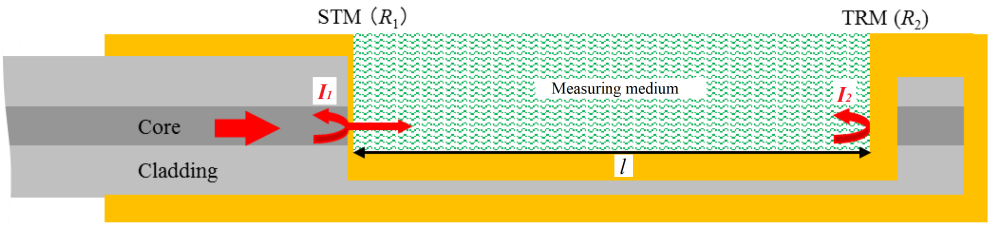

Figure 2.13: A schematic diagram of the Fiber-Optic Fabry-Perot interferometer sensor, showing sputtered gold films on the inner surfaces of the micro-cavity. The gold films are used as both a semi-transparent mirror (STM) and a total-reflection mirror (TRM). The optical cavity created by the two mirrors greatly enhances the sesnivity of the device. Reproduced from [12] with permission from MDPI.

Sagnac interference is a phenomenon in which light is split into two beams that counter propagate in a loop to generate interference at the output [139]. Sagnac interference can be applied to a fiber optic biosensor in the form of Sagnac loop interferometer [140]. The polarimetric interference is produced when the light propagates in an elliptical high birefringence microfiber. The detection of single-stranded DNA (ssDNA) has been verified with a minimum detectable concentration at 75 pM while the bulk sensitivity of 13488 nm/RIU has been achieved [141]. When the Sagnanc interference biosensor is used with the Vernier effect, BSA can be detected with sensitivity of 0.097 nm/(mg$\times$mL^{-1}) [142].

A microfiber tapered interferometer employs the fiber's first two propagation modes to generate the interference pattern in the taper waist region [143, 144]. It can be applied to detect IgG. Huang *et al*. have introduced a DNA biosensor based on microfiber tapered interferometer coated by conjugated polymer membranes [145]. The fundamental mode and a higher order mode are excited in the taper region leading to the sensitivity of 2.393 nm/log M. A biosensor based on a tapered interferometer can be fabricated by heating and stretching a section of a highly Ge-doped fiber with the help of a flame-brush and can obtain a sensitivity of 11006 nm/RIU [146].

The interference of the light caused by two different modes in a bimodal waveguide produces the phase difference in the output light [147]. UV lithography [148] and UV-based soft imprint techniques [149] have been used to fabricate the bimodal waveguide. Besides the

Table 2.5: Analytes and performance comparison of Fabry-Perot, Sagnac and bimodal interferometers.

Year	Sample	Sensitivity	LOD	Resolution	Concentration	Ref.
2011	RI liquid and BSA	NA	2.5×10^{-7} RIU	NA	NA	[149]
2011	IgG	λ shift: 1.5 nm	NA	NA	NA	[143]
2012	RI liquid	~994 nm/RIU	NA	NA	NA	[136]
2013	RI liquid	1051 nm/RIU	NA	NA	NA	[133]
2015	RI liquid	19212.5 nm/RIU	NA	NA	NA	[144]
2015	Single-stranded DNA	2.393 nm/log M	10^{-10} M	NA	NA	[145]
2016	RI liquid	1086 nm/RIU	NA	NA	NA	[135]
2016	RI liquid	$>$ 1160 nm/RIU	NA	$>1\times10^{-6}$	NA	[12]
2016	Bacillus cereus and *E. coli*	NA	NA	NA	$>$ 40 CFU/mL	[150]
2017	RI liquid	~216.37 dB/RIU	NA	NA	NA	[137]
2017	RI liquid	457 nm/RIU	NA	NA	NA	[134]
2017	RI liquid	13488 nm/RIU	NA	NA	NA	[141]
	and ssDNA	NA	NA	NA	$>$ 75 pM	
2018	RI liquid	2429 nm/RIU	NA	NA	NA	[142]
	and BSA	0.097 nm/(mg$\times$mL^{-1})	NA	NA	NA	
2018	RI liquid,	-3137 nm/RIU	NA	NA	NA	[140]
	biotin,	λ shift: 12 nm	NA	NA	NA	
	and streptavidin	λ shift: 5 nm	NA	NA	NA	
2018	RI liquid	23794.6 nm/RIU	NA	NA	NA	[138]
2018	IgG	NA	0.2 mg/L	NA	NA	[151]
2019	RI liquid	316π rad/RIU	NA	NA	NA	[148]

standard silicon technology [149] and the polymer core waveguide [148], a bimodal wavguide biosensor based on S_3N_4 has been introduced by Maldonado *et al.* [150]. The waveguide has S_3N_4 as the core which is covered by SO_2 as the cladding. The light is confined in the waveguide and coupled to the fundamental and the first modes when it propagates from the single mode section to the bimodal section. The biomodal interference can also be used in optical fiber. A multimode fiber biosensor has been reported by Cardona-Maya *et al.* by etching the cladding to a singlemode-multimode-singlemode fiber [151]. The LOD can be 0.2 mg/L for the detection of IgG.

The analytes and performance comparison of these interferometer biosensors mentioned above are summarized chronologically in Table 2.5.

2.5 Photonic Crystal Biosensors

A photonic crystal (PC) is a periodic optical nanostructure which has a varying RI. The propagation of electromagnetic waves are controlled by the structure of the photonic crystal which can be one, two or three dimensional. A basic two dimensional photonic structure is shown in Figure 2.14. It has been first reported by Yablonovitch [152]. The propagation of light is forbidden in a certain wavelength range known as the photonic band gap. By introducing defects, photonic crystals are utilized in many applications, such as waveguides, mirrors, and filters.

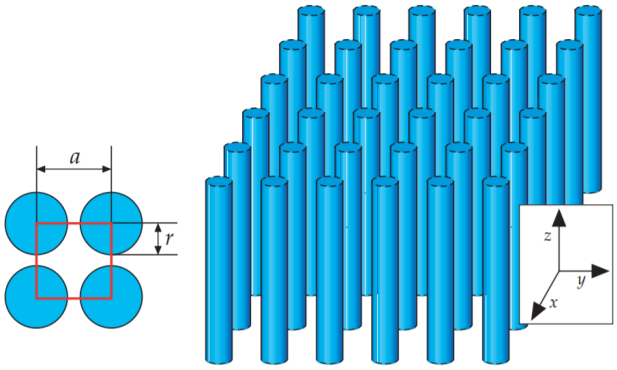

Figure 2.14: A basic two dimensional photonic crystal structure. The radius of the column is r. The material is homogeneous along the z direction and has varying RI along x and y with a lattice constant of a. The engineered structure of the photonic crystal allows only certain wavelengths of light to propagate. Reprinted from [13] with permission from Princeton University Press.

The basic principle of the photonic crystal is the symmetry principle. The periodic envelope function and periodic dielectric function can be satisfied as (2.4) and (2.5):

$$(\nabla + i\vec{k}) * \frac{1}{\varepsilon(r)}(\vec{\nabla} + i\vec{k}) \times \vec{H}_{(n,\vec{K})}) = (\frac{\omega_n \vec{k}}{c})^2 \vec{H}_{(n,\vec{K})} \tag{2.4}$$

$$\varepsilon(\vec{x}) = \varepsilon(\vec{x} + \vec{R}_i) \tag{2.5}$$

where k is the wave vector, $\vec{H}_{(n,\vec{K})}$ is the periodic envelop function with eigenvalue $\omega_n\vec{k}$ and $\vec{R}_i$ is the lattice vectors. The propagation modes allowed in the photonic cystral can be found by solving for the eigenvalues described above.

A one dimensional photonic crystal consists of multiple layers of alternating materials where the RI of the material is changed periodically in one dimension. A common example is the Bragg reflector where each layer causes partial reflection for a certain range of frequencies and acts as a band-pass filter. For a two dimensional photonic crystal, the RI of the structure is alternated periodically in two dimensions and the basic structures include hole-based photonic crystals and slab-based photonic crystals, which are created of air holes or silicon pillars in the lattice, respectively. Introducing line defect into photonic crystal structure can cause resonance with less loss compared with traditional waveguides [153]. With only the light within a narrow range of frequency being able to escape from the defect, a line defect photonic crystal waveguide produces a narrow peak in the spectrum with high quality factor, thus can be applied in optical biosensors [154]. Its high sensitivity and high quality factor make the photonic crystal biosensor one of the most powerful sensors to detect DNA [155], cells [156], and proteins [157] by measuring the small change of the RI [158]. Besides fabricating on SOI to obtain the photonic crystal biosensor, polymer [159], Si_3N_4 [160] and TiO_2 [161] have all been demonstrated as materials for the high index region. Due to the small sizes of the photonic crystal holes, E beam lithography[162] or focused ion beam lithography [163] are used to fabricate the structure of the photonic crystal.

The Ln cavity based photonic crystal removes n air holes to form the defect of the photonic crystal structure [164]. The microcavities confine the light to an ultra-low mode volume to produce the potential to enhance the sensitivity of the biosensor. Examples are L3-cavity [165], L7-cavity [166], L13-cavity, L21-cavity, and L55-cavity [167]. These photonic crystal microcavities have all been demonstrated as photonic crystal biosensors. Antibiotics and gentamicin being detected by the photonic crystal microcavities has been reported by Yan *et al*. [14]. The mode profiles of L13-cavity and L13-cavity with nanoholes PC waveguide are

shown in Figure 2.15. The L13-cavity and L13-cavity with nanoholes are formed by a row of 13 missing holes and by a row of 13 nanoholes in the Γ-K direction, respectively. Compared with the conventional L13-cavity structure, L13-cavity with nanoholes can increase the fill factor by 40% and obtain a larger resonance shift to measure gentamicin with the concentration as low as 1 nM.

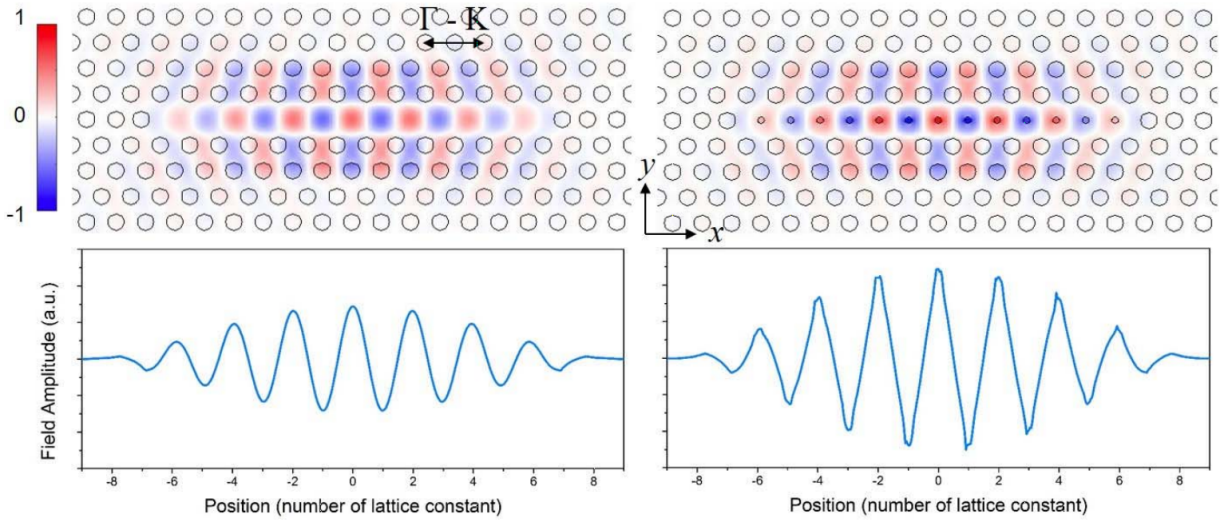

Figure 2.15: Mode profiles of L13 and L13 with nanoholes PC microcavities. Reprinted from [14] with permission from IEEE.

Slot waveguide photonic crystals have gained much attention recently. In the structure of slot photonic crystal, the light is not only confined by the photonic crystal, but is also spatially confined by the slot waveguide. The basic photonic crystal slot waveguide is formed by implementing an air slot into a photonic crystal waveguide [168]. The slot waveguide photonic crystal biosensor combines the respective advantages of a slot waveguide and a photonic crystal. By implementing the air slot in the photonic crystal waveguide and optimizing the parameters, the sensitivity can be 1538 nm/RIU and the quality factor can be 50000 [169]. An optical biosensor based on multi-slotted photonic crystal cavities has been presented by Xu *et al*. [170]. The device is patterned by electron-beam lithography. The pattern is transferred onto a silicon layer by anisotropic etching through an inductively coupled plasma process. The light propagating in this sensor interacts more with the lower RI region

to enhance the sensitivity to 586 nm/RIU. Another multi-slot photonic crystal biosensor based on a nano-slotted parallel quadrabeam integrated cavity achieves a sensitivity of 451 nm/RIU with a quality factor of larger than 7000 [171].

A photonic crystal nanobeam, which is a type of one dimensional photonic crystal, has also been studies for its high quality factor and small mode volume [172]. SOI wafer [173], polymer film [174] and porous silicon [175] have been used to fabricate photonic crystal nanobeam biosensors. Combining the functions of nanobeam and slot, a slotted photonic crystal sensor has been designed to test single nanoparticles [176]. The air slot is implemented as a row of air holes, at the end of which the structure gradually turns into a conventional photonic crystal sturcture without air slots. The sensitivity is 439 nm/RIU to test the particles with a maximum quality factor of 12000. Another slot nanobeam photonic crystal waveguide is based on embedded quantum dots of InAs [177]. By introducing an air slot bewtween two rows of nanobeam photoncic crystals, the sensitivity of the sensor reaches 900 nm/RIU. Furthermore, by tapering the width of the cavity region of a rectangular photonic crystal cavity, a nanobeam high-sensitivity photonic crystal optic biosensor shows a sensitivity of 428 nm/RIU with a quality factor of 1.3×10^4 [178].

A photonic crystal optical fiber biosensor consitst of a two dimensional photonic crystal in which a periodic array of micro air holes is embedded along the entire length of the fiber [179]. A photonic crystal fiber (PCF) sensor based on surface plasmon has been designed by Rifat *et al*. [180], which is performed by a stack-and-draw method [181]. The fabricated capillaries are stacked and then drawn into a cane, and finally pulled into a fiber. The PCF sensor consists of seven air-hole rings and a large air hole coated with gold that is introduced in the first ring. Resonance occurs when the real effective index of the core mode and SPP mode are the same, which lead to a sensitivity of 11000 nm/RIU. Another fiber biosensor based on a photonic crystal is designed by splicing one section PCF into two sections of multimode fibers, as shown in Figure 2.16. By coating gold and graphene oxide on the fiber

surface and immersing in staphylococcal protein A (SPA), the bulk sensitivity can achieve 4649.8 nm/RIU and the LOD can be 10 ng/mL for detection of human IgG [15].

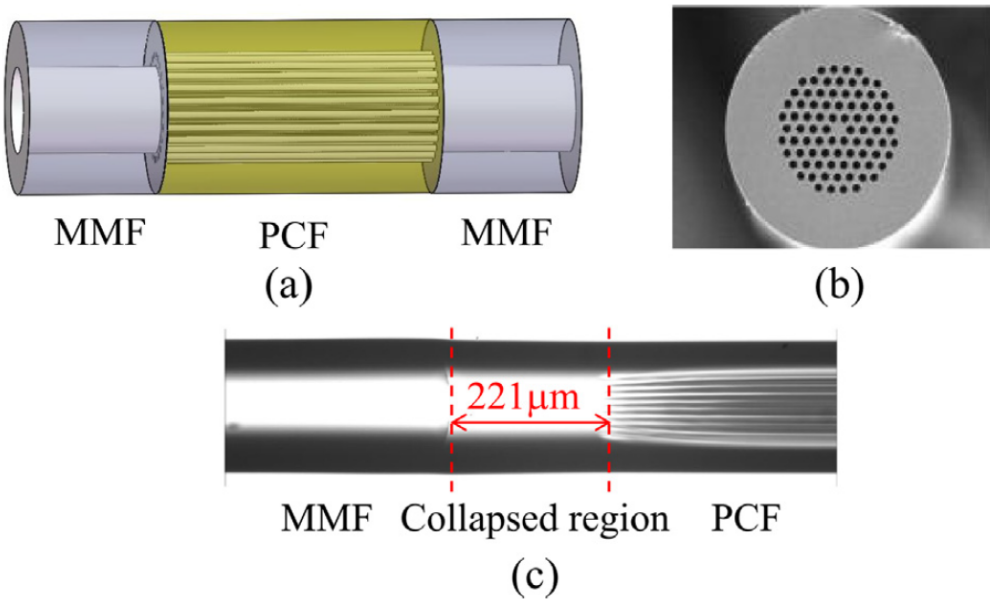

Figure 2.16: (a) A schematic of a MMF-PCF-MMF sensor. (b) A microscope photograph of the end face of PCF. (c) The collapsed region of PCF. Reprinted from [15] with permission from Elsevier.

A D-shaped photonic crystal fiber can also be designed for biosensor applications based on surface plasmon resonance by coating metal on the polished surface [182, 183]. A D-shaped photoinc crystal fiber based on suface plasmon coated by gold has been introduced by Wu *et al*. [184]. A wheel polishing setup is used to realize the side-polished PCF. By optimizing air holes arrayed in the cladding to the polished surface, the sensitivity of 21700 nm/RIU is obtained. Another D-shaped photonic crystal fiber sensor based on surface plasmon achieves the maximum sensitivity of 46000 nm/RIU at the RI of 1.42 [185] by coating TiO_2 on the fiber surface as the adhesion layer between gold and fiber and broadening the operating wavelength range. Unlike the conventional photonic crystal fiber biosensor, a hollow Bragg optical fiber has been introduced by Li *et al*. based on its hollow core surrounded by alternating layers with varying RI [16], as shown in Figure 2.17. The sensor is fabricated by heating and drawing the preform in a drawing tower. The device's sensitivity is 1850 nm/RIU.

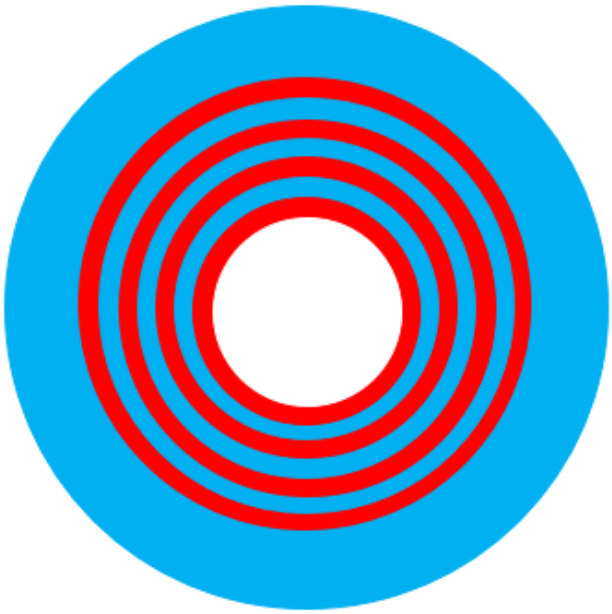

Figure 2.17: A cross section view of a hollow Bragg fiber of which the large hole is surrounded by a periodic sequence of high (blue) and low RI (red) layers. The alternating layers help enhance the performance of the sensor through better light confinement and improve its sensitivity. Reproduced from [16] with permission from OSA.

The analytes and performance comparison of these photonic crystal biosensors mentioned above are summarized chronologically in Table 2.6.

2.6 Ring Resonators

The earliest integrated ring resonator has been published in 1969 by Marcatili *et al.* [186]. A basic ring resonator consists of a line waveguide and a ring waveguide where the light propagating in the line waveguide will be coupled to the ring waveguide. The light is confined in the waveguides by total internal reflection and the resonance occurs when the optical path difference is a multiple of the wavelength of the light due to the constructive interference.

Ring resonator sensors find a number of applications in chemical and biological sensing and detection [187, 188], and have shown potential in industry [189]. When the analyte is bonded to the ring resonator, the change of the RI of the analyte leads to the change of the

Table 2.6: Analytes and performance comparison of photonic crystal biosensors.

Year	Sample	Sensitivity	LOD	Q factor	Concentration	Ref.
2003	RI liquid	11000 nm/RIU	NA	NA	NA	[179]
2007	RI liquid and BSA	NA	~10 μg/mL	NA	NA	[158]
2007	BSA	Min detection mass: 2.5 fg	NA	NA	NA	[154]
2009	RI liquid	1538 nm/RIU	NA	50000	NA	[169]
2010	RI liquid	900 nm/RIU	NA	700	NA	[177]
2010	RI liquid and monolayer of 3-APTES molecules	100 nm/RIU	NA	NA	NA	[165]
2010	Single-strand DNA	NA	19.8 nM	NA	NA	[155]
2011	Glucose	386 nm/RIU	NA	36000	NA	[174]
2012	RI liquid	460 nm/RIU	NA	NA	NA	[166]
2013	RI liquid	3692 nm/RIU	NA	NA	NA	[157]
	and IgG	NA	0.267 mg/L	NA	NA	
2013	HPV virus-like nanoparticles	NA	1.5nm	NA	NA	[162]
2013	ZEB1 in lysates	2 cells per mL	NA	NA	NA	[156]
2013	Biotin-avidin binding	NA	NA	NA	67 pg/mL for L21 3.35 pg/mL for L55	[167]
2015	RI liquid	451 nm/RIU	NA	$>$ 7000	NA	[171]
2015	RI liquid	428 nm/RIU	NA	13000	NA	[178]
2015	Single-nanoparticle	439 nm/RIU	NA	~12000	NA	[176]
2017	RI liquid	7381 nm/RIU	NA	NA	NA	[182]
2017	RI liquid	21700 nm/RIU	NA	NA	NA	[184]
2017	RI liquid	46000 nm/RIU	NA	NA	NA	[185]
2017	Gentamicin	NA	NA	NA	0.1 nM - 1 μM	[14]
2018	RI liquid	4649.8 nm/RIU	NA	NA	NA	[15]
	and IgG	NA	10 ng/mL	NA	NA	
2019	RI liquid	1850 nm/RIU	NA	NA	NA	[16]
2019	APTES	1023 nm/RIU	NA	NA	NA	[175]
	and PNA	1.6 pm/nM	NA	$<$ 8900	NA	

effective RI of the ring. This results in a peak shift in the spectrum due to the change of the optical path. It can be described by (2.6),

$$2\pi R n_{eff} = m\lambda, \qquad m = 1, 2, 3, ... \tag{2.6}$$

where n_{eff} is the effective RI of the propagating mode and R is the radius of the ring.

Various materials are used to fabricate the waveguides and ring resonators. A ring resonator immunsensor based on SOI has been developed by Valera *et al.* to detect MCP-1

in buffer and human serum samples [190]. An LOD of 0.5 pg/mL has been shown. By optimizing the thickness of the silicon waveguide to 150 nm, the ring resonator biosensor fabricated on SOI wave can achieve a bulk sensitivity of 270 nm/RIU for a guided TM mode wave. It can also verify the detection of biological interactions, such as standard sandwich assays [191]. Besides SOI, silicon oxynitride (SiON) [192], porous silicon [193] and polymers [194] have been reported as the structure materials for ring resonator biosensors. By connecting three sensor micro-rings with a reference micro-ring, a ring resonator biosensor has been designed to detect human immunoglobulin E (IgE) and human thrombin with LODs of 33 pM and 1.4 nM, respectively [195]. Compared with conventional ring resonators, a suspended ring resonator structure has been demonstrated to achieve a symmetrical optical mode distribution and nearly 3.6 times improvement in the mode overlap with the target analytes [196]. The ring and waveguide is fabricated using standard CMOS technology, including UV lithography and RIE etching. A buffered oxide etch is used to release the suspended structure. A concentration as low as 100 nM Herceptin has been detected. From the fabrication perspective, the reported structure was patterned by e-beam lithography with the help of Monte Carlo simulation. It was then dry etched by RIE with an additional wet etching step to obtain the suspended microring resonators.

Two or more rings with different individual free spectral ranges can be cascaded to enhance the total free spectral range through the Vernier effect [197]. This technique can be applied to enhance the sensitivity of biosensors [198, 199]. A ring resonator biosensor based on the Vernier effect and suspended silicon nanowires introduced by Hu and Dai achieves a sensitivity of 4.6×10^5 nm/RIU with an LOD of 4.8×10^{-6} RIU [200]. A cascaded double-ring resonator sensor based on the Vernier effect has been introduced by Jiang *et al.* [17], as shown in the Figure 2.18. Unlike simply two cascaded rings, both ring resonators consist of one sensor ring and one reference ring. The transmission spectrum of each sensor is the product of the two rings' transmission spectra. The sensitivity of such double-ring resonator is 24300 nm/RIU. A three cascaded ring resonator based on Vernier effect sensor achieves a

lower sensitivity of 5866 nm/RIU but a range of measurement increased to 7.6×10^{-2} which is about 24.7 times compared with the conventional two cascaded ring sensor [201].

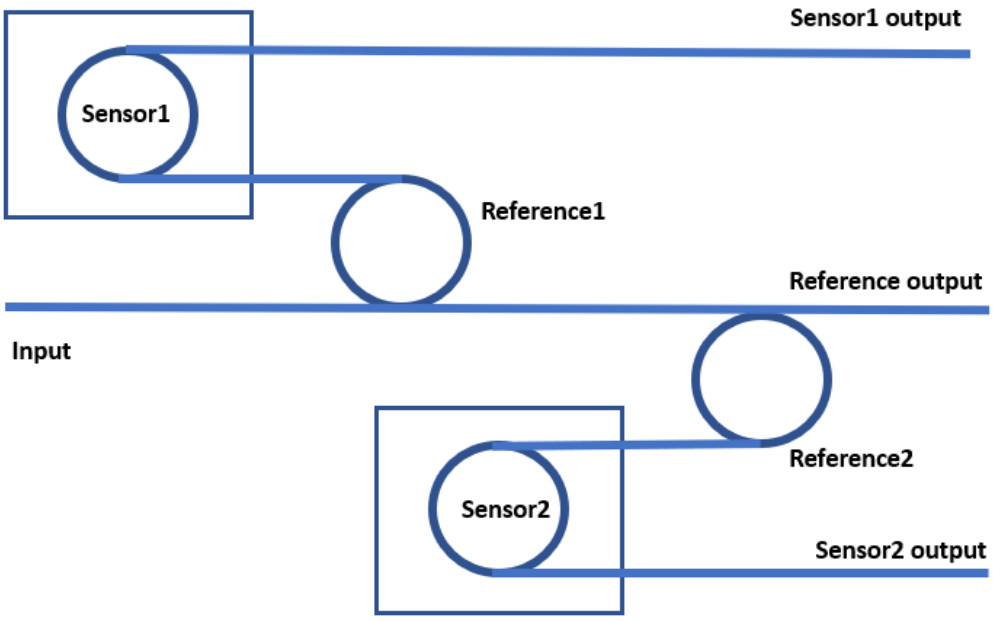

Figure 2.18: A schematic diagram of two cascaded double-ring resonator biosensors based on the Vernier effect. The output spectrum of each sensor is the product of the two rings' transmission spectra. Reproduced from [17] with permission from OSA.

In addition to SOI based cascaded rings, a cascaded ring resonator based on the polymer Ormocore has been shown to produce a FSR of 4.6 nm and an increase in sensitivity by 16-fold [202]. A biosensor based on cascaded ring resonators that uses intensity interrogation has shown a high sensitivity of 1579 dB/RIU with the detection of limit of 9.7×10^{-6} RIU. The sensing ring is modified with molecularly imprinted polymers for the detection of progesterone with an LOD of 83.5 fg/mL [203].

Along with wavelength interrogation and intensity interrogation, a ring resonator based on phase interrogation to detect the cladding material has been introduced by Liu *et al*. [204]. Two lasers are launched into the ring with one laser aligned to the ring resonance and the other slightly off resonance. The sensitivity is 6×10^{-3} rad/RIU and the LOD is 2.5×10^{-6} RIU.

Using a slot waveguide along with ring resonator biosensors enables the light to interact more with the analyte to enhance the sensitivity [205]. A ring resonator based on slot waveguide has demonstrated a sensitivity of approximately 1×10^{-8} g/mL for the detection of prostate specific antigen (PSA) [206]. Another ring resonator biosensor based on double-slot hybrid plasmonic waveguides has been introduced by Sun *et al.* [207]. The narrow slots enhance the confinement for the optical energy leading to the sensitivity of 687.5 nm/RIU with the LOD of 5.37×10^{-6} RIU.

A whispering-gallery mode (WGM) is a resonance mode of a wave in a resonator formed by a cavity with smooth edges. The resonant wavelength of WGM is determined by (2.6), where R is radius of the optical structure. WGM based devices have been successfully used as optical biosensors [208, 209, 210]. A biosensor based on WGM created from silca microspheres has been designed by Anderson *et al.* [211]. It is applied to detect H.hepaticus with the LOD of 1×10^{3} cells/mL. The microsphere is obtained by using a 25-W CO_2 laser to melt the tip of a single mode fiber. Thin-walled capillary based sensors also benefit from WGM [212]. An optical biosensor based on WGM can excite mechanical vibrations by its thin-walled capillary. The sensitivity of 1.2 Hz/(pg/mm^2) can be achieved with the LOD of 83 pg/mm^2 [213]. Another ring resonator optical biosensor based on WGM has been introduced by Zhang *et al.* [18]. As shown in Figure 2.19, it consists of one ring laser as a master resonator and one optofluidic ring tube as a slave resonator. Both resonators are made of PDMS by pulling the fiber out from the PDMS. The sensitivity can achieve 5930 nm/RIU due to the Vernier effect and the large ratio change of effective RI. Using a capillary to replace the PDMS to form two thin-wall silica capillaries, another sensor has demonstrated a sensitivity of 2510 nm/RIU with an LOD of 1.6×10^{-5} [214]. Instead of employing a solid dye laser, a flowed dye solution can improve the stability and reduce the noise, which achieves the sensitivity of 3874 nm/RIU with the LOD of 2.6×10^{-6} RIU [215]. Another ring (disk) resonator based on WGM has been introduced by Khozeymeh and Razaghi [216]. The quality factor can be larger than 25000 and the sensitivities for the

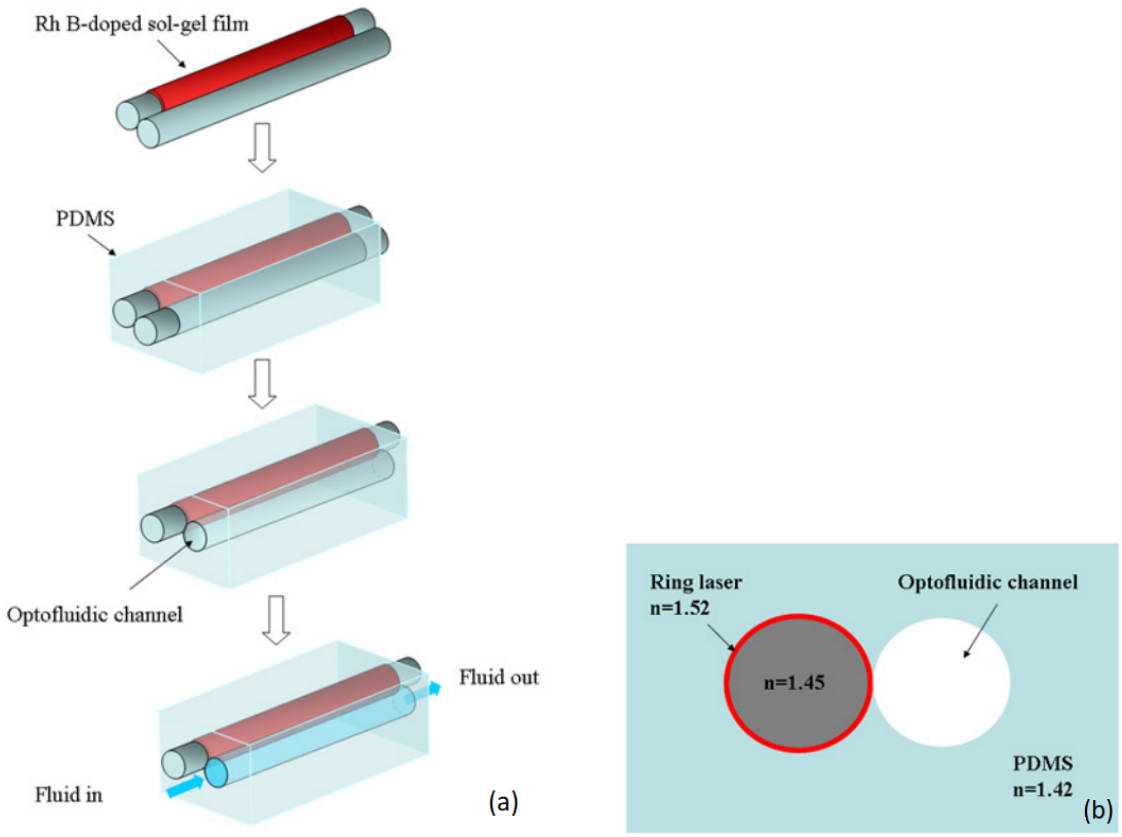

Figure 2.19: A ring resonator optical biosensor based on Whispering-Gallery mode (a) Fabrication process of an optofluidic coupled cavity. (b) The cross-section of the coupled cavity. [18]

singe disk and dual disk are 193 nm/RIU and 134 nm/RIU, respectively. To suppress the common-mode noise, a self-referencing optofluidic sensor based on a ring resonator has been introduced by Li *et al.* to detect bovine serum albumin and achieved an LOD of 2 pg/mL with low noise [217]. Besides WGM liquid channel sensors, a liquid-core waveguide based ring resonator has been presented by Testa *et al.* [218]. The alternating SiO_2 and Si_3N_4 layers are fabricated as the antiresonant cladding layers by LPCVD. The interaction for the light and test analytes is enhanced and the RI sensitivity reaches 700 nm/RIU.

The analytes and performance comparison of these ring resonator based biosensors mentioned above are summarized chronologically in Table 2.7.

Table 2.7: Analytes and performance comparison of ring resonator biosensors.

Year	Sample	Sensitivity	LOD	Q factor	Concentration	Ref.
2009	RI liquid	298 nm/RIU	4.2×10^{-5} RIU	NA	NA	[205]
	and avidin	λ shift: 2.2 nm	NA	NA	NA	
2010	RI liqiud	570 nm/RIU	NA	1.2×10^{5}	NA	[187]
	and Biotin					
2011	RI liquid	1070 nm/RIU	1.6×10^{-5} RIU	NA	NA	[198]
2011	RI liquid	4.6 $\times10^{5}$	4.8×10^{-6}	NA	NA	[200]
2011	RI liquid	λ shift: 25 fm	NA	NA	NA	[208]
2011	RI liquid	5390 nm/RIU	NA	NA	NA	[18]
2012	Glucose	2510 nm/RIU	1.6×10^{-5} RIU	NA	NA	[214]
2013	RI liquid	24300 nm/RIU	NA	NA	NA	[17]
2013	IgE	NA	33 pM	NA	NA	[195]
	and thrombin	NA	1.4nm	NA	NA	
2013	BSA	2 pg/mL	NA	NA	NA	[217]
2014	RI liquid	6×10^{3}/RIU	2.5×10^{-6} RIU	NA	NA	[204]
2014	Glucose	1.84 pm/mM	NA	NA	NA	[212]
2014	Hydrofluoric	NA	83 pg/mm^2	NA	NA	[213]
	acid solutions					
2015	RI liquid	428 nm/RIU	NA	13000	NA	[178]
2015	RI liquid	687.5 nm/RIU	~5.37×10^{-6} RIU	NA	NA	[207]
2015	RI liquid	112 nm/RIU	1.6×10^{-6}	NA	NA	[192]
	and AFM1	NA	NA	NA	12.5 nM	
2015	RI liquid	380 nm/RIU	NA	~10000	NA	[193]
	and nucleic acid					
2015	RI liquid and IgG	1804 nm/RIU	7.1 μg/mL	NA	NA	[199]
2015	H.hepaticus	NA	1×10^{3} cells/mL	NA	NA	[211]
2016	RI liquid	~700 nm/RIU	~1.57×10^{-6} RIU	NA	NA	[218]
2016	MCP-1	NA	0.5 pg/mL	NA	84.3-1582.1 pg/mL	[190]
2016	PSA	~1×10^{-8} g/mL	NA	NA	NA	[206]
2017	RI liquid	5866 nm/RIU	NA	NA	NA	[201]
2017	RI liquid	270 nm/RIU	NA	10100	NA	[191]
	and biological	λ shift: $>$ 400 pm	NA	NA	NA	
	sandwich assays					
2017	RI liquid	1579 dB/RIU	9.7×10^{-6} RIU	NA	NA	[203]
	and progesterone	NA	83.5 fg/mL	NA	NA	
2017	Glucose	3874 nm/RIU	2.6×10^{-6} RIU	NA	NA	[215]
2018	RI liquid	310 nm/RIU	NA	~30000	NA	[196]
	and Herceptin	NA	NA	NA	100 nM	
2019	RI liquid	increase by by 16-fold	NA	NA	NA	[202]
2019	RI liquid	193 nm/RIU	NA	NA	NA	[216]
2019	RI liquid	300 nm/RIU	NA	NA	NA	[189]
	and BSA	λ shift: 0.5 nm	NA	NA	NA	
2019	RI liquid	NA	NA	8×10^{5}	NA	[194]
	and BSA					

2.7 Biosensors Combining Multiple Methods

Biosensors combining the advantages of the various methods previously described are often able to improve the sensitivity. In this section, several recently developed integrated optical biosensors are summarized.

A biosensor based on a one-dimensional photonic crystal combined with a ring resonator to enhance the light confinement and the light-matter interaction has been demonstrated [219]. An optical biosensor based on a photonic crystal ring resonator can operate in both air and dielectric bands, and produce a resonance in the air band mode to obtain a sensitivity of 87 nm/RIU with a quality factor greater than 10000 [220]. Another optical biosenosr based on a photonic crystal ring resonator has been presented by Lo *et al.* [221]. Due to the localized optical mode field of the photonic crystal structure, the bulk sensitivity can achieve 248 nm/RIU. The detection of DNA, biotin and streptavidin has also been verified with this sensor.

The optical fiber biosensor combining fiber Bragg gratings, localized surface plasmon and long range surface plasmon has been reported by Lao *et al.* [222]. The light is coupled to the cladding by the gratings and the gold film coated on the fiber enhances the resonance. Gold nanoparticles are functionalized to bind the analyte. The overall effect leads the LOD of thrombin of 1 nM.

An MZI biosenosor based on one-dimensional photonic crystal in the sensing arm has been introduced by Qin *et al.* [223]. The light is squeezed to produce a slow light effect and enhance the relative phase shift to achieve a bulk sensitivity of 84000 rad/RIU-cm. The sensor has a compact footprint, and has demonstrated the detection of nucleic acid molecules. Another MZI biosensor based on sub-wavelength gratings in sensing arm has been introduced by Sumi *et al.* [224]. The phase difference between the sensing and reference arms for the given wavelength has a relatively flat maximum. The sensor achieves a sensitivity of 931 rad/RIU/mm. An MZI based on long range surface plamon has been designed by Khan *et al.* [225]. The sensor made from gold stripes in Cytop with an etched microfluidic channel has reached an LOD of approximately 9×10^{-7} RIU.

A ring resonator has also been combined with MZI as a biosensor [226]. A ring resonator optical biosensor based on MZI and Vernier effect has been introduced by Azue *et al.* [19]. SU8 2000 polymer is used as core of the waveguide while PMATRIFE polymer is used

as cladding layer and superstratum for the reference ring. As shown in Figure 2.20, by implementing a ring resonator to each arm of the MZI to produce Vernier effect, the sensor can achieve the sensitivity of 17558 nm/RIU for glucose detection.

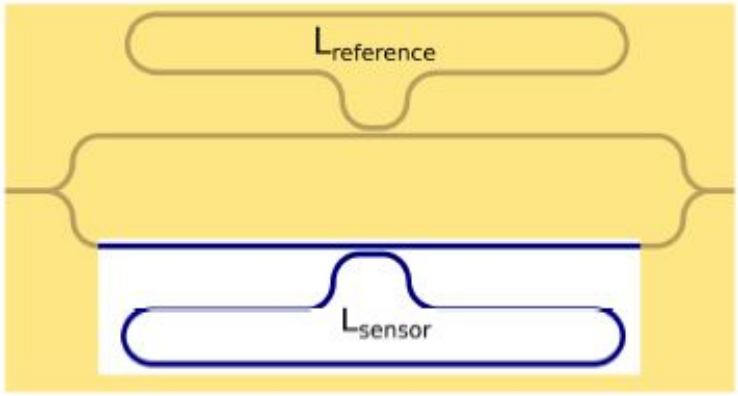

Figure 2.20: A schematic diagram of a ring resonator optical biosensor based on MZI and Vernier effect. The sensor ring is in the reservoir (white rectangle) etched in the PMATRIFE superstrate (yellow) covering the the sensor. The reservoir is covered by the analyte to be detected. Reprinted from [19] with permission from OSA.

The combination of a ring resonator and SWG to design an optical biosensor can decrease the light confinement in the core of the waveguide and tailor the effective RI to enhance the sensitivity [227, 228, 229, 230]. Subwavelength multibox waveguides that consist of five rows of silicon squares have been studied in a ring resonator optical biosensor to enhance the bulk sensitivity to 579.5 nm/RIU and the surface sensitivity to 1900 pm/nM for biological sandwich assay detection [231]. A suspended waveguide which can balance the sensitivity and the propagation loss has been used in the ring SWG optical biosensor to reach the quality factor of 15300 with the sensitivity of 337.5 nm/RIU [232]. Compared with the suspended structure, a pedestal structure can also be used with a SWG ring resonator biosensor to reduce the distribution of asymmetric RI and introduce a more robust structure. A biosensor based on a pedestal structure has been reported by Chang *et al.* [20], as shown in Figure 2.21. The pedestals are under the gratings and formed by undercut etching to increase mode volume overlap factor. A greater resonance shift for Sulfo-NHS-Biotin immobilization has

been shown and the detection of streptavidin has been demonstrated at a low concentration of 0.1 ng/mL with 0.15 nm as resolution.

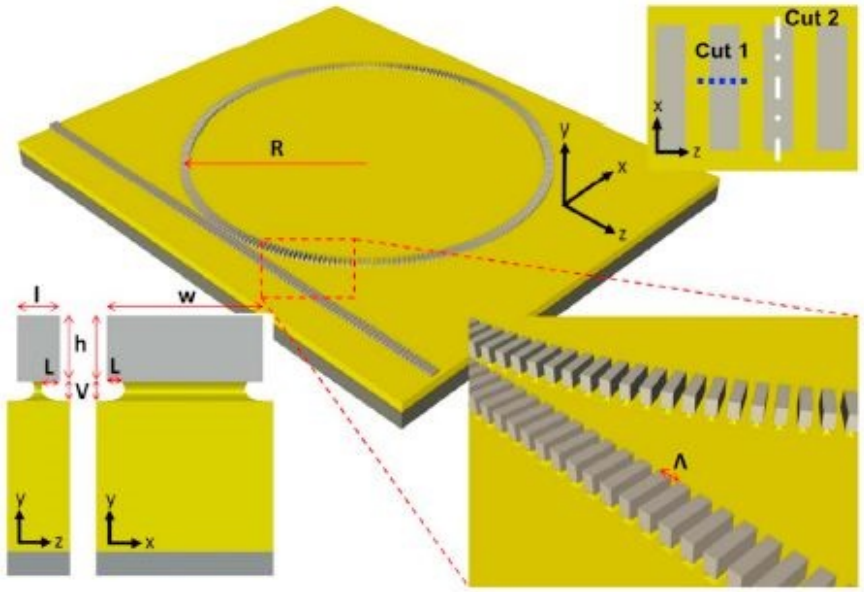

Figure 2.21: A schematic diagram of a pedestal subwavelength grating metamaterial waveguide ring resonator, where R is the diameter of the ring, Λ is the grating period, h is the thickness of ring waveguide, w is the width of waveguide core, l is the length of pillar, L is the depth of lateral etching propagation, and V is the depth of the vertical etching propagation. Reprinted from [20] with permssion from Elsevier.

An optical biosensor based on a PCF and a MZI can produce higher mechanical stability and easier fabrication and measurement [233]. The cladding mode is excited when the light is coupled into the PCF and interferes with the core mode. By splicing a short section of PCF between two standard single mode fibers, a PCF biosensor has reached the sensitivity of 326 nm/RIU [234]. Two collapsing points are made in a PCF at certain regions by a fusion splicer to form the sensor. Other techniques involving a PCF include fiber tapering at the splicing point [235], up-tapered joint [236], nonadiabatically tapering a small section of the fiber [237], and introducing a PCF taper between two waist-broadened tapers of SMF-PCF [238]. Besides the method of splicing, a PCF biosensor has also been demonstrated by coating hafnium oxide on the surface of the PCF to enhance the sensitivity to the surrounding medium by Melo *et al*. [239]. The sensor demonstrates a sensitivity of 1307 nm/SRI. Another

optical biosensor based on a PCF and a MZI has been introduced by Du *et al*. [240]. By etching the surface of the PCF, the sensitivity can achieve 359.37 nm/RIU. A biosensor based on a PCF and a MZI uses a cavity ring down loop to improve the performance of the sensor [241]. The sensor acheives an LOD of 7.8×10^{-5} RIU. Another PCF and MZI biosensor uses alcohol to fill the air holes of the PCF to decrease the difference of RI between the core and the cladding [21], as shown in Figure 2.22.

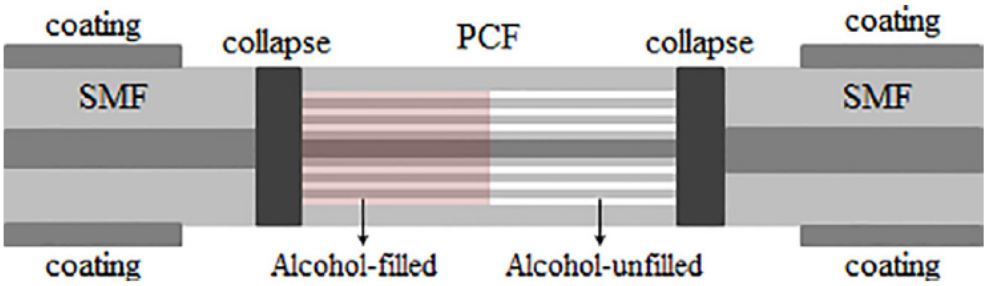

Figure 2.22: Alcohol-filled PCF sensing probe based on MZ interferometry. The alcohol helps decrease the difference in RI between the core and cladding. Reprinted from [21] with permission from Elsevier.

Optical biosensors can also be improved by integrating a FPI with a PCF [242]. As shown in Figure 2.23, Tian *et al*. [22] have demonstrated a sensor based on FPI and PCF by splicing a segment of a concave-core PCF with a segment of SMF. The concave-core forms a physically short cavity which allows liquid to flow into the sensor with ease and significantly reduces the measurement time. Another PCF optical biosensor based on FPI has been introduced by splicing a hollow core PCF into two sections of SMF and cleaving the pigtail of SMF to a proper length [243]. The two interfaces of concave-core of the fiber function as mirrors to form the FPI cavity, obtaining a sensitivity of 1635.62 nm/RIU and a fast response time. A sensitivity of -136 dB/RIU has been shown for the detection of yeast growth. This structure can also be used to detect the specific rabbit IgG as well. For antigen binding, the wavelength increases by 190 pm and the contrast of fringe decreases by 2.15 dB [244]. Another PCF optical biosensor based on FPI has been shown by connecting the multimode photonic crystal fiber (MPCF) with SMF. The sensor achieves a sensitivity of

21.52 dB/RIU and a resolution of 1.7×10^{-5} [245]. Furthermore, a novel sensor has shown a sensitivity of 178.7 nm/RIU by cascading SMF-HCF-PCF-SMF to obtain a transmitted MZI and a reflected FPI [246].

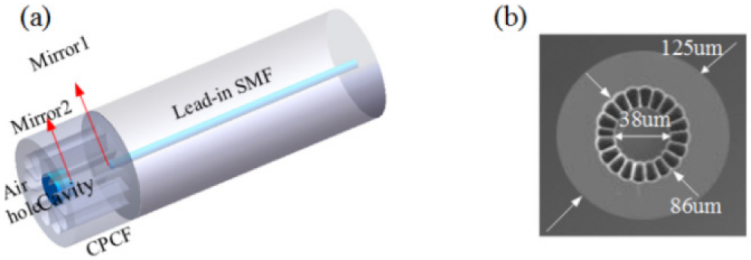

Figure 2.23: (a) A schematic diagram of an optical biosensor based on a concave-core PCF and FPI. (b) A microscope photograph of the cross section of the sensor. The concave-core forms a physically short cavity which allows liquid to flow into the sensor with ease and significantly reduces the measurement time. Reprinted from [22] with permission from OSA.

The analytes and performance comparison of the multi-configuration biosensors mentioned above are summarized chronologically in Table 2.8.

2.8 Conclusion

This chapter reviews several categories of optical waveguide biosensors based on RI scheme developed recently, including evanescent waveguide biosensors, surface plasmon resonance waveguide biosensors, grating coupler biosensors, interferometers, photonic crystal biosensors, ring resonators, and biosensors combinging multiple methods. The quality factors, sensitivities, and detection limits of the sensors are summarized and compared to study the performances. All these kinds of waveguide based biosensor can be well applied in biological molecules. Analyses of the biosensors suggest to improve performance to not only diversify the sensor materials, technologies and tools, but also to combine different methods in one design so as to integrate advantages from them, resulting in improved sensitivities or quality factors.

For ease of use and greater applicability, optical waveguide biosensors should be designed to interface to the outside world more easily with simplified experimental apparatus.

Table 2.8: Analytes and performance comparison of biosensors by combining different methods.

Year	Sample	Sensitivity	LOD	Q factor	Concentration	Ref.
2012	RI liquid	11.7 $\mu s^{-1}RIU^{-1}$	7.8×10^{-5} RIU	NA	NA	[241]
2012	Sucrose	326 nm/RIU	NA	NA	NA	[234]
2013	RI liquid	NA	9×10^{-7} RIU	NA	NA	[225]
2014	RI liquid	401 nm/RIU	NA	NA	NA	[227]
2014	RI liquid	21500/RIU	NA	NA	NA	[226]
	and IgG	1 ng/mL	NA	NA	NA	
		λ shift: 0.5 nm				
2015	RI liquid	252 nm/RIU	NA	NA	NA	[236]
2015	RI liquid	-21.52 dB/RIU	1.7×10^{-5} RIU	NA	NA	[245]
2016	RI liquid	260.8 nm/RIU	NA	NA	NA	[235]
2016	RI liquid	281.6 nm/RIU	NA	NA	NA	[238]
2016	RI liquid	178.7 nm/RIU	NA	NA	NA	[246]
2016	RI liquid, biological	440.5 nm/RIU	NA	NA	NA	[228]
	sandwich assay,	~1nm/1nm	NA	NA	NA	
	and microRNA	λ shift: 0.19 nm	NA	NA	NA	
2016	RI liqiud and Biotin	89/RIU	NA	$>$ 10000	NA	[220]
2016	RI liquid,	84000 rad/RIU-cm	NA	NA	NA	[223]
	DNA and PNA	λ shift: 0.46 nm	NA	NA	NA	
2016	RI liquid and thrombin	490 nm/RIU	2×10^{-6}	7000	NA	[229]
2016	RI liquid	36 dB/RIU	NA	NA	NA	[243]
	and yeast growth	λ shift: 0.04 nm	NA	NA	NA	
2016	Glycerin solution	1307 nm/RIU	NA	NA	NA	[239]
2016	IgG	λ shift: 190 pm	NA	NA	NA	[244]
2017	RI liquid	~931 rad/RIU/mm	NA	NA	NA	[224]
2017	RI liquid	429.7$\pm$0.4 nm/RIU	3.71×10^{-4} RIU	NA	NA	[230]
2017	RI liquid	224.2 nm/RIU	NA	NA	NA	[233]
2017	RI liquid, DNA,	~248 nm/RIU	NA	NA	NA	[221]
	Streptavidin,	λ shift: 2.42 nm	NA	NA	NA	
	and Biotin					
2017	RI liquid	722.3 nm/RIU	NA	NA	NA	[237]
	and BSA	NA	125 pg/mL	NA	NA	
2017	Glucose	17558 nm/RIU	1.1×10^{-6} RIU	NA	NA	[19]
2017	RI liquid	337.5 nm/RIU	NA	15300	NA	[232]
2018	Thrombin	NA	1 nm	NA	NA	[222]
2019	RI liquid	359.37 nm/RIU	NA	NA	NA	[240]
2019	RI liquid	386.66 nm/RIU	NA	NA	NA	[21]
2019	RI liquid and biological	579.5 nm/RIU	NA	NA	NA	[231]
	sandwich assay	1900 pm/nM	NA	NA	NA	
2019	RI liquid, NSH-Biotin	545 nm/RIU	NA	NA	NA	[20]
	imobilization,	λ shift: 0.71 nm	NA	NA	NA	
	and Streptavidin	NA	NA	NA	0.1 ng/mL	

From the fabrication perspective, due to the small wavelength of the light, it is common for a biosensor to include nanometer-sized structures to interact with the light and measured

analyte. For examples, fabrication in the vertical direction typically requires growth technologies such as molecular beam epitaxy, metal organic chemical vapor deposition, atomic layer deposition or e-beam evaporation for film deposition, while the horizontal direction needs the techniques of nanolithography and nanoetching. Increasing the light interaction area or combining different methods in one design to increase field overlap with the analyte will lead to a better performance, but at a cost of a more complicated structure. For applicability in the commercial market, the optical waveguide biosensors need to be easily fabricated and low-cost. Though the structures may be more complicated, continuous technological innovations in fabrication and packaging of optical waveguide biosensors will boost the growth of commercial applications in the upcoming years.

To reduce the cost and be competitive in the market, the optical waveguide biosensor should be designed for low cost production with greater compatibility and ease of use. For a commercial product, the tunable lasers can be replaced by LEDs. Cameras or photodiodes can be chosen as the detectors instead of traditional spectrum analyzers. By choosing the appropriate source and detection scheme, the size, weight and power of the biosensors can be greatly reduced and portability achieved. Embedding the biosensors into the consumer electronic products, such as smartphones, will bring convenience to users as well. Furthermore, better integration of the optical structure and the fluidics system can provide more analytical functions to the user. If the biosensor can be fabricated on SOI wafers and integrated with CMOS circuits, even lower costs, lower power consumption and smaller sizes will be achieved. With the development of artificial intelligence and the market demand of the internet of things, new trends in optical biosensors include the integration with smartphones and wearable devices. From the expectation of researchers, the market for optical waveguide biosensors continues its rapid growth rate through 2020. By meeting the challenges in cost and manufacturing, optical waveguide biosensors will have great potential in the future.

Chapter 3

Modeling of a diffraction grating coupled waveguide based biosensor

3.1 Introduction

Grating couplers are a common optical component for introducing light into on-chip photonic structures. They are used extensively for optical interconnects and optical device integration. Grating couplers were presented initially by Dakss [72], and have been used for many other applications including biosensing [247] [248].

In this chapter, a MDGCW based biosensor is presented. The MDGCW based biosensor has the following advantages: easy experimental integration, cost effective fabrication, and relatively high sensitivity. Most diffraction grating based biosensors use the binding reaction of the analyte on the patterned surface of the grating coupler, which changes the effective refractive index of the coupler. Either the coupling angle of the incident light is varied to find the peak intensity of the reflected light [78], or a static angle is chosen and the reflected intensity is measured [73]. Unlike sensors where the binding occurs on the grating, in our MDGCW based biosensor the binding occurs on the dielectric slab of the optical elements similar to research presented in [79]. The dielectric slab forms a capping layer for a microfluidic channel through which the analyte of interest is introduced to the device. The grating itself and the sensitivity of the biosensor depends on the peak shift in the light spectrum. This technique allows for simple fabrication and an unobstructed light path to the grating. Moreover, the binding layer under the grating will not influence the patterned structure of the grating coupler and can simplify analysis. COMSOL Multiphysics® is used to model the MDGCW based biosensor and the results are shown in this chapter.

3.2 Theory

A classical optical grating structure is made of periodic slits in an opaque medium. Each slit is regarded as an independent source of light which interferes with one another to generate the classical diffraction pattern known from geometric optics, as shown in Figure 3.1. A binary grating, as shown in Figure 3.2, is used as a basic coupling structure. It consists of an array of narrow periodic thin rectangular ridges of alternating RI. Mathematically this effect can be described by Eq. (3.1) for reflection and transmission as:

$$d(n_t \sin \psi_t - n_i \sin \psi_i) = m\lambda \tag{3.1}$$

where d is the grating period, n_t is the refractive index of the transmitted medium and n_i is the refractive index of the incidence medium. λ is the wavelength of the light, ψ_i is the coupling angle, and ψ_t is the angle that the light propagates in the grating coupler. Grating couplers are common optical components for introducing light into on-chip photonic structures and they were presented initially by Dakss *et al.* [72]. They are used extensively for optical interconnections especially optical devices integration.

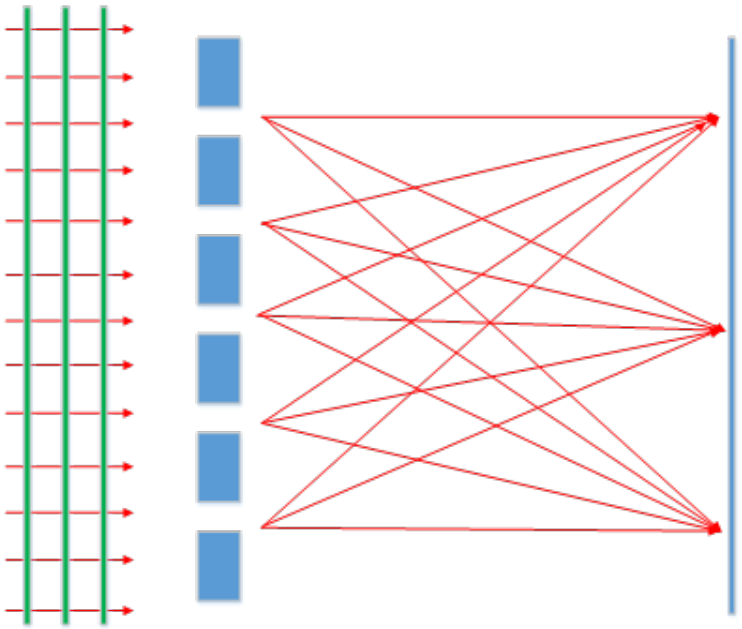

Figure 3.1: Principle of a classical optical grating.

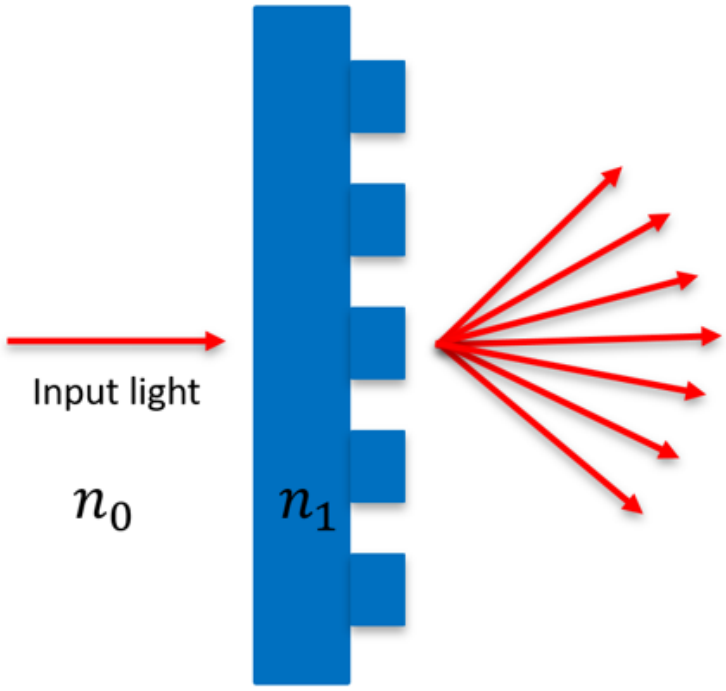

Figure 3.2: Light incident onto a binary grating will be diffracted to several diffraction orders.

Furthermore, The following equations can be used to extend Eq. (3.1) to accurately predict the coupling parameters, and can be written as Eq. (3.2), Eq. (3.3) and Eq. (3.4):

$$n_{eff} = n_t \sin \psi_t \tag{3.2}$$

$$n_{eff} = n_i \sin \psi_i + \frac{m\lambda}{d} \tag{3.3}$$

$$\triangle n_{eff} = n_i \sin \psi_i + \frac{m\triangle\lambda}{d} \tag{3.4}$$

where n_{eff} is is the effective refractive index of the light coupled into the grating coupler, $\triangle n_{eff}$ is the change of the effective refractive index and $\triangle\lambda$ is the change of the wavelength of the light. The change of the wavelength will lead to the change of the effective refractive index, and cause the change of the coupling efficiency.

The geometry of the MDGCW based biosensor is shown in Figure 3.3. The sensor consists of two grating couplers, a waveguide between the two grating couplers, a PDMS flow cell, and an aqueous medium containing a reagent of interest. The n_{eff} will change

as a result of analyte binding to the substrate. From Eq. (3.4), when n_i and $\sin\psi_i$ are constant, $\triangle n_{eff}$ will influence the light coupled into the waveguide and cause a shift of the peak in the output spectrum. When the light coupled into the waveguide, the peak of the resonance will be shifted linearly due to the change of n_{eff}, and changing n_{eff} also influences the propagation mode of the light in the waveguide. Furthermore, n_{eff} can be calculated by effective index techniques or numerical methods [249]. For both solutions, n_{eff} is related to the normalized frequency, propagation parameter, and asymmetry parameters of the structure. These parameters depend on the wavelength of the light, the dimensions of the structure, and the refractive index of the media. So the refractive index of the binding layer and the dimension of the binding layer will affect n_{eff} and thus the light coupled into the waveguide. When the RI of the binding layer is changed to different values, the peak shift in the spectrum will be linearly proportional to the change of the refractive index. The peak shift is related to the sensitivity of the biosensor. So the sensitivity can be obtained by the following:

$$s = \frac{\triangle\lambda}{\triangle n} \tag{3.5}$$

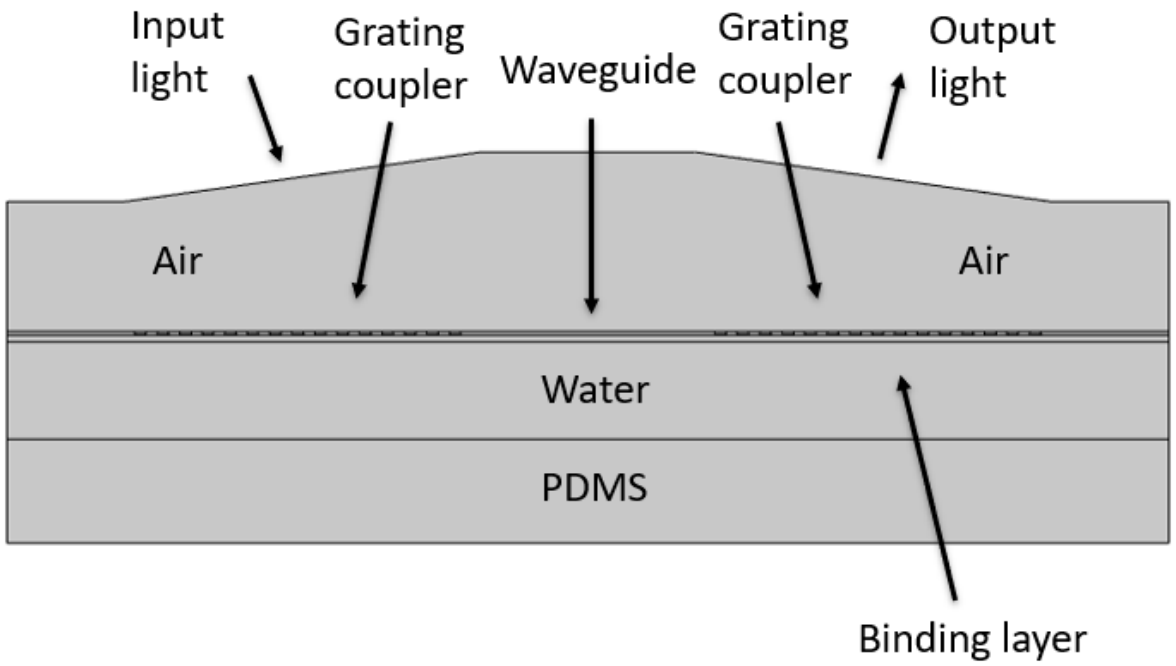

Figure 3.3: Geometry of the microfluidic diffraction grating coupled waveguide based biosensors.

If the coupling angle is changed, it will result in a peak shift in the output spectrum but it will not affect n_{eff} and other parameters. Given the equations above, a structure can be designed to optimize the biosensor performance.

For the model, the optimized grating layer is shown in Figure 3.4 . The RI of the grating and waveguide is 2. Beneath the grating, there is a 200 nm binding layer, a 3 μm water layer and a 3 μm PDMS layer. The 100 nm thick grating coupler consisted of 17 grating periods with a 650 nm period, a 50% fill-factor, and an etch depth of 80 nm. The top of the MDGCW is exposed to air and the input light is incident from the upper left of the air and output from upper right of the air. The length of the waveguide between the two gratings is flexible, and can be adjusted to maximize the interaction length between the binding agent and analyte of interest. Due to the first grating, the incident light is reflected and transmitted into several diffraction orders, and a fraction of the light will be coupled into the waveguide. Between the input and output gratings, the light will propagate through the waveguide. The waveguide is surrounded by air and the binding layer, and it can be

modeled as a dielectric slab waveguide [250]. The guided electric field will be confined in the waveguide and will decay exponentially in the air and the binding layer through evanescent coupling. The light coupled into the waveguide will propagate into the second grating where it will be reflected and transmitted into several diffraction orders again. A fraction of the light will be diffracted out for detection. Both the intensity and wavelength of the output light can be measured to determine the sensitivity of the biosensor.

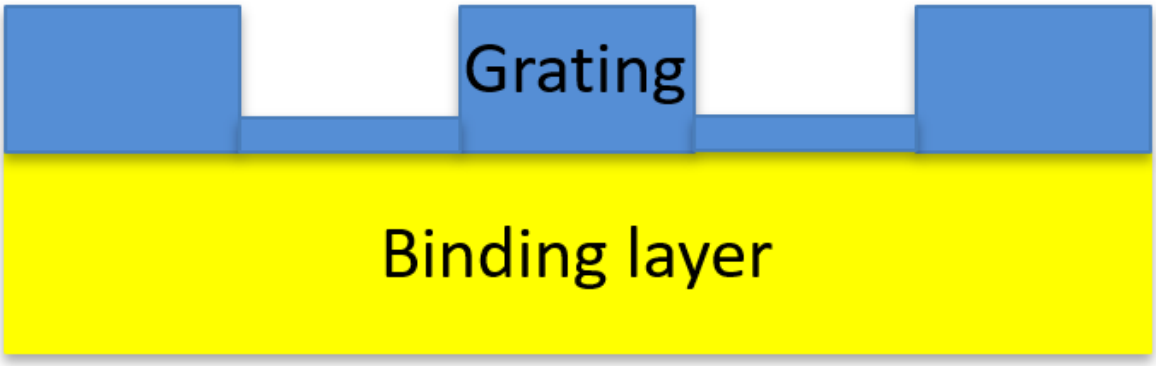

Figure 3.4: Details of the grating design and binding layer.

The COMSOL Multiphysics® Wave Optics module was used to simulate the grating coupler. The light was excited at the upper left side of the air and the transmitted power is detected at the upper right side of the air, as shown in Figure 3.5. The light propagates in the waveguide between two grating couplers as shown in Figure 3.6. A parametric sweep was used to excite different wavelengths of the incident light and scattering boundary conditions were used to reduce the reflection from the boundary. A boundary mode analysis was performed to solve for the propagation constant. The electric field and the propagation constant in COMSOL simulation can be obtained by the Eq. (3.6), Eq. (3.7) and Eq. (3.8):

$$\nabla \times (\nabla \times E) - k_0^2 \varepsilon_r E = 0 \tag{3.6}$$

$$\lambda = -j\beta - \delta_z \tag{3.7}$$

$$E(x, y, z) = \widetilde{E}(x, y) e^{-ik_z Z} \tag{3.8}$$

where k_0 is the free space wave number, ε_r is the permittivity of the material, λ is the eigenvalue, β is the phase constant, and δ_Z is the damping along the propagation direction Z. Eq. (3.6) is the eigenfunction used in the simulations to define the eigenvalue λ which allows us to solve for the electric and magnetic fields.

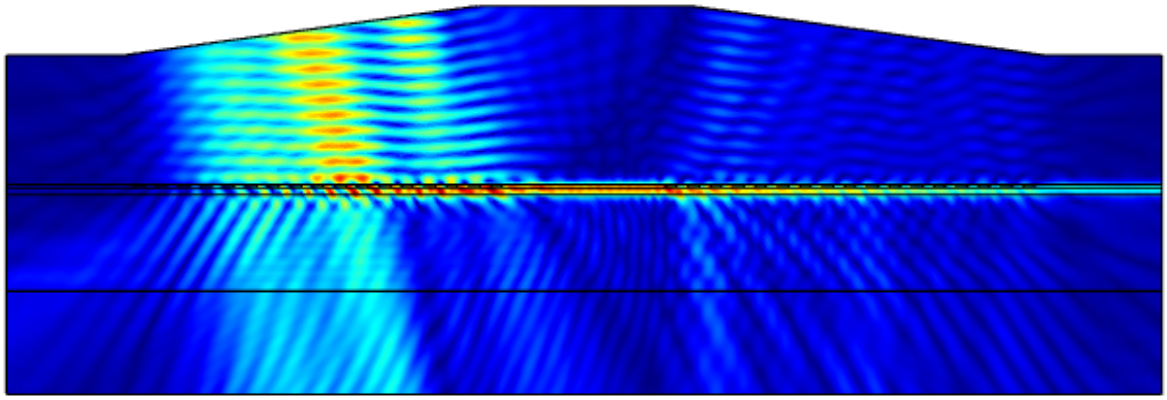

Figure 3.5: Electric field distribution of the diffraction grating coupled waveguide based biosensor.

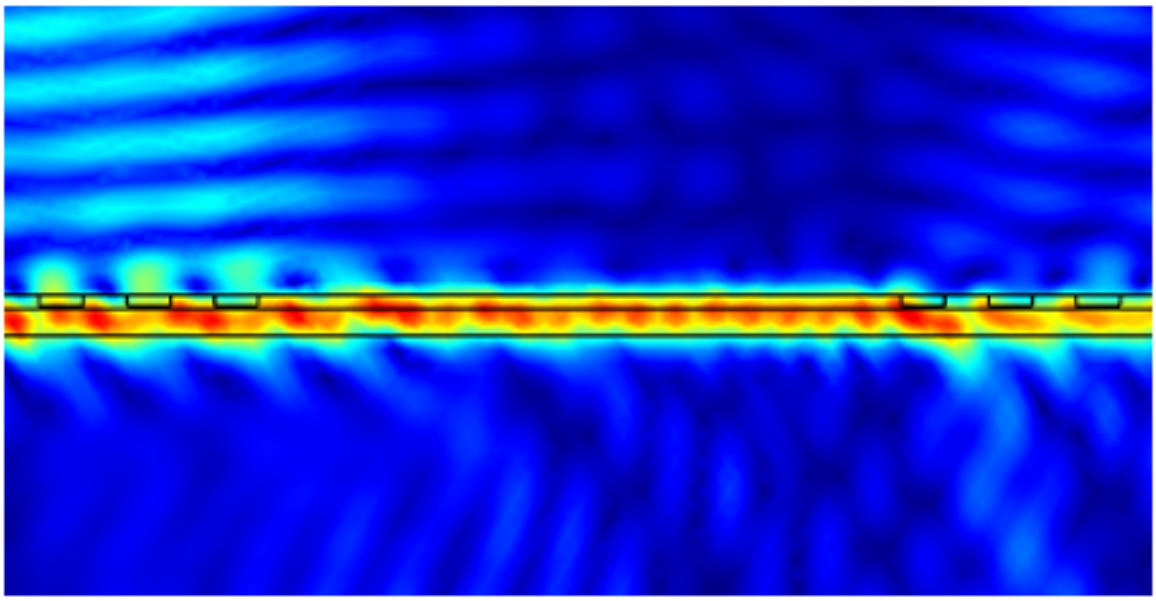

Figure 3.6: Electric field distribution in the waveguide of the sensor.

3.3 Modeling

3.4 Results

Model results indicated good device sensitivity for measurement of the refractive index of the binding layer. Figure 3.7 illustrates the modeling results for the following parameters: $n_g = 2$, $n_{bl} = 1.65, 1.7, 1.75, 1.8$, where n_g and n_{bl} are the refractive indices of the grating and binding layer, respectively. The RI of water is set to 1.33, the RI of air is set to 1 and the RI of PDMS is set to 1.41. The binding layer thickness was set to 200 nm and the coupling angle was 5.7°. The incident wavelength spanned 870 nm to 970 nm. The sensitivity was calculated to be 387nm per refractive index unit. The peak intensity was between 3.5% and 5%, due to the coupling efficiency of the diffraction gratings and propagation losses in the waveguide. Although the reduction in intensity is significant, enough light should exit the biosensor to measure the peak shift.

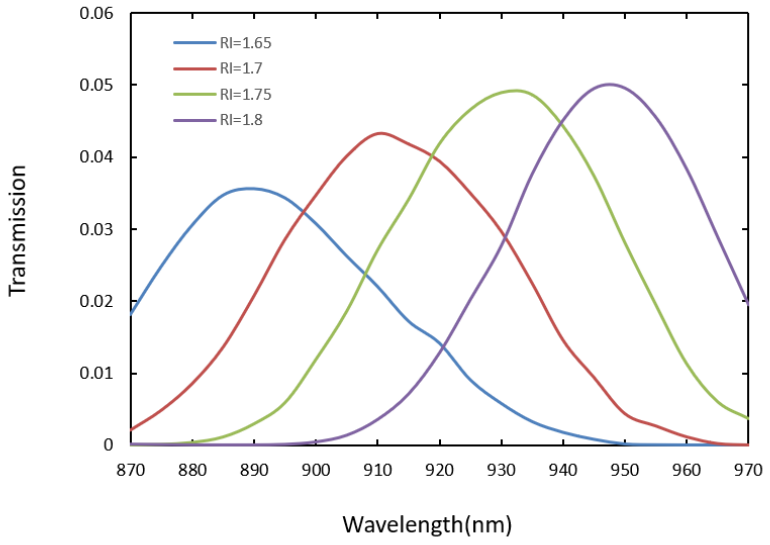

Figure 3.7: Spectrua when binding layer is 200 nm and coupling angle is 5.7°.

Additional simulations were performed where the coupling angle was changed while maintaining the other parameters of interest. Coupling angles of 7.9° and 10.3° were chosen

for simulation to determine the sensitivity of the biosensor to incidence angle. Figure 3.8 and Figure 3.9 illustrate the simulation results for these two angles respectively. Simulations showed that an increasing incidence angle resulted in a blue shifted peak and lower sensitivity. Finally, simulations were performed where the thickness of the binding layer was changed while other parameters remain unchanged. The binding layer thickness impacts the effective refractive index. When the coupling angle was 5.7°, the thickness of the binding layer was set to 100 nm and 150 nm respectively, as seen in Figure 3.10 and Figure 3.11. From the simulation results, it can be seen that the sensitivity of 150 nm was close to the sensitivity of 200 nm, but the sensitivity of 100 nm was much smaller in comparison with the sensitivity of 200 nm. Also the influence of the thickness of binding layer to the peaks were analyzed. The peaks were red shifted with the increased thickness of binding layer, as shown in Figure 3.12. The Figure 3.13 illustrates a comparison of the different incident angles for $n_{bl} = 1.7$. The peaks were blue shifted with the increased angles.

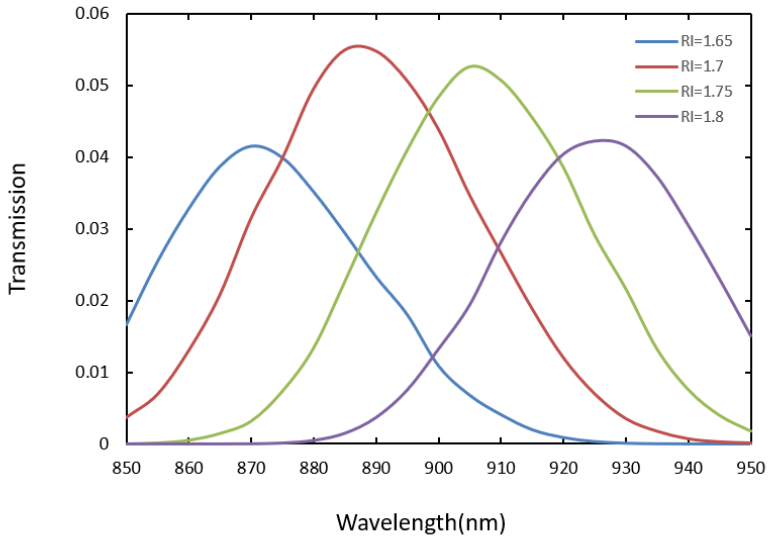

Figure 3.8: Spectrua when binding layer is 200 nm and coupling angle is 7.9°.

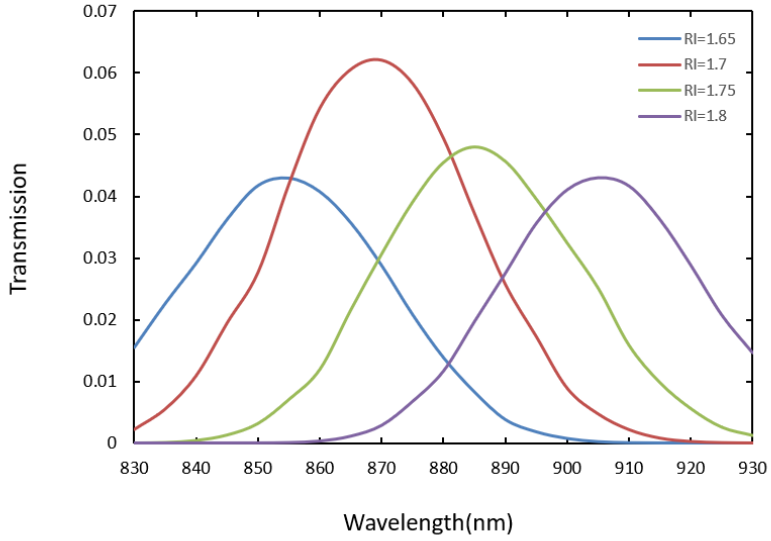

Figure 3.9: Spectrua when binding layer is 200 nm and coupling angle is 10.3°.

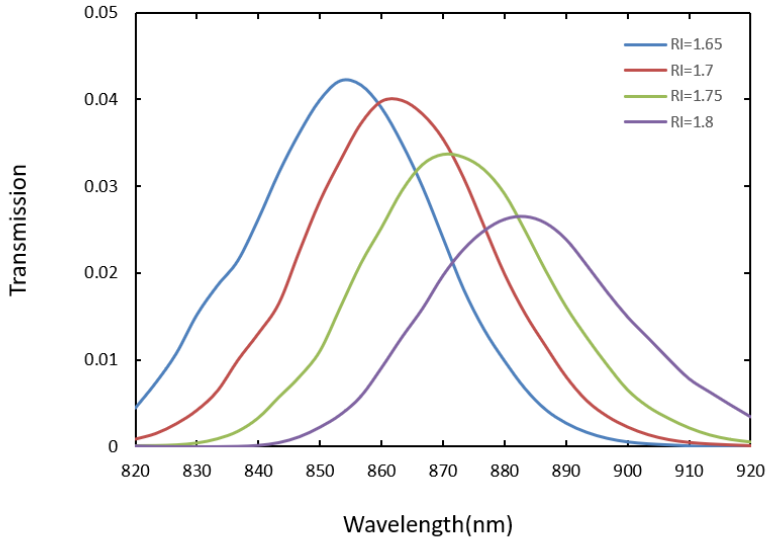

Figure 3.10: Spectrua when binding layer is 100 nm and coupling angle is 5.7°.

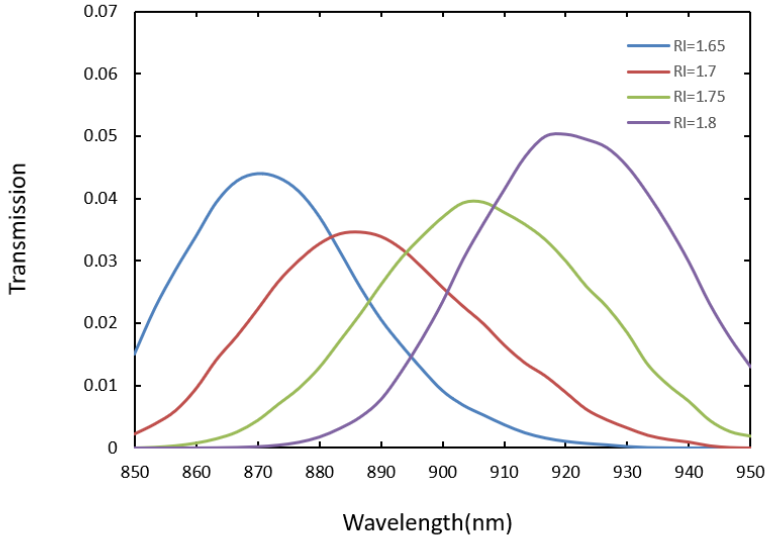

Figure 3.11: Spectrua when binding layer is 150 nm and coupling angle is 5.7°.

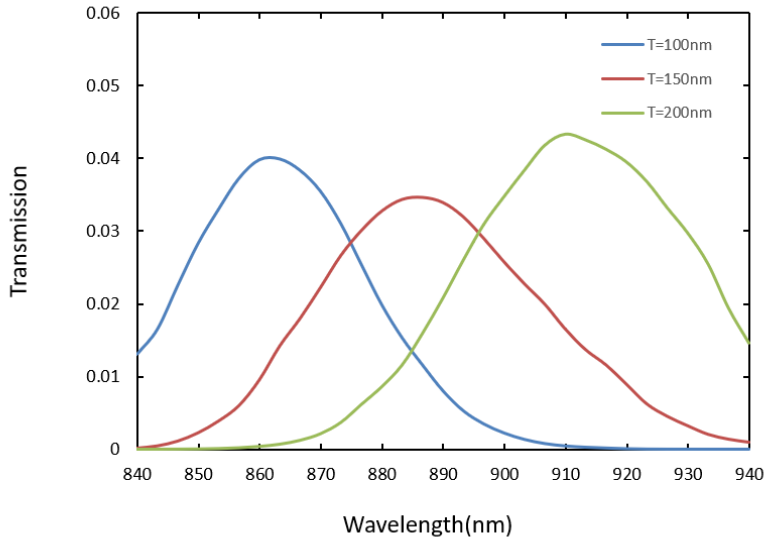

Figure 3.12: Spectrua when the refractive index of the binding layer is 1.7 and coupling angle is 5.7°.

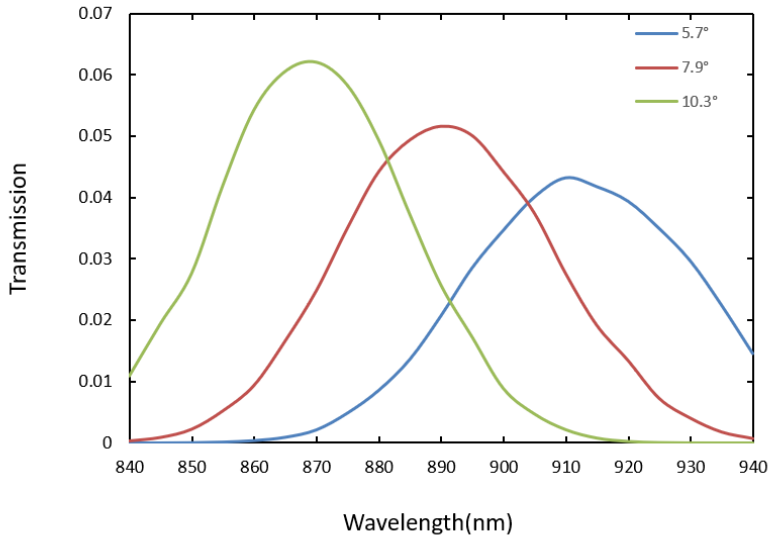

Figure 3.13: Spectra when binding layer is 200 nm and the refractive index of the binding layer is 1.7.

3.5 Summary

A microfluidic diffraction grating coupled waveguide based biosensor which measures the refractive index of the binding layer under the grating was presented. Simulation results have shown that the MDGCW based biosensor should have good sensitivity. As expected, the resulting sensitivity was affected by the refractive index of the binding layer, the dimension of the binding layer, and the coupling angle of the incident light. Although the performance of the MDGCW was reasonable, we chose not to pursue the design further due to equipment availability required for fabrication.

Chapter 4

Two optical waveguide biosensors based on Bragg gratings

4.1 introduction

An optical Bragg grating is a structure with a periodic variation of the refractive index so that a certain wavelength can fulfill the Bragg condition. Many applications are based on Bragg gratings, from communications and information processing to sensing and medical applications [251, 252]. Bragg gratings can be integrated with waveguides to confine the light to enable the creation of sensors [6].

The concept of slot waveguide was first provided by Michal Lipson at Cornell University for confining and enhancing light in a nanometer-scale material with low refractive index [253, 254]. The light intensity in the air slot can be up to 20 times greater than in conventional rectangular waveguides made of the same materials. The interaction between the fundamental modes of the two individual slabs form the slot waveguide eigenmode. The guiding of the light in the core is caused by the imperfect confinement of light. Due to the high refractive index contrast, the component of the electric field normal to the interface of air and silicon shows a large discontinuity at the boundary and the light intensity is significantly higher in air close to the air/silicon interface. When two silicon slabs are designed enough close to each other, they can form a slot in between them. The eigenmode that is formed by the two discontinuities interaction and can be applied in the fields of optical biosensors, optofluidic filters, and optical trapping.

This chapter details the design, simulation and fabrication of two waveguide biosensors based on Bragg gratings, which are able to detect analytes with different refractive indices by integrating the techniques mentioned above. The DSBGW is designed to integrate Bragg gratings with waveguides on SOI wafers to measure the analyte surrounding the waveguide.

The TM mode light in the waveguide structure fully interacts with the analyte and the Bragg gratings to achieve high sensitivity of the sensor. Compared with the DSBGW, a DSBGISW based biosensor is based on a slot waveguide where the analyte interacts with the TE mode light. The analyte can be liquid or biomolecules of different refractive indices. The chapter is organized as follows: Section 4.2 describes the configuration and modeling of a basic grating coupler to help the light input to the biosensor, Section 4.3 discusses the configuration of the DSBGW and DSBGISW, Section 4.4 details the simulation results of the DSBGW and DSBGISW, section 4.5 shows the explanation of the results, Section 4.6 provides the fabrication process of the these two biosensors, Section 4.7 provides the future experimental set up to combine the grating coupler and biosensors for the measurement. At last, Section 4.8 provides the brief summary of the chapter.

4.2 The configuration and modeling of the grating coupler

The grating coupler structure chosen for simulation consisted of a silicon grating coupler, a top air layer, a silicon dioxide layer and silicon substrate, as shown in Figure 4.1. As shown in Figure 4.2, the 220 nm thick grating coupler with a coupling angle 8° consisted of 19 grating periods with a 630 nm period, a 50% fill-factor, an etch depth of 80 nm. The region connecting to the grating coupler was regarded as the waveguide. The waveguide, which was modeled as a dielectric slab waveguide, was surrounded by air and silicon dioxide. The top of the grating coupler was exposed to air and the input light was incident from the upper left of the air and output was measured from right part of the waveguide.

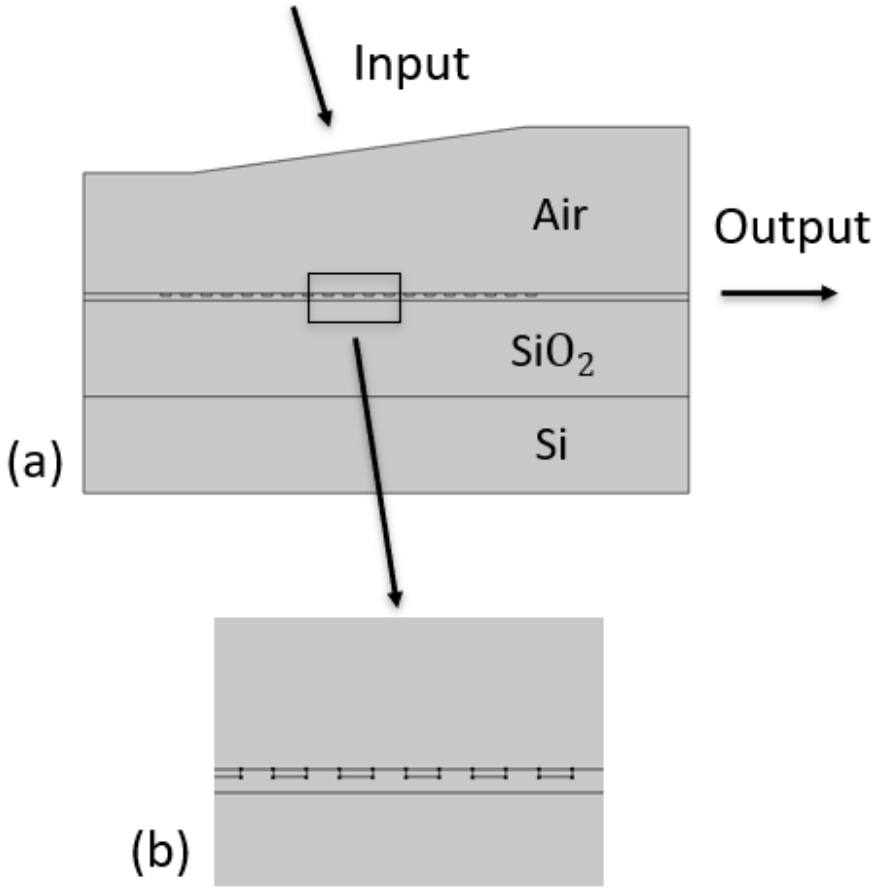

Figure 4.1: Geometry of the grating coupler.

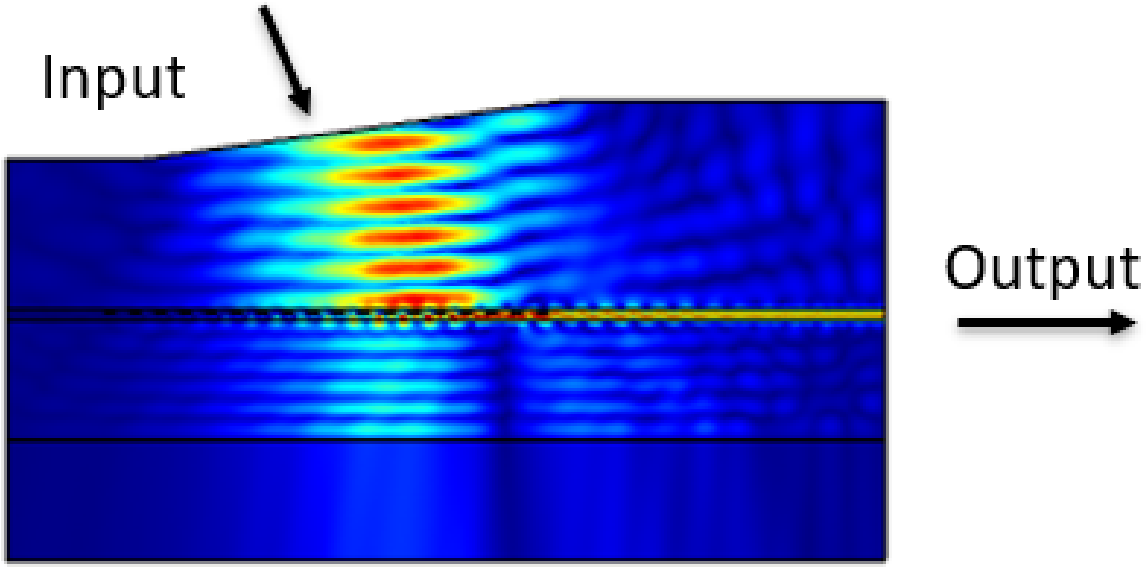

Figure 4.2: Electric field distribution of the grating coupler.

The COMSOL Multiphysics® Wave Optics module was used to simulate the grating coupler. The model used COMSOL's boundary mode analysis. A parametric sweep was used to excite different wavelengths of the incident light and scattering boundary conditions were used to reduce the reflection from the boundary. A boundary mode analysis was performed to solve for the propagation constant. The electric field and the propagation constant in COMSOL simulation also can be obtained by the mentioned equations Eq. (3.6), Eq. (3.7) and Eq. (3.8). The light was excited at the upper left side of the air and the transmitted power is detected at the right side of the waveguide, as shown in Figure 4.3. When the light reaches to the gratings, the incident light is reflected and transmitted by the gratings into several diffraction orders, and a part of the light will be coupled into the waveguide and propagate in the waveguide. Simulation results indicated good coupling efficiency around a wavelength 1560 nm. The peak transmission was close to 50% and the 1 dB bandwidth exceeded 40 nm due to the diffraction gratings, the coupling efficiency and the propagation losses.

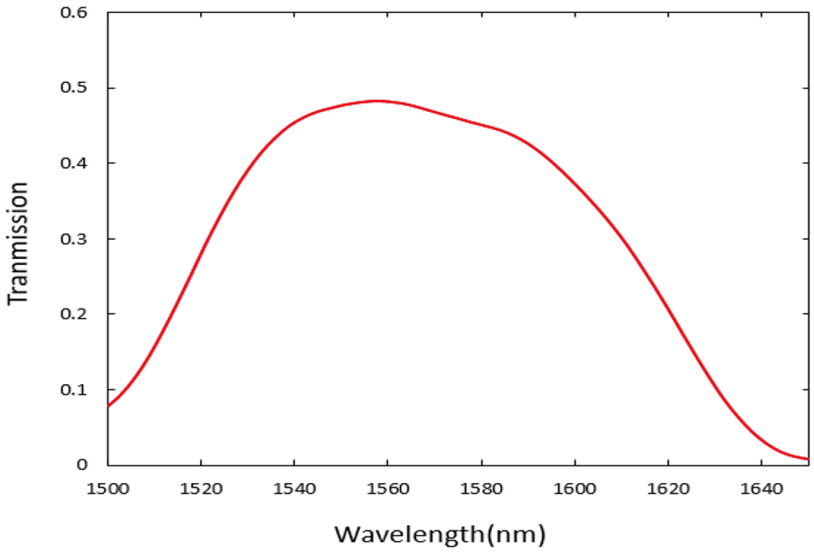

Figure 4.3: The output spectrum when the grating coupler with a coupling angle 8° consisted of 19 grating periods with a 630 nm period, a 50% fill-factor, an etch depth of 80 nm.

4.3 The configuration of two biosensors

In terms of the basic structure of the DSBGW, the top view of the DSBGW is shown in Figure 4.4a. The waveguide (grey part) surrounded with the analyte (yellow part) had the length of 1000 μm and width of 800 nm. Each sidewall of the waveguide consisted of 1500 grating periods with a 640 nm period, a 50% fill-factor and an etch depth of 700 nm. For the real experiment, the biosensor will be connected with two grating couplers. The light of TM mode is input from the left grating coupler connected with the waveguide, then the light propagates in the biosensor and is coupled out from the grating coupler on the right side of the waveguide, as shown in Figure 4.4c. For real experiment, the thickness of the waveguide was 220 nm as shown Figure 4.4b,

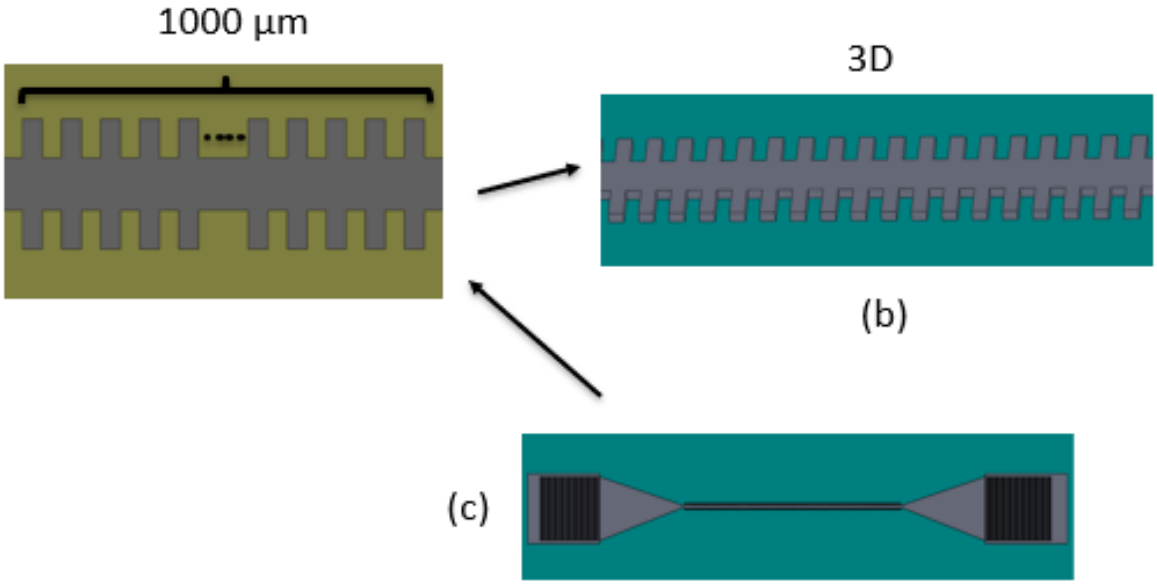

Figure 4.4: (a) The structure of DSBGW. (b) 3D view of the structure on the substrate (without the analyte). (c) when the sensor structure integrated with two grating couplers.

In terms of the basic structure of the DSBGISW, a slot was inserted in the middle of the waveguide, and the top view of the structure is shown in Figure 4.5a. The grey part was the waveguide and sidewall gratings, and all the yellow parts were the analyte analyzed. The total length of the waveguide was 100 μm with a width of 800 nm and the waveguide was surrounded with the analyte. Each side of waveguide consisted of 80 grating periods

with a 1180 nm period, a 50% fill-factor and an etch depth of 570 nm. When the biosensor is connected with the grating couplers, the light of TE mode is input from the left grating coupler connected with the waveguide and is output from the grating coupler on the right side of the waveguide, as shown in Figure 4.5c. For real experiment, the thickness of the waveguide was 220 nm as shown in Figure 4.5b.

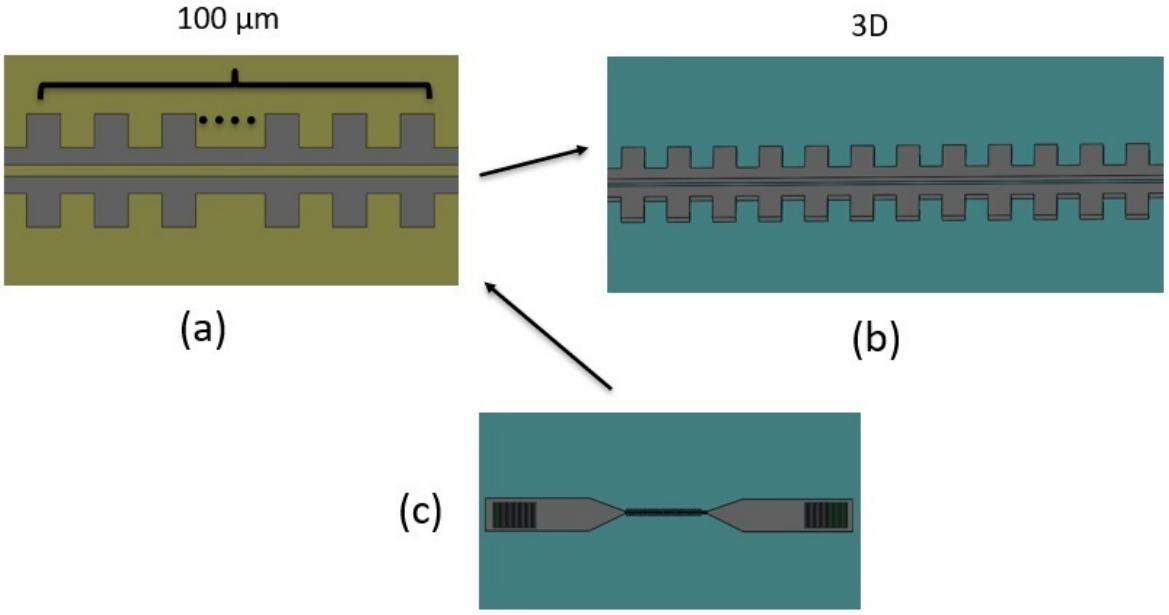

Figure 4.5: (a) The structure of DSBGISW. (b) 3D view of the structure on the substrate (without the analyte). (c) When the sensor structure integrated with two grating couplers.

4.4 The modeling and simulation results

The COMSOL Multiphysics® Wave Optics module was also used to simulate these two biosensors. The model used COMSOL's boundary mode analysis. A parametric sweep was used to excite different wavelengths of the incident light and perfect matched layer were used to reduce the reflection from the boundary.

The simulation of the DSBGW showed that the light was confined in the waveguide and Bragg gratings, and that it interacted with the analyte around the structure. For the TM mode, Figure 4.6a and Figure 4.6b show the input and output parts of the electric field when the light has good resonance with the DSBGW, respectively, while Figure 4.6c and Figure

4.6d present input and output parts of light that is significantly filtered by the DSBGW when the grating period was 1500 with fill factor 50%. The biosensor structure consisted of 1500 grating periods with grating period of 640 nm, a 50% fill factor and grating height of 700 nm and the width of the waveguide of 870 nm. To understand the influence of the number of gratings, a sensor with 500 grating periods and a sensor with 1500 grating periods were simulated, as shown in Figure 4.7. The DSBGW with 1500 periods showed better quality factor and the intensity of the transmission was still close to 60%. Then the height of the gratings was set 600 nm, 700 nm and 800 nm respectively to determine the influence of the height of the gratings on the biosensor. As shown in Figure 4.8, when the height was 700 nm, its quality factor was maximized while providing high transmission. Also the contribution of the width of the waveguide on the biosensor was evaluated where the width of the waveguide was set as 820 nm, 870 nm, 920 nm respectively, and the peaks are red shifted with increased width, as shown in Figure 4.9. Finally the biosensor is tested with different refractive indices of the analyte, RI = 1.33, 1.38 and 1.43 to show the sensor performance, as shown in Figure 4.10. After the simulation, a sensitivity of 255 nm/RIU was obtained with a quality factor was close to 500. Furthermore, for the TE mode at RI = 1.38, the transmission is less than 2% at the position of the peak in TM mode, as shown in Figure 4.11. Thus the propagation of TE mode will not affect the sensor performance.

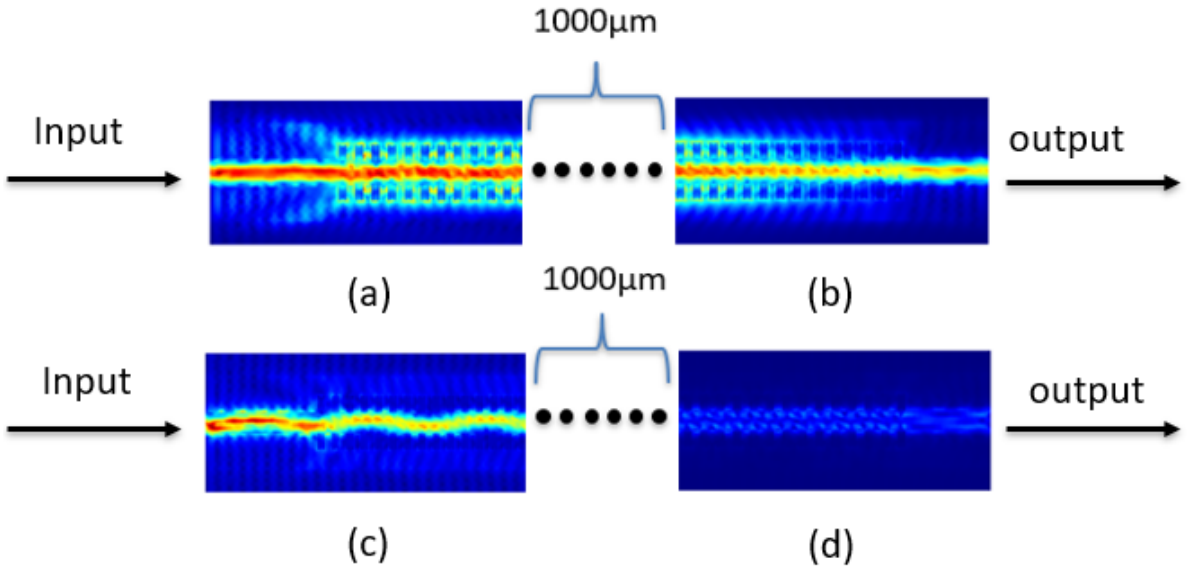

Figure 4.6: (a) Input part of electrical field when the light resonates with the DSBGW. (b) Output part of electrical field when the light resonates with the DSBGW. (c) Input part of electrical field when the light is significantly filtered by the DSBGW. (d) Output part of electrical field when the light is significantly filtered by the DSBGW.

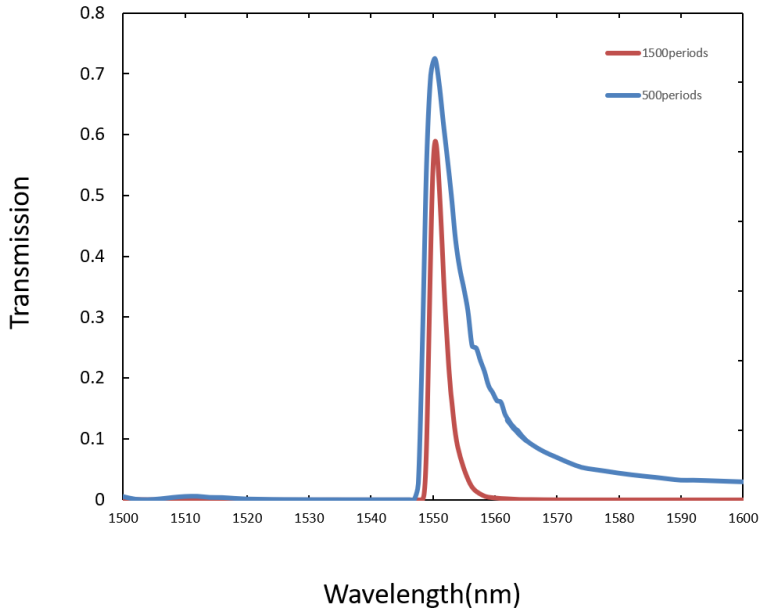

Figure 4.7: The output spectra of one DSBGW with 1500 periods gratings and one with 500 periods gratings.

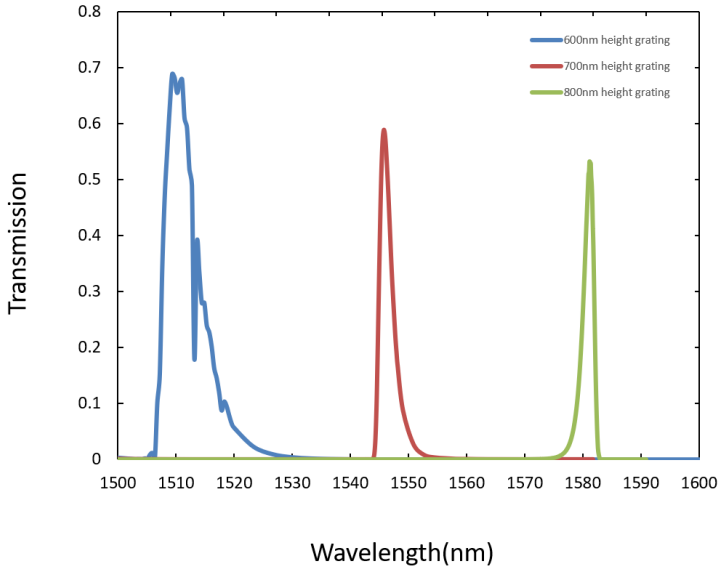

Figure 4.8: The output spectra when 600 nm, 700 nm and 800 nm are the grating height of the DSBGW with 1500 periods grating.

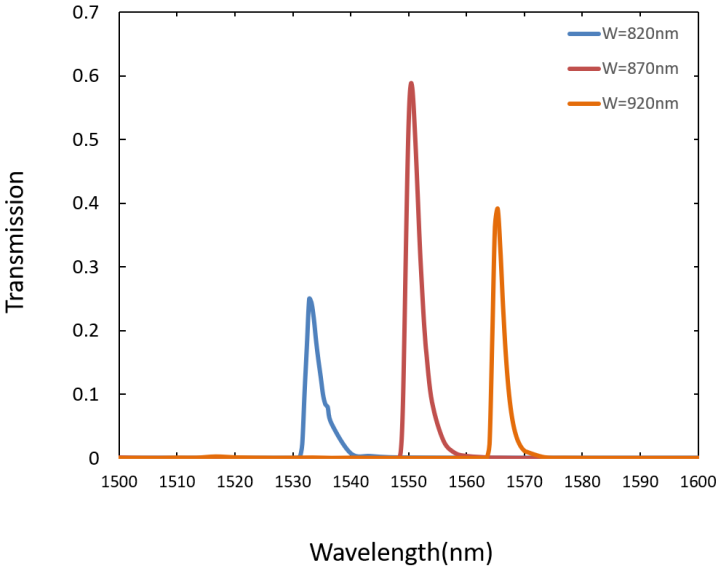

Figure 4.9: The output spectra of DSBGW when the width of the waveguide is 820 nm, 870 nm and 920 nm with 1500 periods gratings.

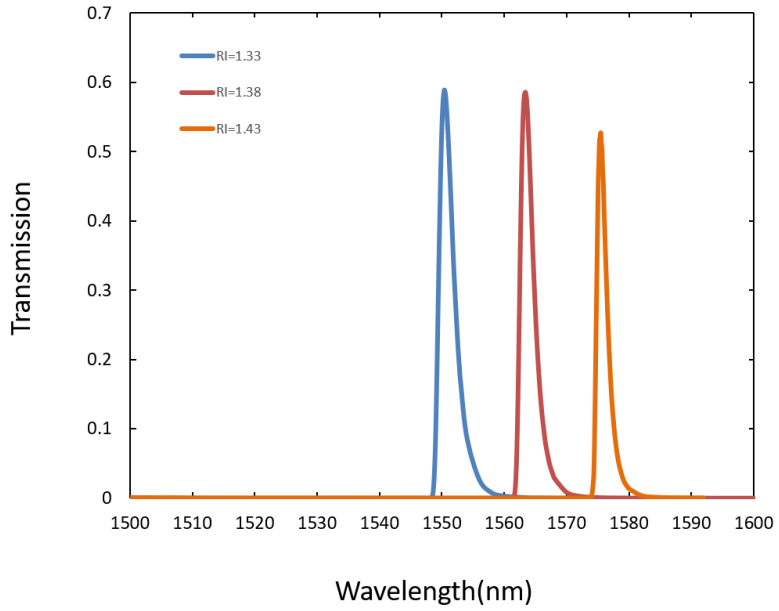

Figure 4.10: The output spectra of DSBGW when the cladding RI = 1.33, 1.38 and 1.43 of the waveguide structure with 1500 periods gratings.

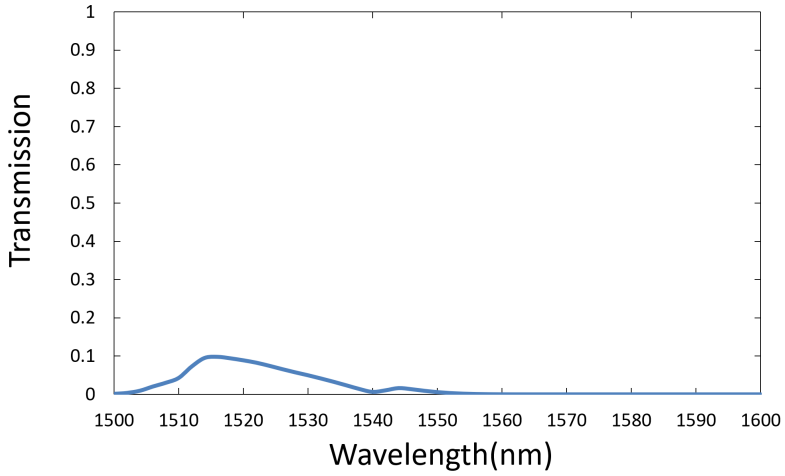

Figure 4.11: The output spectrum when the TE mode light is used in the DSBGW simulation.

The simulation of the DSBGISW showed that the light was confined in the slot waveguide and Bragg gratings and interacted with the liquid around the gratings and the slot. For

the TE mode, Figure 4.12a and Figure 4.12b show the input and output parts of the electric field when the light resonated with the DWBGW, respectively, while Figure 4.12c and Figure 4.12d present input and output parts of the light significantly filtered by the DWBGISW. For this simulation, the RI of silicon and the RI of the liquid were set to 3.46 and 1.43 respectively. The biosensor structure consisted of 80 grating periods with grating period of 1180 nm, a 50% fill factor and grating height of 590 nm and the width of the waveguide of 820 nm with a 220 nm width slot inside. As shown in Figure 4.13, three different peaks, within a wavelength span from 1500 nm to 1600 nm, are shown in the spectrum. At first, The grating periods were set 40, 80 and 160 respectively to research the impact of the number of grating periods on the biosensor. Based on the simulation, the peaks were in the same position and more grating periods led to better quality factor and worse transmission, thus 80 periods can provide the biosensor with a good quality factor and enough light transmission. The height of the gratings and the width of the waveguide were simulated to determine the effect on performance. The peaks were red shifted as the height was set as 570nm, 590nm and 610nm, as shown in Figure 4.14. The peaks were also red shifted when the waveguide width was set as 800 nm, 820 nm and 840 nm, as shown in Figure 4.15. Furthermore, the width of the slot also affected the position of the peaks. Each slab was was set to 300 nm and the slot width was set as 180 nm, 220 nm and 260 nm. As shown in Figure 4.16, the peak red shifted with the increased slot width, and a slot width 220 nm was chosen to optimize the quality factor and transmission. Finally, the influence of the different refractive indices of the analyte, RI = 1.33, 1.38, 1.43 and 1.48 were analyzed on the biosensor. The peaks red shifted when the RI increased, as shown in Figure 4.17 and a sensitivity of 190 nm/RIU with quality factor close to 600 was noted. When the refractive index was set to 1.38, for TM mode light, the transmission was less than 1%, as shown in Figure 4.18, so the resonance peak in DSBGISW was only caused by TE mode.

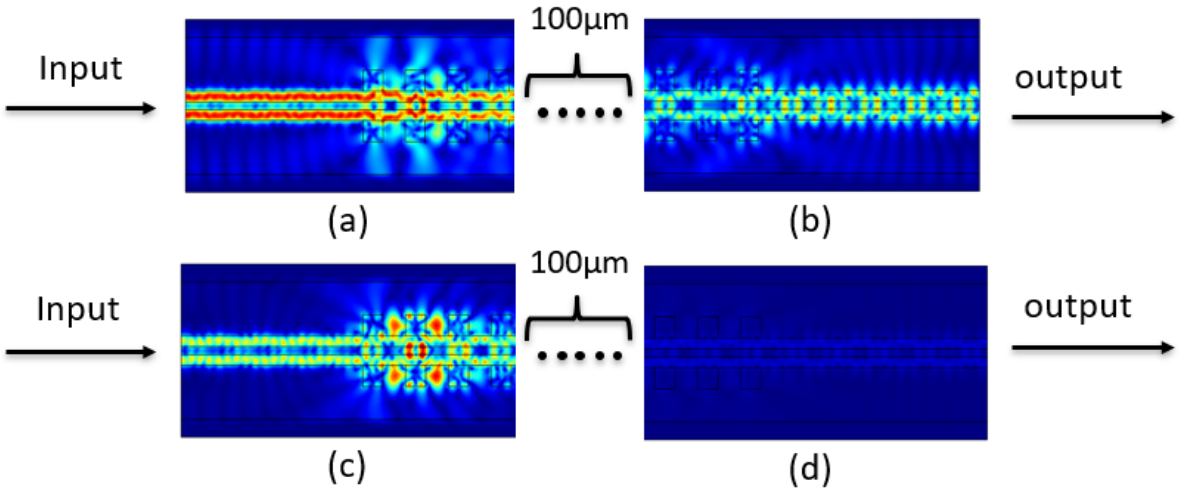

Figure 4.12: (a) Input part of electrical field when the light resonates with the DSBGISW. (b) Output part of electrical field when the light resonates with the gratings in the DSBGISW. (c) Input part of electrical field when the light is significantly filtered by the DSBGISW. (d) Output part of electrical field when the light is significantly filtered by the DSBGISW.

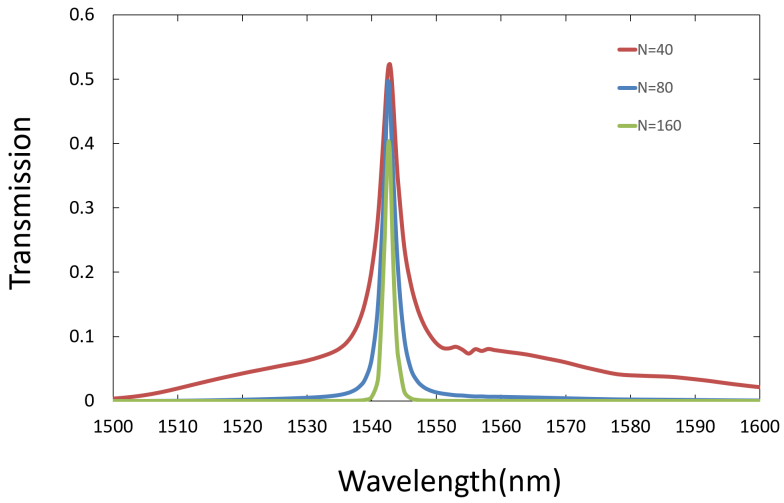

Figure 4.13: The output spectra when the number of grating periods of the DSBGISW is 40, 80 and 160.

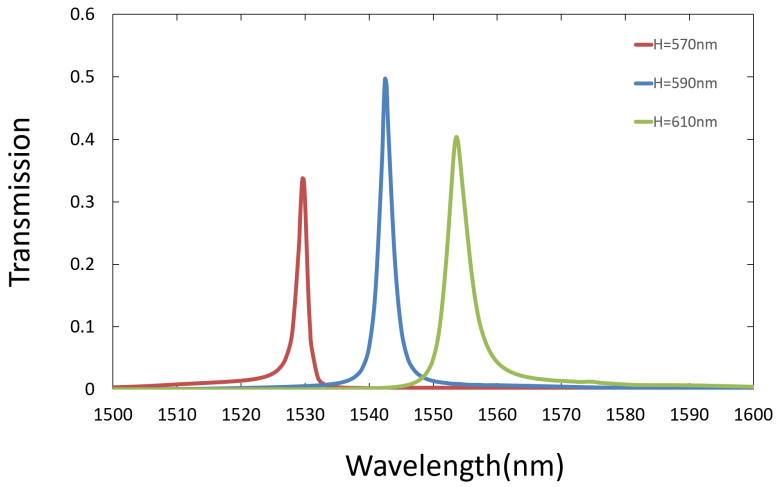

Figure 4.14: The output spectra when 570 nm, 590 nm and 610 nm are the height of the gratings of the DSBGISW with 80 periods gratings.

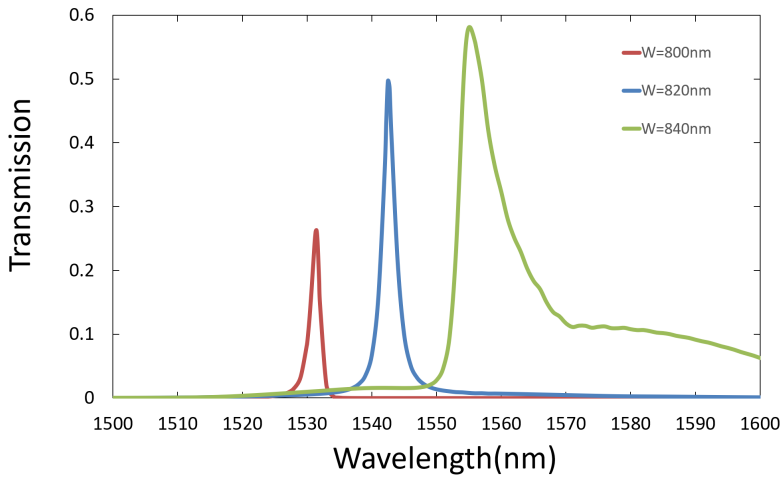

Figure 4.15: The output spectra when 800 nm, 820 nm and 840 nm are the width of the waveguide of the DSBGISW with 80 periods gratings and 220 nm width slot.

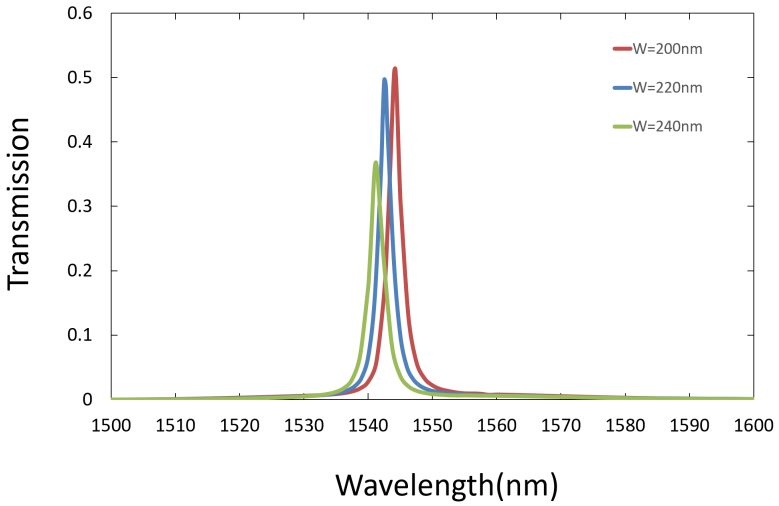

Figure 4.16: The output spectra when slot width is 200 nm, 220 nm and 240 nm with 300 nm slab width.

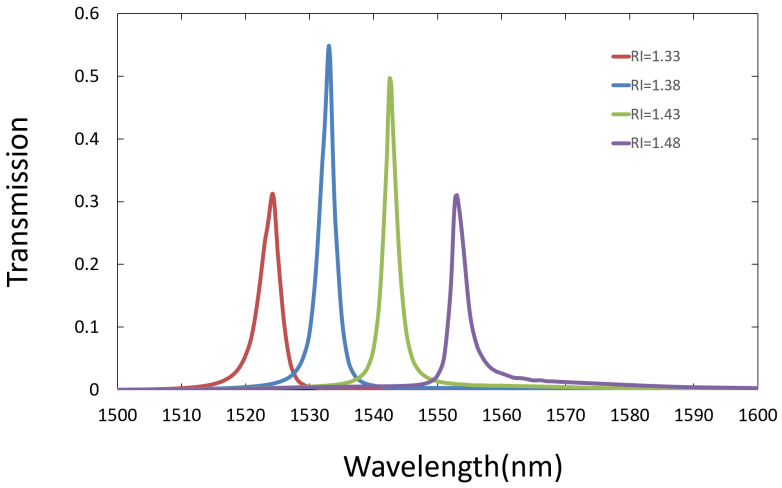

Figure 4.17: The output spectra when the cladding and slot RI = 1.33, 1.38, 1.43 and 1.48.

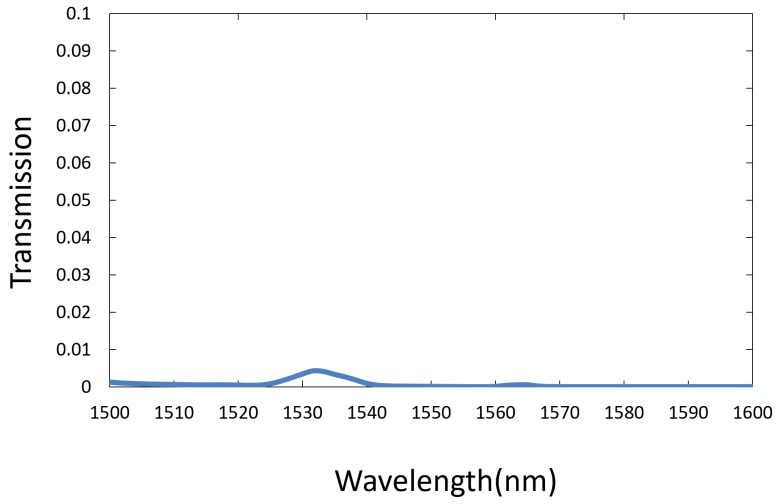

Figure 4.18: The output spectrum TM mode light is applied in the DSBGISW simulation.

4.5 Discussion of the results

The equations below describe how the light is confined and interacts with the double sided Bragg grating structure [255]:

$$\kappa = (\frac{n_{grating}}{\overline{n_{Bragg}}})^2 \frac{2}{\lambda} \cdot sin(\pi \cdot DC) \cdot \gamma \cdot (n_{core} - n_{clad}) \tag{4.1}$$

$$n_{grating} = \sqrt{{n_{core}}^2 \cdot \left(\frac{DC}{2}\right) + {n_{clad}}^2 \cdot \left(\frac{1 - DC}{2}\right)} \tag{4.2}$$

Where $\overline{n_{Bragg}}$ is the effective index of the material specifically at the Bragg wavelength, $n_{grating}$ is the waveguide index for the alternating grating regions, γ is the fraction of the power of the mode within the alternating grating regions, DC is the duty cycle, λ is the wavelength, n_{core} is refractive index of the core and $n_{cladding}$ is the refractive index of the cladding. From Eq. (4.1) and Eq. (4.2), the coupling efficiency κ will increase with the greater difference between n_{core} and $n_{clading}$ due to better confinement of the light. By calculating Eq. (4.1), the coupling efficiency will reach a maximum when the duty cycle is set to 0.5. Furthermore, in Eq. (4.1), the fraction of the power of the mode γ is related

to the region of alternating wide and narrow gratings, so the mode power is determined by the parameters of Bragg gratings and waveguide. From Eq. (3.4), the change of effective index will be determined by the RI of analyte and the phase of the light, and it will influence the propagation mode of the light in the waveguide. As seen from the simulation results, additional gratings produce a higher quality factor but worse transmission, which can be explained by the longer resonance distance and propagation loss. Also, for both biosensors, a larger waveguide width, bigger grating period and taller gratings can lead to the red shift of the peaks. Due to the difference of the light propagation in the waveguide and the interaction with analyte and Bragg gratings between TE and TM modes, the DSBGW has better sensitivity than DSBGISW and less propagation loss, but it needs many more grating periods to reach a good quality factor. Compared with DSBGW, the DSBGISW can reach good quality factor with less grating periods, thus it can reduce the total loss during the light propagation caused by the fabrication tolerance for real experiments. Also the slot waveguide inside DSBGISW can concentrate the electric field inside the structure, enlarge the area of light interaction between the TE mode and the analyte which leads to increase field overlap and higher sensitivity [6].

4.6 Fabrication process

A Raith^{TM} e-LiNE e-beam lithography (EBL) system was used to pattern the wafer to form the Bragg gratings structure, as shown as Figure 4.19. A block diagram of a typical electron beam lithography system is shown as Figure 4.20. The column is set for forming and controlling the electron beam. A column typically consists of an electron source, several lenses, apertures to define the beam, a blanker to turn the beam on and off, a mechanism system to deflect the beam, a stigmator to remove the astigmatism in the beam, alignment systems to make the beam at the center in the column and an electron detector to focus and locate marks on the sample. The chamber under the column has a stage for moving the sample around provides access for loading and unloading samples. The entire system

is kept under vacuum during operation. A rack of electronics supplies power and signals that are connected to the various parts of the machine. Finally, the system is controlled by a computer, which operates diverse functions, such as exposure function, loading and unloading procedures, aligning and focusing the electron beam, and sending the mask and pattern data to the pattern generator. The part of the computer and electronics designed to operate pattern data is referred to as the datapath. The main steps of the EBL procedure include loading samples, defining the voltage of the beam, choosing the spot size, focusing the sample through adjusting the working distance and by correcting the astigmatism, doing write field alignment by adjusting the electromagnetic/electrostatic deflection system to the X-Y-Z position of the precision laser stage, measuring the beam current and achieving exposure to the sample.

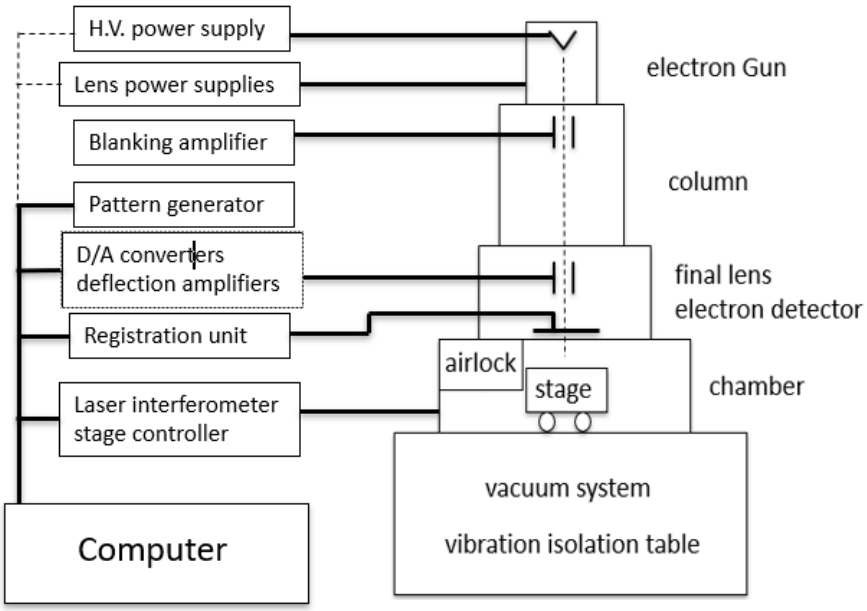

Figure 4.19: Major components of a typical commercial e-beam lithography system.

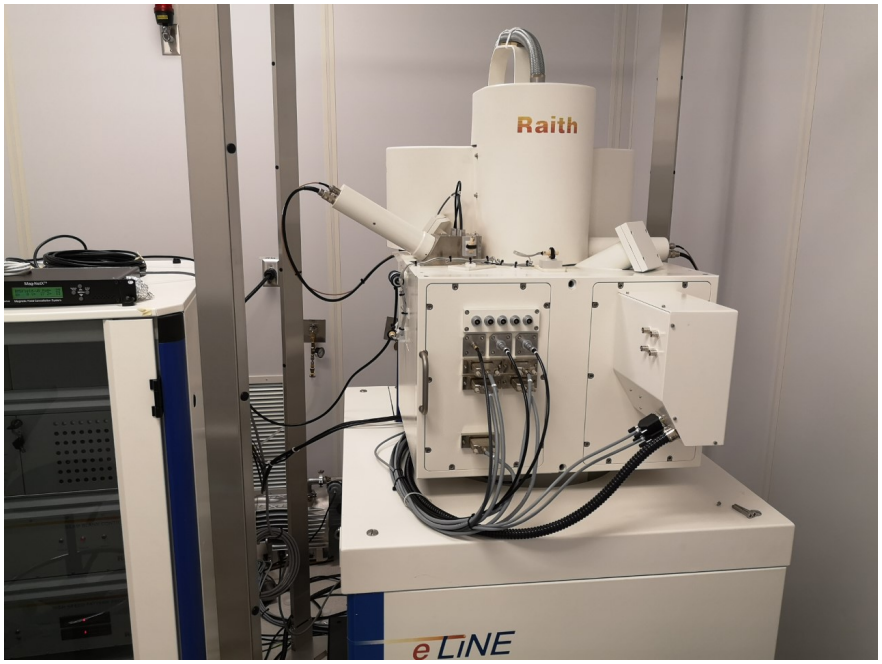

Figure 4.20: The image of A Raith^{TM} 150 e-beam lithography system.

To fabricate both biosensors on SOI wafer, the 220 nm silicon device layer needed to be etched through. Most of the surface area will be etched so features of the biosensor will must be protected from the gas etchant by a mask material during the etching. For the fabrication, 20 nm Cr film was chosen as the metal mask for the etch process and liftoff process was applied to generate the mask structures. Liftoff is a process to expose on a sacrificial layer and then transfer the thin film, such as the metal, to the exposed area to create the structure. Due to the resolution requirement for the pattern, the e-beam resist must be very thin during the exposure which causes issues when a typical one-layer liftoff process is used to obtain the mask. In this research, a two-layer stack, where the bottom layer is undercut during resist development, is used to obtain a better result. This is known as bilayer lift-off process. A 1 cm $\times$ 1 cm SOI wafer (blue)Figure 4.21a was used as a substrate and 495 polymethyl methacrylate (PMMA) A2 by MicroChem^{TM} was used as the bottom layer of the bilayer (red)(Figure 4.21b). The resist was spun at 1600 rpm for 45 s for a thickness after baking at 180°C for 5 mins of 70 nm. Then 950 PMMA A2 by MicroChem^{TM} was used as the top layer of the bilayer (orange)(Figure 4.21c). The resist was spun at 3000

rpm for 45 s for a thickness after baking at 180°C for 5 mins of 72 nm. Then the mask of the waveguide structure were patterned using EBL, as shown in Figure 4.21d. After the development of the resist, the bottom layer was undercut and was ready to perform the lift-off process. Then 20 nm Cr (gray) was deposited by e-beam evaporation, as shown in Figure 4.21e. The wafer was then immersed into acetone in an ultrasonic bath for 10 mins to remove all the resist. The completed lift-off process produced the Cr structure on the surface of the wafer to obtain the mask, as shown in Figure 4.21f. The image of the Cr mask after lift-off process by SEM is shown in Figure 4.22.

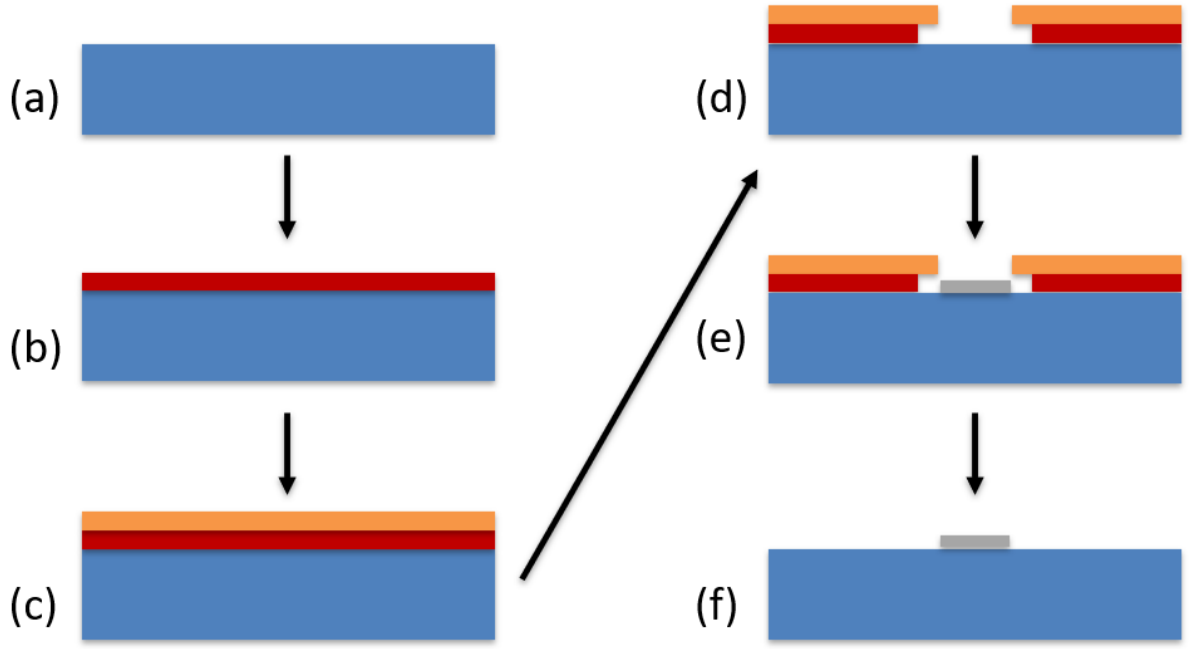

Figure 4.21: (a) A SOI wafer is prepared. (b) 495 PMMA A2 is spined on the wafer. (c) 950 PMMA AA2 is spined on the layer of 495 PMMA A2. (d) The bilayer resist was patterned by e-beam lithography. (e) A 20nm Cr film was deposited. (f) The bilayer resist was removed by Acetone ultrasonic bath.

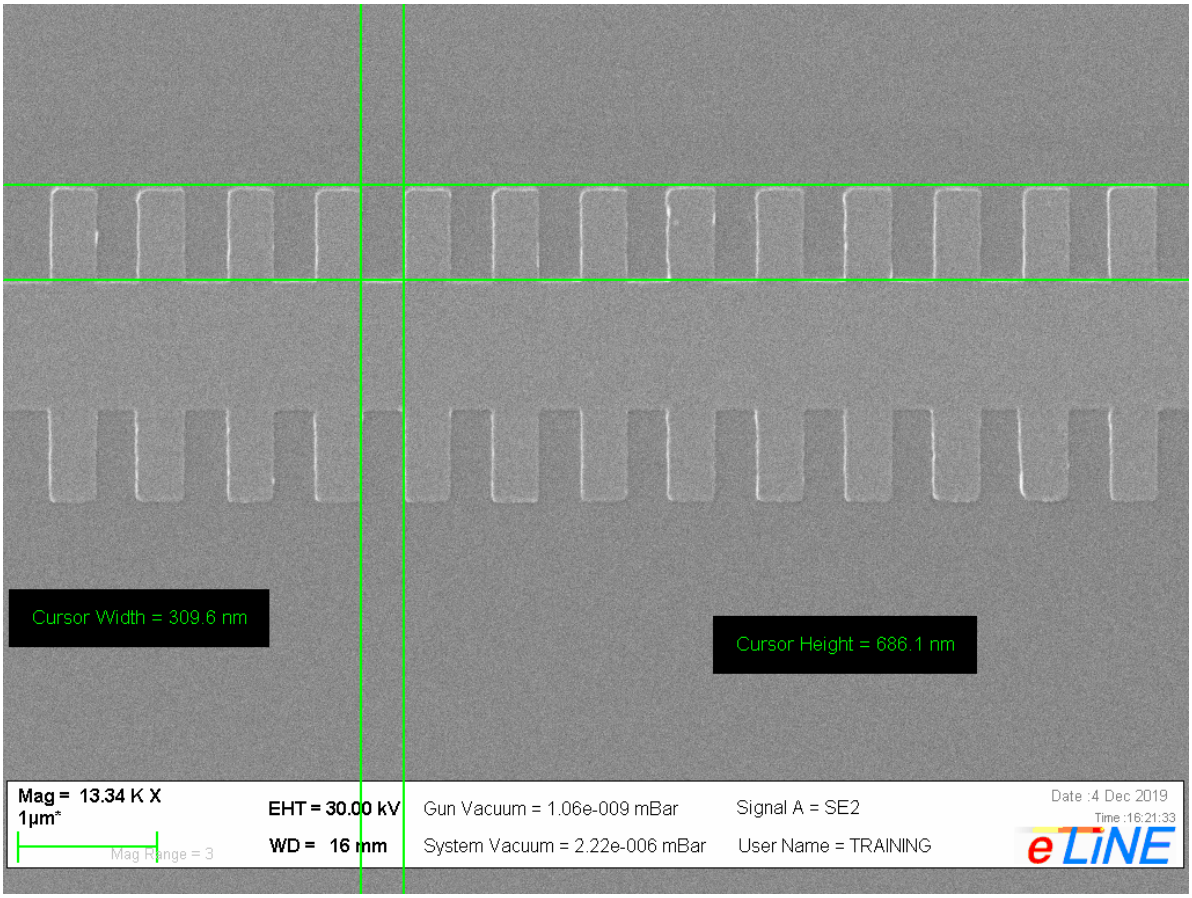

Figure 4.22: The image of the Cr mask after lift-off process by SEM.

4.7 Future work

The Cr mask will allow the biosensors structure to be fabricated through a dry etching process. Then the sample will be patterned again to generate the Cr mask for the grating coupler and etched to produce the grating coupler as well. For both Cr masks, after the etching process, the samples will be put into Cr etchant to remove the Cr mask. For the DBSGW biosensor, the etched sample will be shown as Figure 4.23a, the details of grating coupler and DBSGW are shown as Figure 4.23b and Figure 4.23c respectively. Then the samples can be prepared for experimental validation.

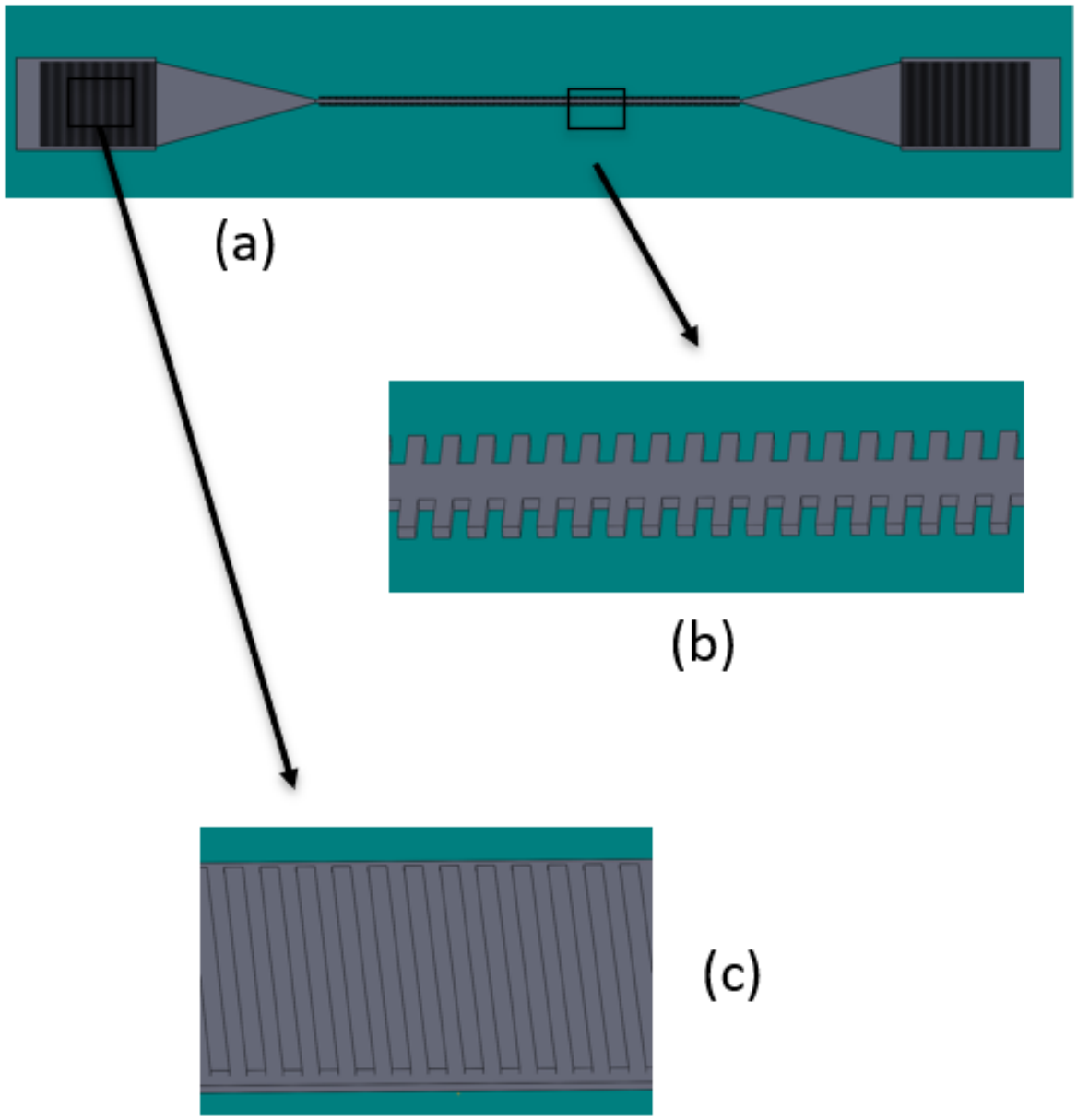

Figure 4.23: (a) The structure of etched DSBGW. (b) Detail of Grating coupler. (c) Detail of DSBGW.

For the experiment, both sensors will be placed in the test appartus, as shown in Figure 4.24. Two single mode optical fibers are placed on a 3-axis stage (by Thorlabs^{TM}) which allows for accurate positioning of the fibers. One single-mode fiber (with core diameter of 8.5 μm) will connect the sensor input with a tunable laser (IQTLS by Coherent Solutions). Another single-mode fiber (with core diameter of 8.5 μm) is connected to the sensor output

and the signal is transmitted to a spectrum analyzer (AQ6370D by Yokogawa). With help of two 3D printed holders, the input single-mode fiber will be aligned with the input grating coupler and the output single-mode fiber will be aligned with the output grating coupler to receive the light. The angle of the fiber with the sensor on the stage will be set to 8°, and the sensor will be illuminated by the tunable laser over a range from 1527.6 nm to 1567.2 nm.

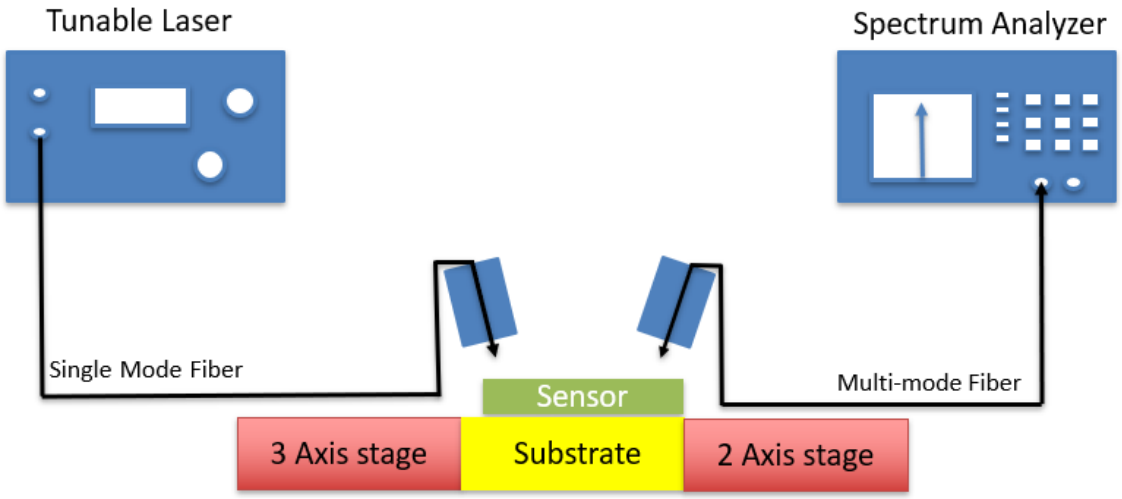

Figure 4.24: Future optical setup for testing sensor

4.8 Summary

Two different waveguide biosensors based on Bragg gratings are presented in this chapter. The DSBGW based biosensor is built on a SOI wafer to produce the resonance, resulting in the peak in the spectrum to measure the analytes of different refractive indices with 255 nm/RIU sensitivity. The height of the gratings and width of the waveguide both influence the position of the peaks. The DSBGISW based biosensor integrates the Bragg gratings with a slotted waveguide on a SOI wafer to generate the resonance in TE mode to measure the analytes of different refractive indices with 190 nm/RIU sensitivity. The parameters of the gratings, the width of the waveguide and the width of the slot impact the position of

peaks. Also, fabrication process and future work of these two biosensors are presented in this chapter.

Chapter 5

A metamaterial/liquid-core waveguide microfluidic optical biosensor

5.1 introduction

Optical sensors use the characteristics of light propagation to perform sensing and are good alternatives to conventional non-optical devices [253, 254, 255, 256]. A RI scheme based optical biosensor is one of the most powerful optical sensors. Designing the sensor to test the refractive index liquid experimentally can show the potential to measure chemical and biological analytes.

A liquid-core waveguide, which integrates microfluidics with waveguides, can be used in many applications such as sensors [256], optical particle manipulation [257], and nonlinear optics [258]. Commonly for a waveguide, the evanescent wave caused by total internal reflection propagates into the cladding around the core and decays exponentially [259]. In a liquid-core waveguide, the RI change of the core influences the interaction between the optical wave and the cladding, resulting in different guiding properties. Therefore, from a design perspective, the RI of the cladding should be lower than the liquid in the core so as to allow the light to propagate long distances in the waveguide. The liquid in the core allowing for stronger interaction results in high sensitivity of the sensor at the same time [260, 261, 262]. Teflon AF and PDMS have been used to implement liquid core waveguides due to their low refractive indices [263, 264]. As another example, ARROW are designed by coating dielectric multilayer films as the cladding on silicon substrate to introduce the light into the liquid by the high reflectance of core sidewall [265]. There are several sensors based on liquid-core waveguides that have been previously realized. Examples include a liquid-core waveguide sensor based on ring resonator introduced by Testa et al [266]. With the hybrid claddings composed by bonding PDMS layer on antiresonant layers to produce high reflectance to

confine the light, such sensor can achieve the sensitivity of 700 nm/RIU, which is higher than the sensitivity of conventional ring resonator sensors. Another liquid-core waveguide sensor based on MZI using silica as the cladding material can achieve a resolution better than 4×10^{-6} in RI [110]. The proposed liquid-core waveguide sensor integrates PDMS and glass claddings which have low RI and are easily fabricated. Compared with the optofluidic ring resonator sensors [266], the proposed work obtains higher sensitivity as detailed below.

Metamaterials are electromagnetic materials inaccessible in nature that exhibit exotic physical properties and are promising for practical applications [267, 268]. When the scale of a metamaterial element is much smaller than the wavelength of the incident wave, the metamaterial acts as an absorber in which the light interacts with the small features of the metamaterial to affect wave propagation. The deposition of metal gratings on a dielectric material has been shown to create a metamaterial absorber which can act as an optical sensor [269, 270]. The resonance peak produced by such an absorber is not only obtained by surface plasmon resonance with the TM polarization light [271], but also by TE polarized light [272]. Compared with that in conventional metamaterial optical sensors like SPR sensors, in metamaterial/liquid-core waveguide sensors, the confined light can propagate in the target analyte thus enhancing the sensitivity by increasing the light-analyte interaction and by utilizing the direct interaction of the light mode propagating in the waveguide [265]. Also, SPR sensors are excited on the metal-dielectric interface by a transverse magnetic (TM) mode wave and use the resulting intensity modulation to show the performance of the sensor [273], while the proposed approach employs a TE mode to excite the resonance and detect the analyte by measuring the wavelength shift through the change of RI with higher sensitivity and higher quality factor.

This chapter details the design, simulation and testing of an optical biosensor based on a liquid-core waveguide and dielectric/metal metamaterial, which is able to detect liquids with different refractive indices by integrating the techniques mentioned above. With the help of a patterned gold structure, the PDMS and glass are bonded as the cladding of the waveguide.

The light in the liquid core fully interacts with the liquid to achieve high sensitivity of the sensor. The chapter is organized as follows: Section 5.2 describes the configuration and modeling of a basic liquid-core waveguide with embedded metamaterial, Section 5.3 discusses the simulation results, Section 5.4 details the sensor structure and fabrication process, Section 5.5 provides the experimental design and test results of the fabricated sensors along with analysis and discussion.

5.2 Configuration and Modeling

As the basic structure of this design, gold is deposited and patterned as a periodic structure on a glass wafer to form the metamaterial. The glass wafer is then bonded with PDMS to form the channel. A basic liquid-core waveguide sensor consisting of a liquid core, PDMS cladding, glass cladding, and patterned gold, is shown in Figure 5.1. The liquid core (red) has a larger RI than the glass (green) and the PDMS (blue) to make the light propagate in the core due to total internal reflection. In this specific structure design, the height of the core h is 6.2 μm, the period of the gold pattern (yellow) d is 1 μm, and the fill factor is 50%. The light is illuminated at the left side of the waveguide and the transmitted power is detected at the right side. A shift of resonance peak is expected to be measured in the detected spectrum when the RI of the liquid core varies, which is explained as below.

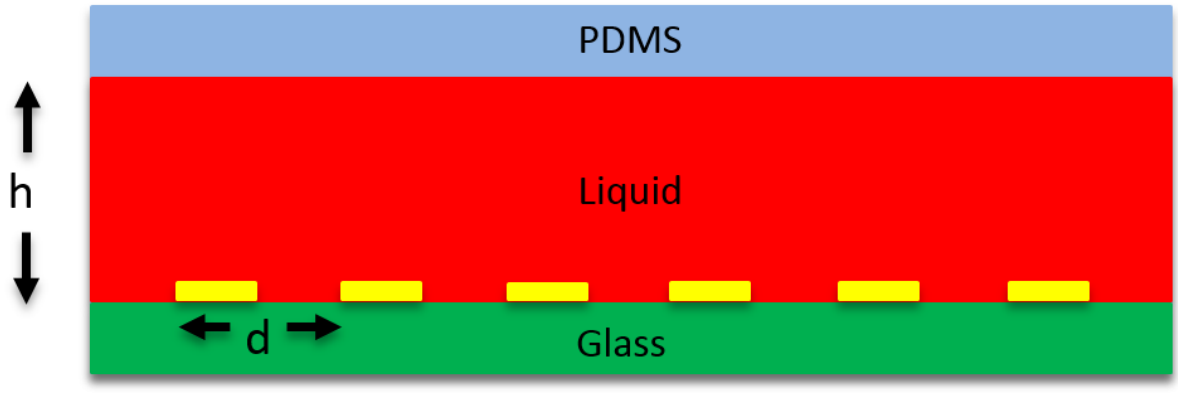

Figure 5.1: The basic structure of a liquid-core waveguide sensor based on gold/dielectric metamaterial.

In a linear isotropic homogeneous lossy medium, the general electromagnetic wave equation can be written as Eq. (5.1), where γ, which is the propagation constant, can be described by Eq. (5.2) and Eq. (5.3).

$$\nabla^2 \vec{E_s} - \gamma^2 \vec{E_s} = 0 \tag{5.1}$$

$$\gamma^2 = j\omega\mu(\eta + j\omega\epsilon) \tag{5.2}$$

$$\gamma = \alpha + j\beta \tag{5.3}$$

where μ is permeability, η is conductivity, ϵ is permittivity, ω is angular frequency, α is the attenuation constant, β is the phase constant, and γ is the propagation constant of the medium. As indicated by Eq. (5.3), the propagation constant is determined by the attenuation constant α and the phase constant β. For this specific design, α and β are related to the RI of the liquid core and the metamaterial structure. The gold pattern, which forms the metamaterial, is a binary grating which consists of periodic rectangular ridges. In our design, gold, which has a very small real RI and high absorption, is patterned on the glass substrate within the waveguide to impact the wave propagation. In such a structure, resonant waves can be coupled in the waveguide with less absorption when phase matching takes place [274]. As a result, with the gold structure placed on the core's inner surface, the light confined in the core interacts with the liquid and the metamaterial at the same time to produce the resonance peak, which can be detected in the output spectrum.

The behavior of light in the device can also be described through classic diffraction theory by Eq. (5.4),

$$\beta = \frac{2\pi}{\lambda} sin\theta + m\frac{2\pi}{d}, m = 1, 2.. \tag{5.4}$$

where β is the phase constant, λ is the wavelength of the incident wave, θ is the propagation angle of the excited wave, and d is period of the patterned gold structure. The phase constant

β, which is related to the amplitude and phase of the light and is influenced by the RI, can determine the behavior of the light propagating in the waveguide. According to Eq. (3.4), a slight change in the propagation constant results in a different coupling and absorption efficiency by affecting the propagation of the excited wave in the waveguide. This, in turn, causes the peak shift in the spectrum.

5.3 Simulation

COMSOL^{TM} Multiphysics software, based on finite element analysis, is an interactive environment for modeling and simulation of scientific and engineering problems. The COMSOL^{TM} Multiphysics Wave Optics module was used to simulate the liquid-core waveguide sensor with the help of boundary mode analysis. A parametric sweep was used to excite different wavelengths of the incident light and perfect matched layer boundary conditions were used to remove the reflection from the boundary. A boundary mode analysis was performed to solve for the propagation constant. The electric field and the propagation constant in COMSOL simulation also can be obtained by the previously mentioned Eq. (3.6), Eq. (3.7) and Eq. (3.8).

As for the simulation parameters, the liquid in the core was defined by setting its RI while observing the simulation results. The refractive indices of the PDMS and the glass were set as 1.4 and 1.45, respectively. The RI of gold was set with real part of n = 0.49 and imaginary part of i = 10.35. The gold pattern was based on a periodic rectangular grating structure which had parameters of 80 nm for height, 50% for fill factor, and 1 μm for the grating period. A parametric sweep was used to excite different wavelengths of the incident light. Perfectly matched layers were used to reduce the reflection from the boundary. A boundary mode analysis was performed to solve for the propagation constant. Wavelengths ranging from 1450 nm to 1650 nm were simulated.

During simulation, the light was confined in the core and interacted with the gold/dielectric metamaterial structure. TE mode light and TM mode light were both illuminated at the

input port. For the TE mode, Figure 5.2a and Figure 5.2b show the input and output parts of the electric field when the light resonated with the metamaterial structure, respectively, while Figure 5.2c and Figure 5.2d present input and output parts of the light significantly filtered by the metamaterial structure when the waveguide was 4 mm in length, core height was 6.2 μm and with a metamaterial of 4000 periods inside. To gain better insight into the sensor performance, a waveguide with a metamaterial with 1000 periods (1-mm long) and a waveguide with a metamaterial with 4000 periods (4-mm long) were simulated respectively. The core RI was set to 1.61 for both designs, and the simulation was performed to analyze the light transmission in the liquid core depending on the number of metamaterial periods. Since the refractive indices of the glass and PDMS are 1.45 and 1.4, respectively, the RI of the analyte needed to be higher than 1.45 to realize total internal reflection. To prove the concept, liquids with RI around 1.6 which were readily available and have good contrast, were used as target analytes in both the simulations and the experiments. As plotted in Figure 5.3, within a wavelength range of 200 nm seven narrow peaks appear in the spectrum of both waveguides. As expected, the waveguide with 4000 grating periods (blue) exhibited sharper and higher signal to noise ratio (SNR) than the waveguide with 1000 grating periods(orange), while the peaks of both waveguides were not shifted in wavelength. For the TM mode as shown in Figure 5.4 , however, the maximum transmission of the peaks in the range of 200 nm is less than 2%. Since its intensity is negligible compared with the TE mode, the influence of the TM mode light on the total transmission is neglected in the rest of this chapter.

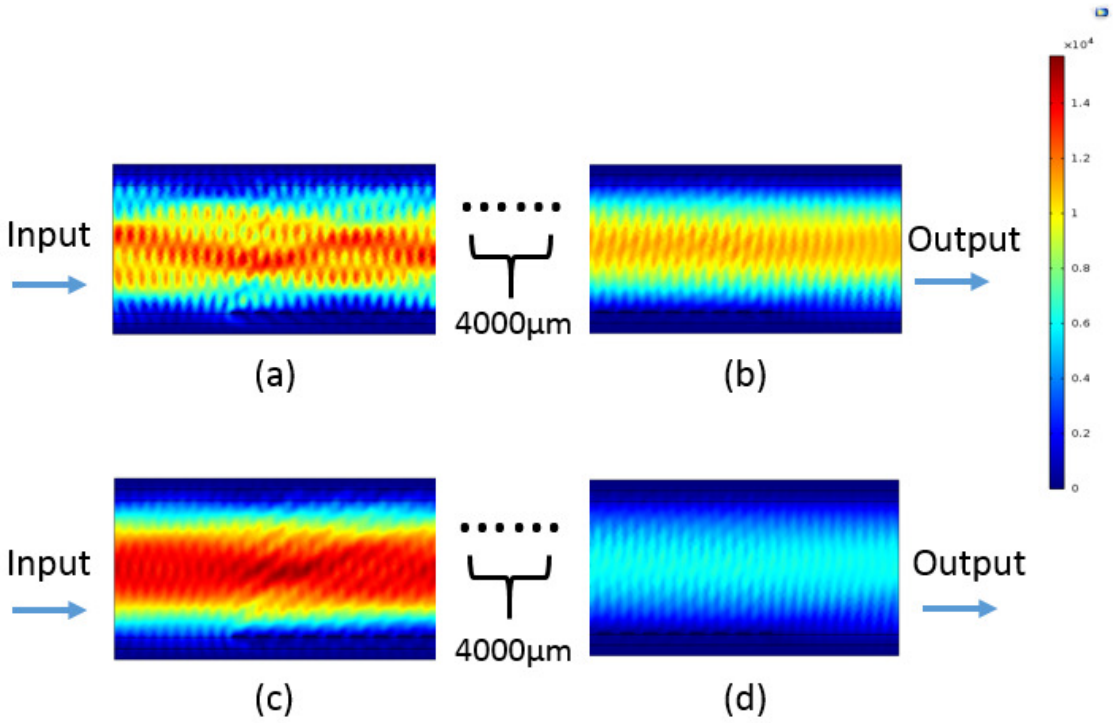

Figure 5.2: (a) Input part of electrical field when the light resonates with the metamaterial in the waveguide. (b) Output part of electrical field when the light resonates with the metamaterial in the waveguide. (c) Input part of electrical field when the light is significantly filtered by the metamaterial in the waveguide. (d) Output part of electrical field when the light is significantly filtered by the metamaterial in the waveguide.

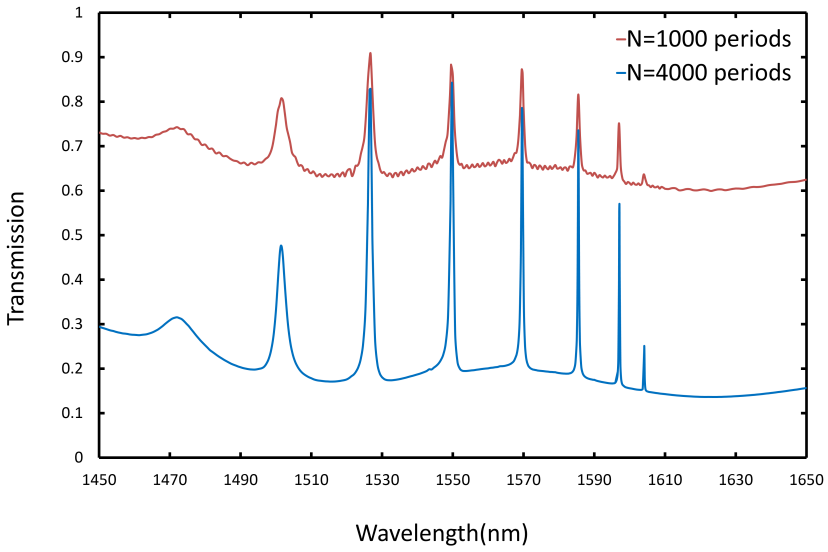

Figure 5.3: The output spectra of one waveguide consisting of a metamaterial structure with 4000 periods and one consisting of a structure of 1000 periods.

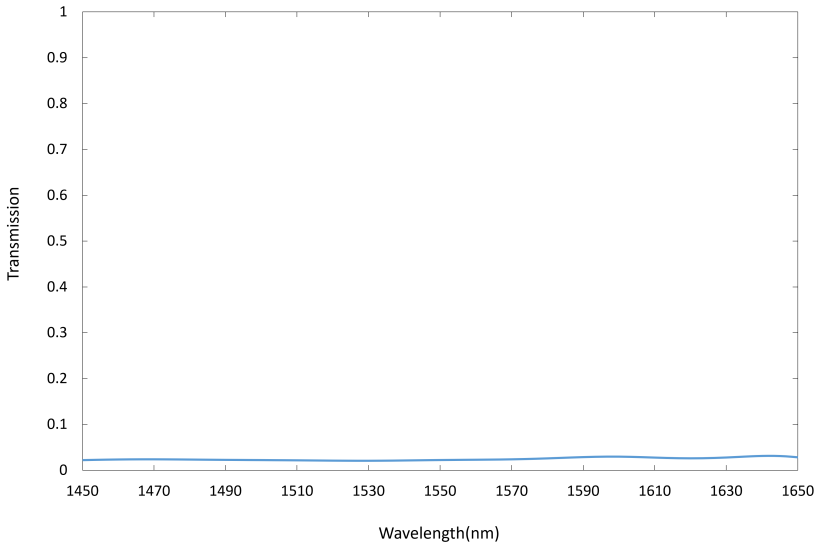

Figure 5.4: The output spectrum for TM wave when 6.2 μm are used as the core thickness of the waveguide consisting of a metamaterial structure of 1000 periods.

The influence of RI was also analyzed by varying the RI over the range from 1.605 to 1.615. The peaks red shifted when the RI increased, as shown in Figure 5.5. The simulated sensitivity of the sensor was close to 1000 nm/RIU and the quality factor was 1703. Another parameter of significance is the core height h. As shown in Figure 5.6, although more peaks existed in the output spectrum of the 10-μm-high waveguide (orange), the light had stronger resonance in the 6.2-μm-high waveguide (blue), indicating the latter to be a better candidate for fabrication. Based on the simulations studying the influence of the number of metamaterial periods, RI, and height of the core, a 6.2-μm-high waveguide consisting of a structure of 4000 periods was selected for fabrication to gain high intensity contrast and high sensitivity.

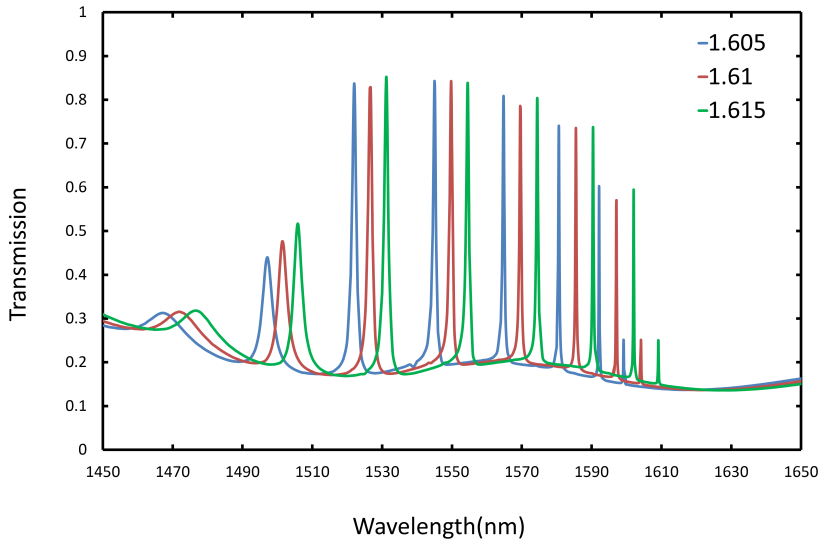

Figure 5.5: The output spectra when the core RI = 1.605, 1.610 and 1.615 of the waveguide consisting of a metamaterial structure of 4000 periods.

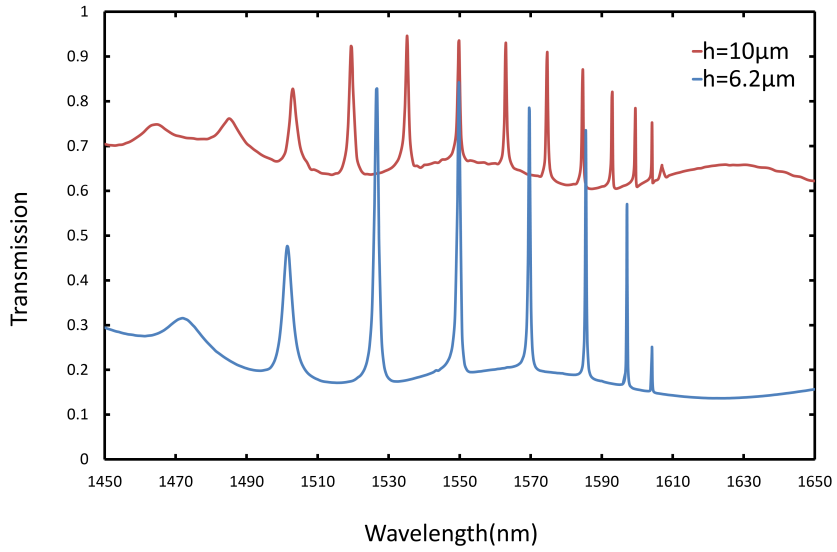

Figure 5.6: The output spectra when 6.2 μm and 10 μm are used as the core thickness of the waveguide consisting of a metamaterial structure of 4000 periods.

5.4 Fabrication

5.4.1 Lift-off Process for the gold/dielectric metamaterial

A 100 mm glass wafer was prepared by performing a standard Radio Corporation of America (RCA) clean, which is a solution comprised of 5 parts of deionized water, 1 part of ammonia water (29% by weight of NH_3) and 1 part of aqueous H_2O_2 (hydrogen peroxide, 30%). The mixed solution was heated to temperature of 70°C with a hot plate and then the wafer was dipped into the solution for 20 minutes. After cleaning the wafer was rinsed in deionized (DI) water and then dried with nitrogen.

The gold pattern was fabricated through a lift-off process as shown in Figure 5.7. Figure 5.7a shows the cross-section view of the 1 cm $\times$ 1 cm square glass wafer which was used as a substrate was obtained by dicing the 100 mm glass wafer into pieces. As shown in Figure 5.7b, a 10 nm chromium thin film (black) was deposited on the glass wafer by e-beam evaporation to avoid charging during the exposure. 950 PMMA A4 by MicroChem^{TM} was used as the e-beam resist (red) in the process (Figure 5.7c). The PMMA was spun at 2500 rpm for 60 s. The thickness after baking at 180 °C for 1 min and 30 s was measured to be 260 nm. A metamaterial of 4000 periods with period of 1 μm were patterned, as shown in Figure 5.7c. After the development of the resist, as shown in Figure 5.7d, a 10 nm titanium film (green) and an 80 nm gold film (yellow) were deposited by e-beam evaporation, respectively. The 10 nm titanium film worked as an adhesion layer between the chromium film and the gold film. This was necessary due to the fact that the chromium film was easily oxidized during previous fabrication steps and oxidation decreases the adhesion between chromium and gold. Depositing the gold film immediately after the titanium film without breaking the vacuum can prevent the oxidation of titanium to ensure the adhesion between gold and titanium. The titanium film also provides strong adhesion with chromium or oxidized chromium. The wafer was then immersed into acetone in an ultrasonic bath to complete the lift-off process which produced the gold structure on the surface of the wafer (Figure 5.7e).

The total thickness of metal was close to one third of the thickness of the photoresist to avoid the metal covering the photoresist layer [275]. The gold pattern was left on the substrate after acetone cleaning as shown in Figure 5.7e, and the remaining 10 nm chromium film was removed by chromium etchant through wet etching as shown in Figure 5.7f.

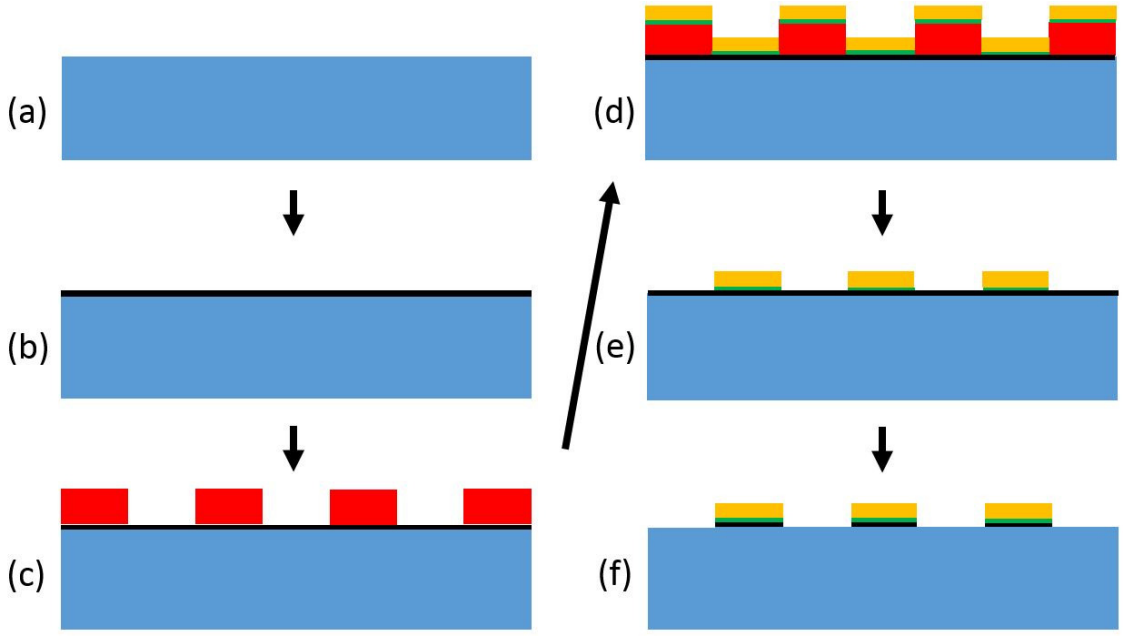

Figure 5.7: Lift-off process: (a) A glass wafer (blue) is prepared. (b) 10-nm chromium (black) is deposited on the glass wafer. (c) PMMA (red) is patterned on the chromium by e-beam lithography. (d) A 10-nm titanium film (green) and an 80-nm gold film (yellow) are deposited. (e) gold patterns are obtained after acetone cleaning. (f) chromium film is removed by chromium etchant.

5.4.2 Design and Assembly for the Liquid-core Waveguide

In order to build the microfluidic liquid-core waveguide sensor, the gold structure was covered by PDMS channels [276]. The PDMS was prepared by using a Sylgard 184 Silicone Elastomer kit by Dow Corning^{TM}. To prepare the silicon mold, a 100 mm silicon wafer is cleaned by RCA cleaning, with solution 5 parts of deionized water, 1 part of ammonia water (29% by weight of NH_3) and 1 part of aqueous H_2O_2 (hydrogen peroxide, 30%), then AZ 9245 photoresist was spun at 2200 rpm for 25 s on the wafer to produce a 6.2-μm-thick pattern, As shown in Figure 5.8a, the silicon wafer is prepared by RCA cleaning. Then the resist 9245

was patterned by UV lithography, as shown in Figure 5.8b. After using trimethylchlorosilane (TMCS) to silanize the surface of the silicon wafer, a 10:1 mixture of PDMS base and curing agent was poured onto the mold, as shown in the Figure 5.8c. The wafer was placed in an oven to cure at 80 °C for 3 h and the PDMS sample was obtained by peeling the PDMS from the silicon mold, as shown in Figure 5.8d. The microfluidic channel was designed with a T shape and the hole at the bottom of the T shape was used as the inlet for the channels [277], as shown in Figure 5.9c. Liquid of different refractive indices can be injected into this hole to fill the channel. Five channels (Figure 5.9d) with 1 cm in length (Figure 5.9c), 40 μm in width and 6.2 μm in height were separated by 20 μm width each (Figure 5.9b and Figure 5.9a). A reservoir was formed around the channels within an area of 5 mm $\times$ 400 μm in the central part (Figure 5.9c). Five channels were used instead of a single channel to help with optical alignment as discussed below. The ratio of channel width to height was set less than 10:1 to prevent the channel from collapsing. For the same purpose, four rows of rectangular pillars were also placed around the channels. Since the diameter of the core of the single mode fiber used in the experiments was only 8.5 μm, the total width of the five channels of 300 μm made it easier to align the fiber tip with the sensor input. The reservoir around the channel was designed to balance the liquid and avoid leakage from the gap of gold structure. Also, as the time for the liquid to fill the reservoir was much slower than to fill the channels, the filling of the reservoir can be used as an indicator to observe whether the sensor is fully filled with the analyte.

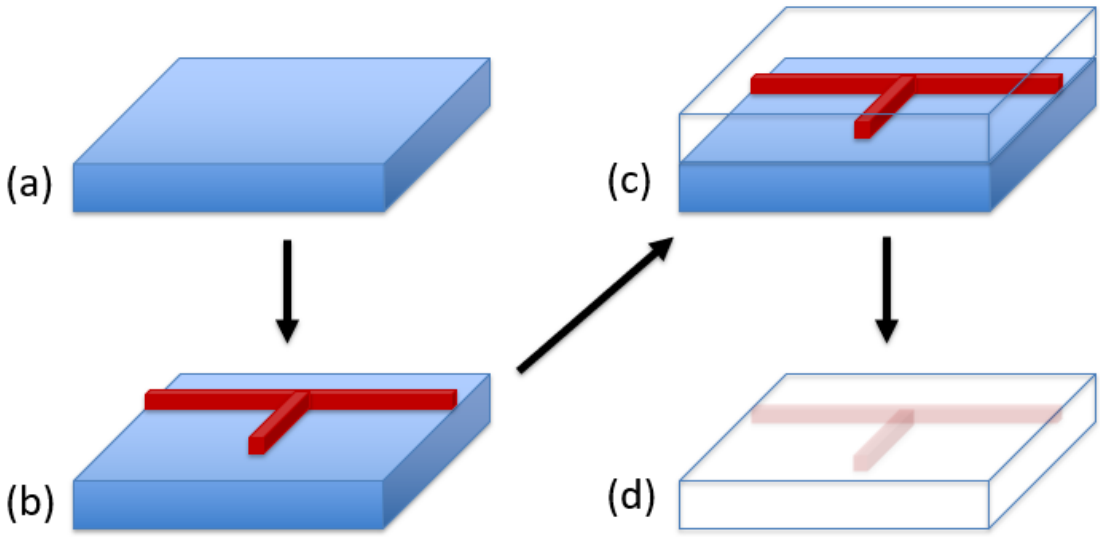

Figure 5.8: (a) a silicon wafer is prepared. (b) Resist 9245 is patterned by UV lithography. (c) a 10:1 mixture of PDMS base and curing agent is poured onto the mold. (d) The PDMS sample is obtained by peeled the PDMS from silicon mold.

The 1 cm × 1 cm PDMS samples were obtained by dicing the PDMS replica into pieces after PDMS replica was peeled away from the silicon mold. The microfluidic T channel was then punched with a Luer stub to allow filling of the channel and reservoir. The PDMS sample (Figure 5.9c) and the glass sample (Figure 5.9e) were temporarily bonded in a way that the core channels were cover by the metamaterial (Figure 5.9g to Figure 5.9h). Before bonding, both the glass and the PDMS samples were treated by ethanol and blown dry. After alignment under a microscope, the assembly was moved to the oven to bake at 80 °C for 3 hours for bonding. The bonded sensor is shown in Figure 5.10, in which three of the five channels were covered by the metamaterial and the angle between the structure and the channel was within 1°.

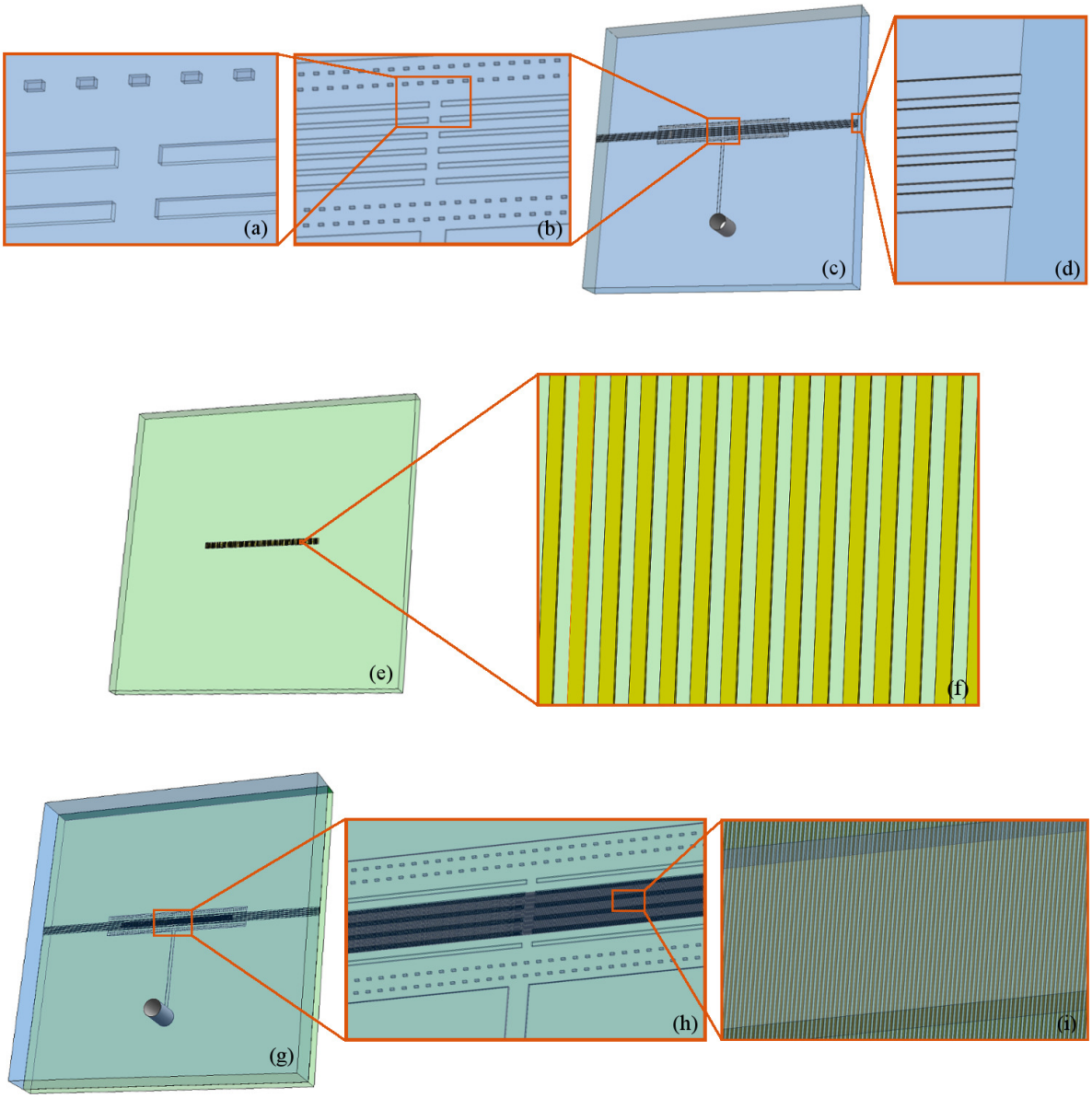

Figure 5.9: 3D structures of the sensor: (a)(b) Zoomed-in figures of the channels and the reservoir with rectangular pillars to prevent collapsing. (c) Five channels formed on PDMS. (d) A zoomed-in on the output side of the channels. (e) gold structure deposited on a glass wafer. (f) A zoomed-in figure of the gold/dielectric metamaterial. (g) The assembly of the sensor. (h)(i) Zoomed-in figures of the channels under gold gratings.

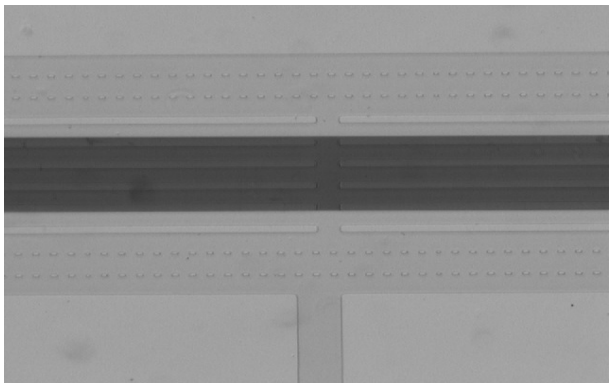

Figure 5.10: A photograph of the central part of the bonded sensor imaged by microscope Nikon^{TM} SMZ800N.

With one single mode optical fiber deployed at the input, a single channel was aligned to the fiber and received the light from it for each experiment. Since the three channels covered by the metamaterial in each sample were fabricated in the same process, they were assumed to be identical. Therefore, the alignment became easier by increasing the chances of matching the fiber and the channel. Also, when the fiber is aligned with either of the two channels without the metamaterial structure, the intensity of the output light will significantly increase, which can be used to ensure proper alignment of the single mode fiber to a channel with the metamaterial present.

Another issue came from the fact that the light not only propagates in the core of the sensor, but also has good transmission in the glass and PDMS substrates. To solve this problem, two sidewalls of the sensor facing to the fibers (i.e. the input and the output sides) were coated with Ti without covering the channel by a radio frequency / direct current (RF/DC) sputtering system, and only the DC sputtering is used due to metal deposition.

The DC sputtering system based on the microwave plasma discharge principle consists of a magnetron sputtering of two inch diameter with the substrate holder mounted over the plasma (ion) gun as an ion source without a filament. The figure of the sputtering chamber is shown as as shown as Figure 5.11. The 2.0"Dia. $\times$ 0.125" thick Ti target, supplied by the Kurt J. Lesker Company, was used to deposit the film on the surface of the substrate. The sample was held in place by a small 3D printed box with one sidewall of the sample exposed

to the air. The box was then adhered on a wafer to serve as the substrate. The target and exposed sidewall distance was optimized and kept constant at 14 cm. The sputtering chamber was pumped down to 5×10^{-6} with a turbo mechanical pump initially and Ar was introduced, and the schematic of the sputtering chamber was shown as Figure 5.12. Then the chamber pressure was continuously pumped down to 7 mTorr. The power was set to 100 W to start the sputtering process and 60 nm Ti film was deposited in 60 mins. The position of the sample was adjusted in the small box to allow the other sidewall to be coated with 60 nm Ti. The Figure 5.13 shows the small box and Figure 5.14 shows the sample sidewalls coated with Ti.

Figure 5.11: Image of the sputtering chamber.

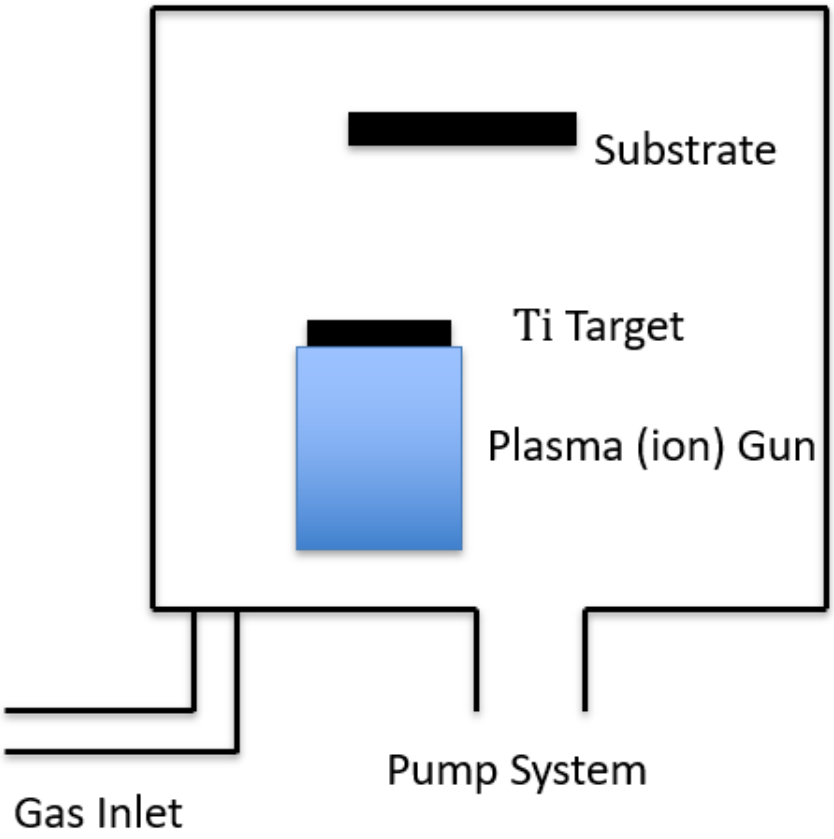

Figure 5.12: Schematic of the sputtering chamber.

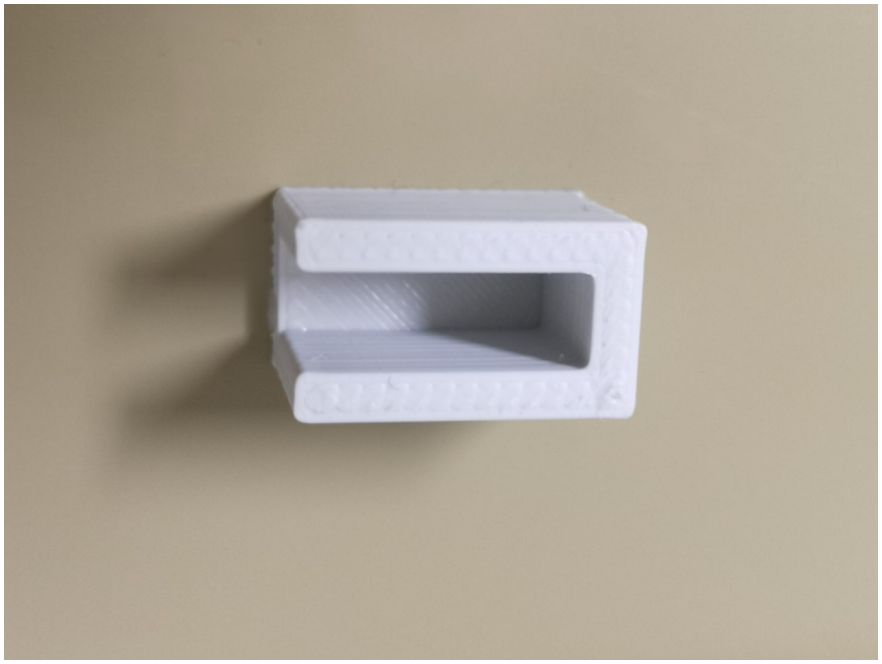

Figure 5.13: The box to hold the sample made by 3D printer.

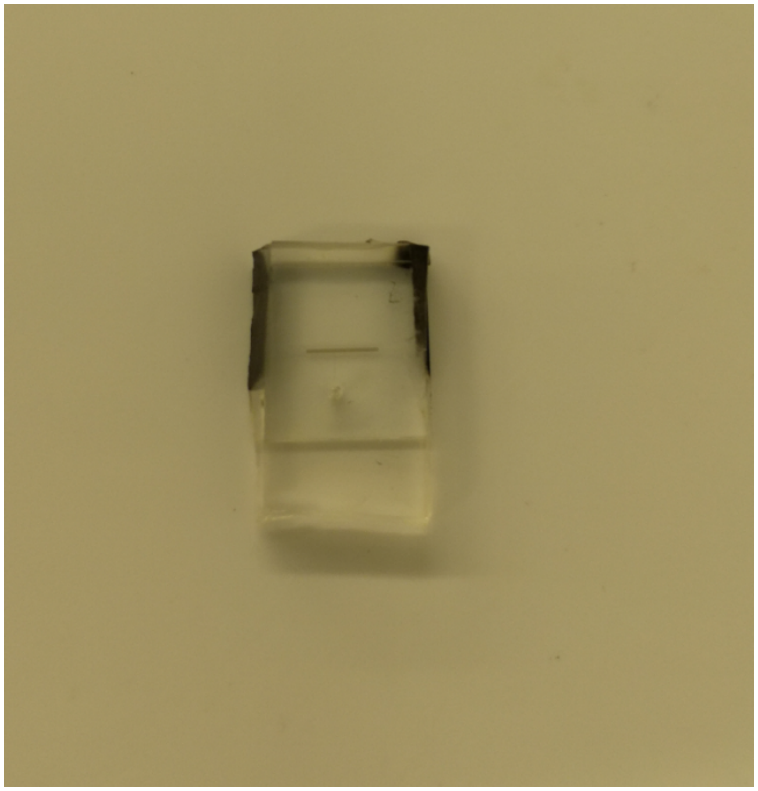

Figure 5.14: The sample deposited with 120 nm Ti film by sputtering system.

The thickness of Ti on each side of the sensor was 60 nm. The Ti coating with a total thickness of 120 nm reduced the power by more than 10000 times to prevent light propagation in the substrate while allowing it within the channel. As a result, when the fiber was aligned to one of the five channels, the power received at the output was greatly increased, and when aligned to one of the three channels with the metamaterial structure, a resonance peak was obtained.

5.5 Testing and Results

As preparation for the tests, liquid was injected into the microchannel via a syringe. The liquid was able to fill the microchannel in less than 1 min after the injection through the hole (Figure 5.9g). When more liquid than necessary was injected, the excess liquid was kept in the hole which acted as a reservoir to avoid the influence of liquid evaporation from

the PDMS channels during experiment. Liquids with refractive indices of 1.605, 1.608 and 1.613 were tested during the experiment.

5.5.1 Verification of Function

With liquid injected into the channel, the sensor was placed in the test apparatus, as shown in Figure 5.15. A single mode optical fiber and a multi-mode optical fiber were placed on a 3-axis stage (by Thorlabs^{TM}) which allowed for accurate positioning of the fibers. The single-mode fiber (with core diameter of 8.5 μm) connected the sensor input to a tunable laser (IQTLS by Coherent Solutions). The multi-mode fiber (with core diameter of 105 μm) was connected to the sensor output and transmitted the signal to a spectrum analyzer (AQ6370D by Yokogawa).

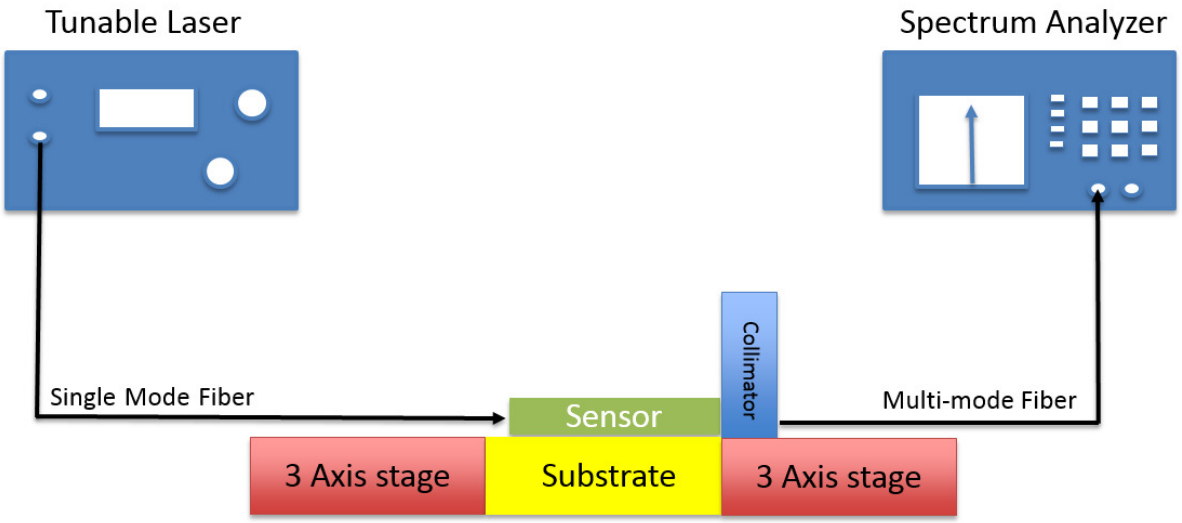

Figure 5.15: Optical setup for testing the sensor.

The IQTLS is a continuous wave laser source with the range from 1527.6 nm to 1567.2 nm, as shown as Figure 5.16. Its specifications include high-power output of maximum power 15 dBm, narrow 100 kHz linewidth and 0.01 pm resolution tunability. This tunable laser source can be controlled via USB or Ethernet ports with single or dual laser configurations. Also it can be used for applications including coherent / Orthogonal Frequency Division Multiplexing transmission and Wavelength Division Multiplexing network emulation. The

spectrum analyzer accepts a wavelength range from 600 nm to 1700 nm ideally for the characterization and test of optical components and systems in the tele-communications Industry, as shown as Figure 5.17. The unique free space input design allows testing of both dense wavelength-division multiplexing class single-mode and Vertical Cavity Surface Emitting Lasers sourced multi-mode fibers in one single model.

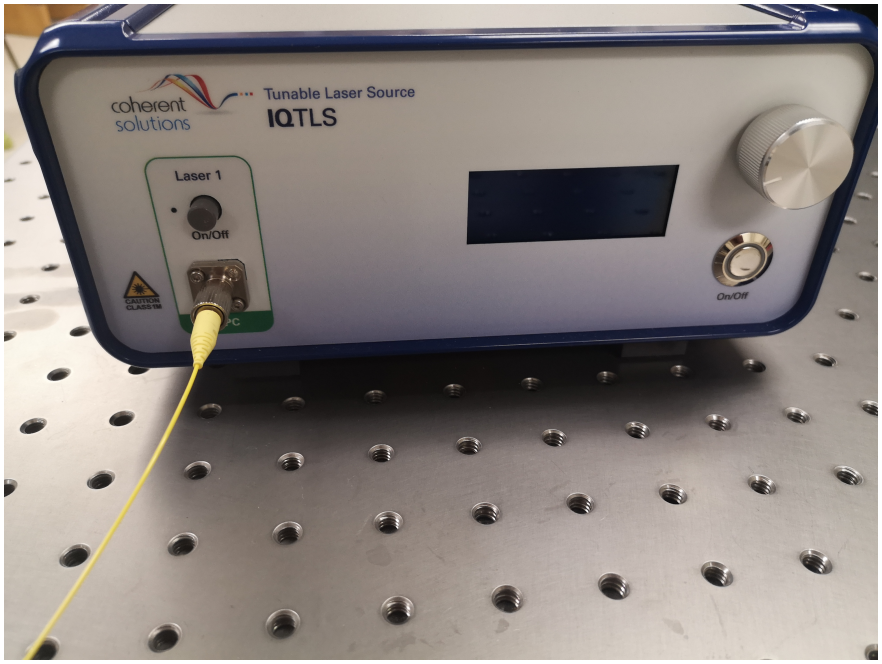

Figure 5.16: The image of the tunable laser (IQTLS by Coherent Solutions) used in the experiment.

Figure 5.17: The spectrum analyzer (AQ6370D by Yokogawa) used in the experiment.

A collimator was mounted on a 2-axis stage in front of the multi-mode fiber for alignment. Figure 5.18 shows an image of the stage and the substrate. With the apparatus set up and alignment done, the sensor was illuminated by the tunable laser over a range from 1527.6 nm to 1567.2 nm. The light output from the channel was collected by the spectrum analyzer. Sensor 1 and Sensor 2 were used for the measurement of all three of the refractive indices respectively. In the results plotted in Figure 5.19, there were three main resonance peaks in the spectrum within the 25-nm range, with each resonance peak corresponding to a different RI. The increase of the RI resulted in the peak red shifted for both Sensor 1 and Sensor 2, as shown in Figure 5.19 and Figure 5.20 respectively. Specifically, for Sensor 1, the peak shift is clearly seen and the resonance wavelengths corresponding to refractive indices of 1.605, 1.608 and 1.613 were 1539.2 nm, 1548.6 nm, and 1554.9 nm respectively. Also, for Sensor 2, the peaks red shifted as Sensor 1 did and the corresponding wavelengths were 1540.7 nm, 1547.8 nm, and 1554.2 nm.

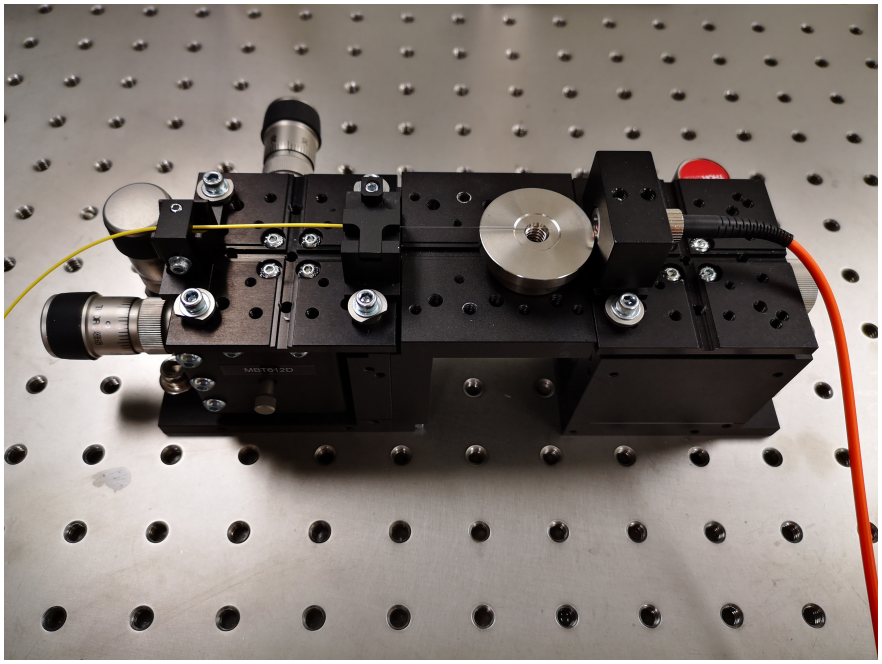

Figure 5.18: A photograph of the substrate of the optical setup mounted on a self-leveled stage.

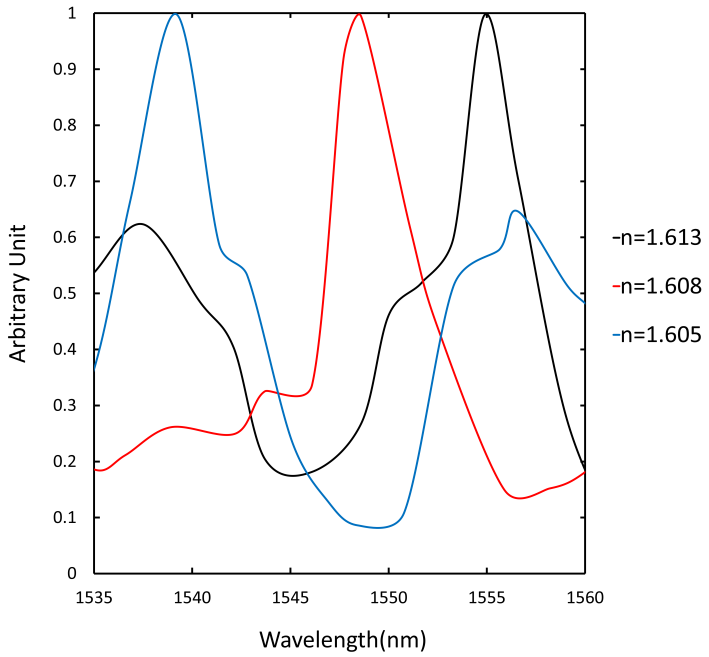

Figure 5.19: The output spectra when analytes with RI = 1.605, RI = 1.608 and RI = 1.613 are tested on Sensor 1.

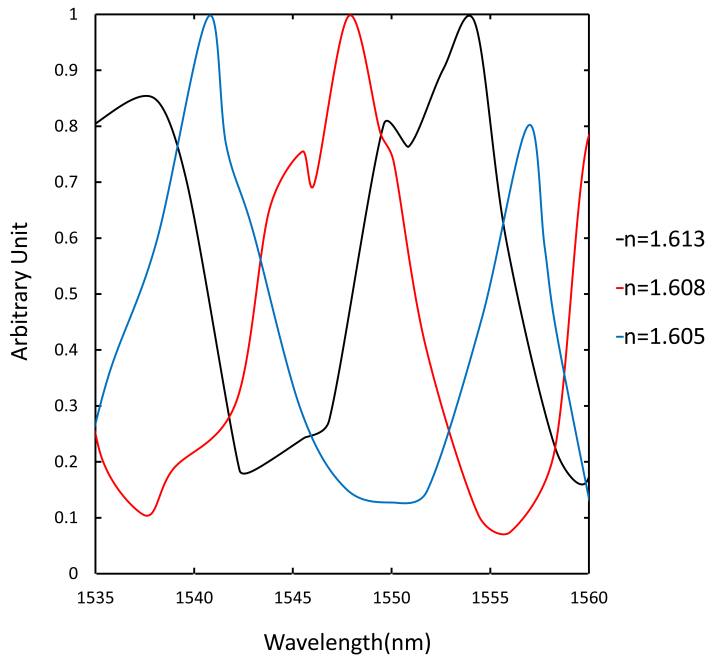

Figure 5.20: The output spectra when analytes with RI = 1.605, RI = 1.608 and RI = 1.613 are tested on Sensor 2.

5.5.2 Study of Repeatability

More sensors were tested to study the tolerance of the fabrication process and verify the repeatability of the sensors. Sensor 3 and Sensor 4 were tested with analytes with RI = 1.605, Sensor 5 and Sensor 6 with RI = 1.608, and Sensor 7 and Sensor 8 with RI = 1.613. The testing results from these samples along with the previous results of Sensor 1 and Sensor 2 were analyzed to study the accuracy of the sensors. Four sets of results from the measurements with RI = 1.605 were plotted in Figure 5.21 for comparison. The position differences between the four peaks were smaller than 5 nm and the average resonance wavelength was 1541.2 nm. Figure 5.22 shows the four results for RI = 1.608 and Figure 5.23 shows the four results for RI = 1.613. The position differences of resonance peaks for RI = 1.608 were less than 2 nm, and less than 5 nm for RI = 1.613, and the average resonance wavelengths were 1547.9 nm and 1554.3 nm, respectively. Looking into these results, all resonance wavelengths corresponding to the peaks for RI = 1.605 were obviously smaller than

the wavelengths of peaks for RI = 1.608, and all wavelengths of resonance peaks for RI = 1.608 were obviously smaller than the wavelengths for RI = 1.613. In other words, there were no overlaps among the resonance wavelength distributions for the different refractive indices. As expected the quality factors were not as good as the simulations predicted due primarily to fabrication and alignment tolerances. However, the results of the experiments still showed a good repeatability of the design. The results from the experiments and from the simulations are summarized and compared in Table 5.1. The experiments show an average sensitivity of more than 1280 nm/RIU, which was close to the result of the simulations. Compared with simulation results, the sensitivities provided by the experiments were relatively higher. Possible reasons could be the strong light confinement of 3D structures and the roughness of the PDMS surface [278].

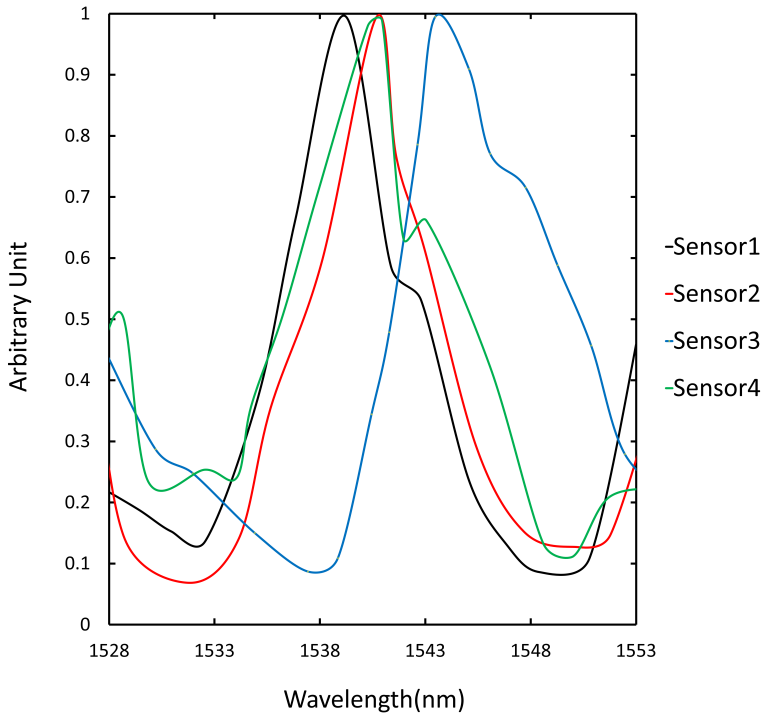

Figure 5.21: The output spectra when the analyte with RI = 1.605 is tested on four sensors.

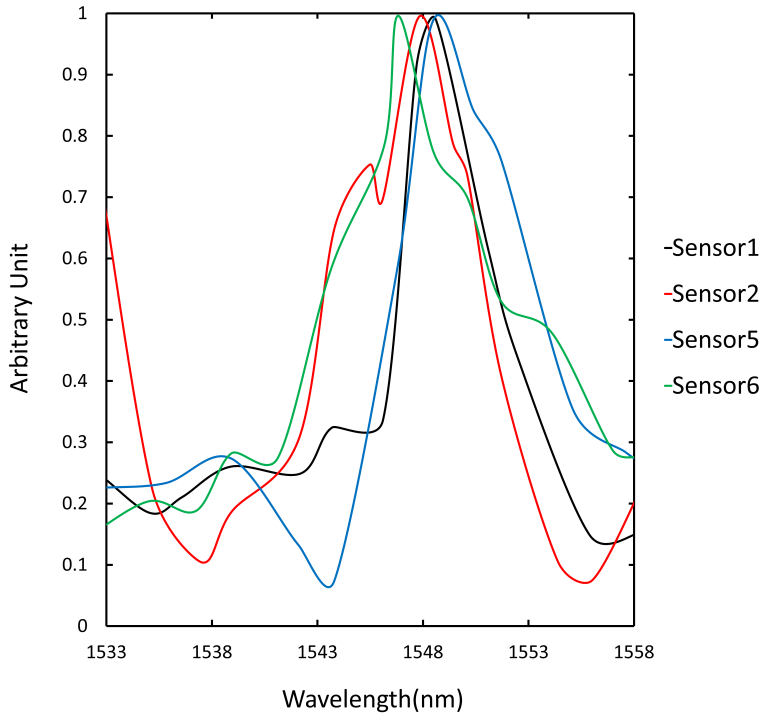

Figure 5.22: The output spectra when the analyte with RI = 1.608 is tested on four sensors.

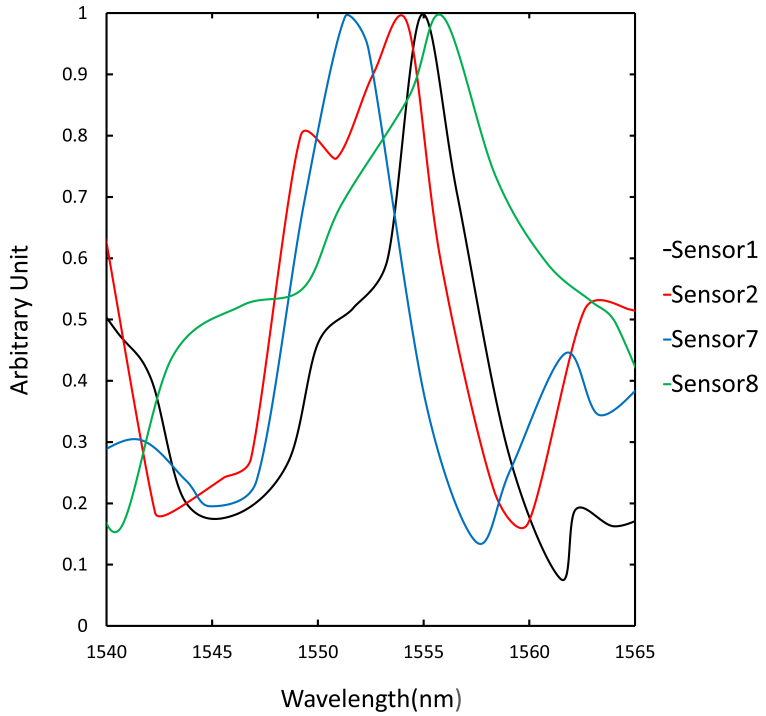

Figure 5.23: The output spectra when the analyte with RI = 1.613 is tested on four sensors.

Table 5.1: Comparison between the experimental (in average of the four sensors for each RI with standard deviations (STD)) and the simulated results.

RI	Experiment			Simulation	
	Resonance λ (nm)	STD (nm)	ΔRIU (nm)	Resonance λ (nm)	ΔRIU (nm)
1.605	1541.2	1.9	0.0	1544.9	0.0
1.608	1547.9	0.7	5.7	1547.8	2.9
1.613	1554.3	1.8	12.1	1552.6	7.7

For the optical loss in the experiments, the output signal could be attenuated due to scattering, fabrication misalignment, channel roughness, gold absorption, liquid absorption, and fiber misalignment. The average loss of the measured devices was 35 dB and the loss varied less than 6 dB among the samples.

5.5.3 Discussion of Results

The experiments verified that resonance peaks exist at the output of the designed biosensor, and that red shifts which increase with RI in the liquid core of the waveguide can be observed. Due to the wave propagation in the liquid being in TE mode during the experiment, the causation of the peaks can exclude the possibility of surface plasmon resonance produced only by TM mode light. These clear peaks and their shifts can be explained by the properties of liquid-core waveguide and metamaterial structure. Since gold has a real RI lower than 1, high imaginary RI, and stable chemical status when exposed to water or air, the metamaterial in the analyte liquid acts similarly to a metal absorber / filter to couple and select certain wavelengths of the light for resonance. In previous researches efforts like [274], output resonance peaks were caused by a coating of dielectric film on the metal gratings absorbing the TE-polarized light [279]. Resonance peak shifts were also found in [280], yet achieved by varying the incidence angle at the input.

In this design, the liquid core can be seen as the thick dielectric film on the patterned gold structure, similar to the solid one in [274]. However, different from the case in [280], the input light is incident normal to the waveguide, instead of with a varying incidence angle. When incident normal to the waveguide, the light will be confined and propagate in the liquid core. The resonance is obtained when the light interacts with the metamaterial of which the grating scale is smaller than resonance wavelength. The parameters of the metamaterial, the thickness and refractive indices of the core and cladding are all relevant to the propagation constant. With the other parameters controlled, varying the RI of the core leads to a change of the guiding properties of the waveguide, resulting in different propagation constants of the light. As indicated in Eq. (5.3) and Eq. (5.4), for a certain wavelength, change of the propagation constant will lead to a different coupling and absorption efficiency of the light. When the light reaches the metamaterial structure, it will be absorbed and coupled back to the core. Some wavelengths will be absorbed more than others instead of coupling. Since the coupling and absorption efficiency of the light will be changed with different propagation constants, different resonance peaks will appear at the output spectrum. The peak position is thus sensitive to the change of RI, while the coupling efficiency is still high within the range of incident laser light, and a high quality factor for the peak remains due to the resonance and absorption.

5.6 Summary

A microfluidic optical biosensor has been presented in this chapter. Fluids with different refractive indices were used for testing and a sensitivity more than 1280 nm/RIU was obtained. As the existence of different molecules in a liquid analyte varies the RI, the presented sensor has a great potential to detect these molecules.

Chapter 6

Conclusion

As a summary, three different kinds of optical biosensors based on gratings and metamaterials are presented and show the function for refractive index sensing.

A MDGCW based biosensor which measures different refractive indices of the binding layer under the waveguide was presented. Simulation results have shown that the MDGCW based biosensor can obtain a sensitivity of 387 nm/RIU and its sensitivity performance was affected by the refractive index of the binding layer, the dimension of the binding layer, and the coupling angle of the incident light. Furthermore, since the effective refractive index of the grating is related to the grating period, the thickness of the grating, and the etch depth of the grating, changes to any of these parameters allow further optimization of the MDGCW based biosensor. Since the binding layer is located on the grating substrate, it will not influence the actual patterned structure of the grating coupler. The biosensor presented allows for an unobstructed light path to the grating, and also provide easy experimental integration. Thus, its straightforward fabrication and its simple experimental set up should allow for numerous chemical and biological sensing applications.

For the second kind of sensors, two optical waveguide biosensors based on Bragg gratings were presented. The DSBGW uses the Bragg gratings on SOI wafer to produce a TM mode resonance, resulting in a peak in the spectrum to measure the liquids of different refractive indices with 255 nm/RIU sensitivity. The DSBGISW with it's dominant TE mode takes advantage of the slot waveguide and gratings to enhance the interaction between the light and liquid analyte thus obtaining better resonance. It can also reduce the length of the waveguide for sensor applications with a sensitivty of 190 nm/RIU. For future fabrication, both sensors can be fabricated by a dry etching process. With the help of the 3D printed

holder, the fiber can easily be aligned with the grating coupler which should allow for easy experimental verifiction. The test liquid range from 1.33 to 1.63 can be applied on the biosensors so that the liquid covers all the area for measurement. Along with the refractive index liquids, other chemical or biological analytes can be applied and measured by these two biosensors. Due to their large test range of refractive indices, most biological fluids and molecules are suitable for the measurement by these two biosensors.

A novel design for a microfluidic optical sensor has been presented in the fifth chapter. The sensor integrates the concepts of liquid-core waveguides and gold/dielectric metamaterials to enhance the light interaction with the analyte, leading to the conversion of the refractive indices of measurands (i.e. liquid analytes) to resonance peak shifts in the output spectrum. The well matched simulation and experimental results have proven high sensitivity and good repeatability for the sensor design. Fluids with different refractive indices were used for testing and a sensitivity more than 1280 nm/RIU was achieved. As the existence of different molecules in a liquid analyte varies the RI, the presented sensor has a great potential to detect these molecules. In future efforts, the sensor will be optimized for quality factor, and applied in medical and industrial areas such as cell and protein detection. Due to the fact that the proposed design works only when the RI of the core is higher than the refractive indices of glass and PDMS, low RI optical polymer substrates will be used to replace the glass substrate and PDMS channel structure of the sensor. Low RI optical polymers will allow measurement of analytes with lower refractive indices such as most biological fluids of interest.

Bibliography

[1] A. Purniawan, G. Pandraud, T. Moh, A. Marthen, K. Vakalopoulos, P. French, and P. Sarro, "Fabrication and optical measurements of a tio2-ald evanescent waveguide sensor," *Sensors and Actuators A: Physical*, vol. 188, pp. 127–132, 2012.

[2] F. Chiavaioli, P. Zubiate, I. Del Villar, C. R. Zamarreño, A. Giannetti, S. Tombelli, C. Trono, F. J. Arregui, I. R. Matias, and F. Baldini, "Femtomolar detection by nanocoated fiber label-free biosensors," *ACS sensors*, vol. 3, no. 5, pp. 936–943, 2018.

[3] P. Berini, "Long-range surface plasmon polaritons," *Advances in optics and photonics*, vol. 1, no. 3, pp. 484–588, 2009.

[4] O. Krupin and P. Berini, "Long-range surface plasmon-polariton waveguide biosensors for human cardiac troponin i detection," *Sensors*, vol. 19, no. 3, p. 631, 2019.

[5] Y.-X. Jiang, B.-H. Liu, X.-S. Zhu, X.-L. Tang, and Y.-W. Shi, "Long-range surface plasmon resonance sensor based on dielectric/silver coated hollow fiber with enhanced figure of merit," *Optics letters*, vol. 40, no. 5, pp. 744–747, 2015.

[6] X. Wang, J. Flueckiger, S. Schmidt, S. Grist, S. T. Fard, J. Kirk, M. Doerfler, K. C. Cheung, D. M. Ratner, and L. Chrostowski, "A silicon photonic biosensor using phase-shifted bragg gratings in slot waveguide," *Journal of biophotonics*, vol. 6, no. 10, pp. 821–828, 2013.

[7] R. Srinivasan, S. Umesh, S. Murali, S. Asokan, and S. Siva Gorthi, "Bare fiber bragg grating immunosensor for real-time detection of escherichia coli bacteria," *Journal of biophotonics*, vol. 10, no. 2, pp. 224–230, 2017.

[8] F. Chiavaioli, P. Biswas, C. Trono, S. Jana, S. Bandyopadhyay, N. Basumallick, A. Giannetti, S. Tombelli, S. Bera, A. Mallick *et al.*, "Sol–gel-based titania–silica thin film overlay for long period fiber grating-based biosensors," *Analytical chemistry*, vol. 87, no. 24, pp. 12 024–12 031, 2015.

[9] D. Yuan, Y. Dong, Y. Liu, and T. Li, "Mach-zehnder interferometer biochemical sensor based on silicon-on-insulator rib waveguide with large cross section," *Sensors*, vol. 15, no. 9, pp. 21 500–21 517, 2015.

[10] A. Psarouli, A. Salapatas, A. Botsialas, P. Petrou, I. Raptis, E. Makarona, G. Jobst, K. Tukkiniemi, M. Sopanen, R. Stoffer *et al.*, "Monolithically integrated broad-band mach-zehnder interferometers for highly sensitive label-free detection of biomolecules through dual polarization optics," *Scientific reports*, vol. 5, p. 17600, 2015.

[11] V. Ahsani, F. Ahmed, M. B. Jun, and C. Bradley, "Tapered fiber-optic mach-zehnder interferometer for ultra-high sensitivity measurement of refractive index," *Sensors*, vol. 19, no. 7, p. 1652, 2019.

[12] X. Li, Y. Shao, Y. Yu, Y. Zhang, and S. Wei, "A highly sensitive fiber-optic fabry–perot interferometer based on internal reflection mirrors for refractive index measurement," *Sensors*, vol. 16, no. 6, p. 794, 2016.

[13] S. John, D. Joannopoulos, J. N. Winn, and R. D. Meade, "Photonic crystals: molding the flow of light," in *Princeton University of press*, 2008.

[14] H. Yan, C.-J. Yang, N. Tang, Y. Zou, S. Chakravarty, A. Roth, and R. T. Chen, "Specific detection of antibiotics by silicon-on-chip photonic crystal biosensor arrays," *IEEE Sensors Journal*, vol. 17, no. 18, pp. 5915–5919, 2017.

[15] Q. Wang and B. Wang, "Sensitivity enhanced spr immunosensor based on graphene oxide and spa co-modified photonic crystal fiber," *Optics & Laser Technology*, vol. 107, pp. 210–215, 2018.

[16] J. Li and K. Nallappan, "Optimization of hollow-core photonic bragg fibers towards practical sensing implementations," *Optical Materials Express*, vol. 9, no. 4, pp. 1640–1653, 2019.

[17] X. Jiang, J. Ye, J. Zou, M. Li, and J.-J. He, "Cascaded silicon-on-insulator double-ring sensors operating in high-sensitivity transverse-magnetic mode," *Optics letters*, vol. 38, no. 8, pp. 1349–1351, 2013.

[18] X. Zhang, L. Ren, X. Wu, H. Li, L. Liu, and L. Xu, "Coupled optofluidic ring laser for ultrahigh- sensitive sensing," *Optics Express*, vol. 19, no. 22, pp. 22 242–22 247, 2011.

[19] P. Azuelos, P. Girault, N. Lorrain, L. Poffo, M. Guendouz, M. Thual, J. Lemaitre, P. Pirasteh, I. Hardy, and J. Charrier, "High sensitivity optical biosensor based on polymer materials and using the vernier effect," *Optics express*, vol. 25, no. 24, pp. 30 799–30 806, 2017.

[20] C.-W. Chang, X. Xu, S. Chakravarty, H.-C. Huang, L.-W. Tu, Q. Y. Chen, H. Dalir, M. A. Krainak, and R. T. Chen, "Pedestal subwavelength grating metamaterial waveguide ring resonator for ultra-sensitive label-free biosensing," *Biosensors and Bioelectronics*, p. 111396, 2019.

[21] Y. Luo, R. Fan, Y. Zhang, Q. Wu, Z. Ren, and B. Peng, "Novel optical fiber refractive sensor fabricated with an alcohol-filled photonic crystal fiber based on a mach–zehnder interferometer," *Optical Fiber Technology*, vol. 48, pp. 278–282, 2019.

[22] J. Tian, Z. Lu, M. Quan, Y. Jiao, and Y. Yao, "Fast response fabry–perot interferometer microfluidic refractive index fiber sensor based on concave-core photonic crystal fiber," *Optics express*, vol. 24, no. 18, pp. 20 132–20 142, 2016.

[23] J. P. Dowling and J. Gea-Banacloche, "Evanescent light-wave atom mirrors, resonators, waveguides, and traps," in *Advances in atomic, molecular, and optical physics*. Elsevier, 1996, vol. 37, pp. 1–94.

[24] A. P. Turner, "Biosensors: sense and sensibility," *Chemical Society Reviews*, vol. 42, no. 8, pp. 3184–3196, 2013.

[25] X. Fan, I. M. White, S. I. Shopova, H. Zhu, J. D. Suter, and Y. Sun, "Sensitive optical biosensors for unlabeled targets: A review," *analytica chimica acta*, vol. 620, no. 1, pp. 8–26, 2008.

[26] D. Dey and T. Goswami, "Optical biosensors: a revolution towards quantum nanoscale electronics device fabrication," *BioMed Research International*, vol. 2011, 2011.

[27] P. Damborskỳ, J. Švitel, and J. Katrlík, "Optical biosensors," *Essays in biochemistry*, vol. 60, no. 1, pp. 91–100, 2016.

[28] R. D. Peterson, W. Chen, B. T. Cunningham, and J. E. Andrade, "Enhanced sandwich immunoassay using antibody-functionalized magnetic iron-oxide nanoparticles for extraction and detection of soluble transferrin receptor on a photonic crystal biosensor," *Biosensors and Bioelectronics*, vol. 74, pp. 815–822, 2015.

[29] S. Geidel, S. P. Llopis, M. Rodrigo, G. de Diego-Castilla, A. Sousa, J. Nestler, T. Otto, T. Gessner, and V. Parro, "Integration of an optical ring resonator biosensor into a self-contained microfluidic cartridge with active, single-shot micropumps," *Micromachines*, vol. 7, no. 9, p. 153, 2016.

[30] Y. Qi, X. Gao, and W. Bi, "Refractive index biosensor based on microstructured optical fiber long-period gratings: a theoretical analysis," *JOSA B*, vol. 30, no. 5, pp. 1256–1260, 2013.

[31] M. Li, Y. Liu, Y. Chen, and J.-J. He, "Silicon-on-insulator nanowire based optical waveguide biosensors," in *Journal of Physics: Conference Series*, vol. 680, no. 1. IOP Publishing, 2016, p. 012004.

[32] N. Nehru, E. U. Donev, G. M. Huda, L. Yu, Y. Wei, and J. T. Hastings, "Differentiating surface and bulk interactions using localized surface plasmon resonances of gold nanorods," *Optics express*, vol. 20, no. 7, pp. 6905–6914, 2012.

[33] K.-L. Lee, C.-C. Chang, M.-L. You, M.-Y. Pan, and P.-K. Wei, "Enhancing the surface sensitivity of metallic nanostructures using oblique-angle-induced fano resonances," *Scientific reports*, vol. 6, p. 33126, 2016.

[34] G. Veldhuis, O. Parriaux, H. Hoekstra, and P. Lambeck, "Sensitivity enhancement in evanescent optical waveguide sensors," *Journal of lightwave technology*, vol. 18, no. 5, p. 677, 2000.

[35] G. d. Cesare, R. Asquini, A. Buzzin, and D. Caputo, "Evanescent waveguide sensor for on-chip biomolecular detection," in *Multidisciplinary Digital Publishing Institute Proceedings*, vol. 1, no. 4, 2017, p. 562.

[36] A. Tortschanoff, C. Ranacher, C. Consani, T. Grille, and M. Moridi, "Optimization of si-based waveguides for evanescent-field sensors," in *Multidisciplinary Digital Publishing Institute Proceedings*, vol. 2, no. 13, 2018, p. 739.

[37] Y. Xin, G. Pandraud, L. Otten, Y. Zhang, and P. French, "Surface functionalization of su-8 vertical waveguide for biomedical sensing: Bacteria diagnosis," *Proceedings*, vol. 2, no. 13, 2018. [Online]. Available: http://www.mdpi.com/2504-3900/2/13/1081

[38] M. Oraie and H. Latifi, "Real-time refractive-index sensing by using liquid core/liquid cladding optofluidic waveguide," *Optics & Laser Technology*, vol. 111, pp. 303–306, 2019.

[39] J. Charrier, M.-L. Brandily, H. Lhermite, K. Michel, B. Bureau, F. Verger, and V. Nazabal, "Evanescent wave optical micro-sensor based on chalcogenide glass," *Sensors and Actuators B: Chemical*, vol. 173, pp. 468–476, 2012.

[40] B. B. Kim, W. J. Im, J. Y. Byun, H. M. Kim, M.-G. Kim, and Y.-B. Shin, "Label-free crp detection using optical biosensor with one-step immobilization of antibody on nitrocellulose membrane," *Sensors and Actuators B: Chemical*, vol. 190, pp. 243–248, 2014.

[41] M. Hiraoui, L. Haji, M. Guendouz, N. Lorrain, A. Moadhen, and M. Oueslati, "Towards a biosensor based on anti resonant reflecting optical waveguide fabricated from porous silicon," *Biosensors and Bioelectronics*, vol. 36, no. 1, pp. 212–216, 2012.

[42] J. H. Sim, Y. H. Kwak, C. H. Choi, S.-H. Paek, S. S. Park, and S. Seo, "A birefringent waveguide biosensor platform for label-free live cell detection of listeria monocytogenes," *Sensors and Actuators B: Chemical*, vol. 173, pp. 752–759, 2012.

[43] Y. Liu, S. Chen, Q. Liu, and W. Peng, "Micro-capillary-based evanescent field biosensor for sensitive, label-free dna detection," *Optics express*, vol. 23, no. 16, pp. 20 686–20 695, 2015.

[44] C. Rau, G. Torosyan, R. Beigang, and K. Nerkararyan, "Prism coupled terahertz waveguide sensor," *Applied Physics Letters*, vol. 86, no. 21, p. 211119, 2005.

[45] G. C. Yadav, S. Prakash, G. Sharma, S. Kumar, and V. Singh, "Performance analysis of a liquid-filled glass prism-coupled metal-clad planar waveguide sensor," *Applied Physics A*, vol. 124, no. 12, p. 840, 2018.

[46] A. Valadez, C. Lana, S.-I. Tu, M. Morgan, and A. Bhunia, "Evanescent wave fiber optic biosensor for salmonella detection in food," *Sensors*, vol. 9, no. 7, pp. 5810–5824, 2009.

[47] H.-q. Yin, R. Xiao, Z. Rong, P.-p. Jin, C.-f. Ji, and J.-g. Zhang, "Establishment of evanescent wave fiber-optic immunosensor method for detection bluetongue virus," *Methods*, vol. 90, pp. 65–67, 2015.

[48] V. Pahurkar, Y. Tamgadge, A. Gambhire, and G. Muley, "Evanescent wave absorption based polyaniline cladding modified fiber optic intrinsic biosensor for glucose sensing application," *Measurement*, vol. 61, pp. 9–15, 2015.

[49] H. Qiu, S. Gao, P. Chen, Z. Li, X. Liu, C. Zhang, Y. Xu, S. Jiang, C. Yang, Y. Huo *et al.*, "Evanescent wave absorption sensor based on tapered multimode fiber coated with monolayer graphene film," *Optics Communications*, vol. 366, pp. 275–281, 2016.

[50] N. Zhong, M. Zhao, L. Zhong, Q. Liao, X. Zhu, B. Luo, and Y. Li, "A high-sensitivity fiber-optic evanescent wave sensor with a three-layer structure composed of canada balsam doped with geo2," *Biosensors and Bioelectronics*, vol. 85, pp. 876–882, 2016.

[51] X. Xin, N. Zhong, Q. Liao, Y. Cen, R. Wu, and Z. Wang, "High-sensitivity four-layer polymer fiber-optic evanescent wave sensor," *Biosensors and Bioelectronics*, vol. 91, pp. 623–628, 2017.

[52] M. Hernáez, I. Del Villar, C. R. Zamarreño, F. J. Arregui, and I. R. Matias, "Optical fiber refractometers based on lossy mode resonances supported by tio 2 coatings," *Applied optics*, vol. 49, no. 20, pp. 3980–3985, 2010.

[53] P. Zubiate, C. Zamarreño, P. Sánchez, I. Matias, and F. Arregui, "High sensitive and selective c-reactive protein detection by means of lossy mode resonance based optical fiber devices." *Biosensors and Bioelectronics*, vol. 93, pp. 176–181, 2017.

[54] C.-L. Tien, H.-Y. Lin, and S.-H. Su, "High sensitivity refractive index sensor by d-shaped fibers and titanium dioxide nanofilm," *Advances in Condensed Matter Physics*, vol. 2018, pp. 1–6, 2018.

[55] F. J. Arregui, I. Del Villar, C. R. Zamarreño, P. Zubiate, and I. R. Matias, "Giant sensitivity of optical fiber sensors by means of lossy mode resonance," *Sensors and Actuators B: Chemical*, vol. 232, pp. 660–665, 2016.

[56] A. Otto, "Excitation of nonradiative surface plasma waves in silver by the method of frustrated total reflection," *Zeitschrift für Physik*, vol. 216, no. 4, pp. 398–410, 1968.

[57] E. Kretschmann and H. Raether, "Notizen: radiative decay of non radiative surface plasmons excited by light," *Zeitschrift für Naturforschung A*, vol. 23, no. 12, pp. 2135–2136, 1968.

[58] J. Zhou, Q. Qi, C. Wang, Y. Qian, G. Liu, Y. Wang, and L. Fu, "Surface plasmon resonance (spr) biosensors for food allergen detection in food matrices," *Biosensors and Bioelectronics*, p. 111449, 2019.

[59] A. A. I. Sina, R. Vaidyanathan, A. Wuethrich, L. G. Carrascosa, and M. Trau, "Label-free detection of exosomes using a surface plasmon resonance biosensor," *Analytical and bioanalytical chemistry*, vol. 411, no. 7, pp. 1311–1318, 2019.

[60] N. Cennamo, L. Zeni, E. Catalano, F. Arcadio, and A. Minardo, "Refractive index sensing through surface plasmon resonance in light-diffusing fibers," *Applied Sciences*, vol. 8, no. 7, p. 1172, 2018.

[61] R. Slavík and J. Homola, "Ultrahigh resolution long range surface plasmon-based sensor," *Sensors and Actuators B: Chemical*, vol. 123, no. 1, pp. 10–12, 2007.

[62] M. Vala, S. Etheridge, J. Roach, and J. Homola, "Long-range surface plasmons for sensitive detection of bacterial analytes," *Sensors and actuators B: Chemical*, vol. 139, no. 1, pp. 59–63, 2009.

[63] O. Krupin, C. Wang, and P. Berini, "Detection of leukemia markers using long-range surface plasmon waveguides functionalized with protein g," *Lab on a Chip*, vol. 15, no. 21, pp. 4156–4165, 2015.

[64] O. Krupin, H. Asiri, C. Wang, R. N. Tait, and P. Berini, "Biosensing using straight long-range surface plasmon waveguides," *Optics express*, vol. 21, no. 1, pp. 698–709, 2013.

[65] P. Ren, O. Krupin, P. Berini, and R. N. Tait, "Fabrication of long range surface plasmon waveguide biosensors in a low-index fluoropolymer," *Journal of Vacuum Science & Technology B, Nanotechnology and Microelectronics: Materials, Processing, Measurement, and Phenomena*, vol. 36, no. 4, p. 042601, 2018.

[66] M. Khodami and P. Berini, "Low detection limits using sandwich and inhibition assays on long-range surface plasmon waveguide biosensors," *Sensors and Actuators B: Chemical*, vol. 273, pp. 1156–1161, 2018.

[67] L. Wang, X.-J. Liu, J. Hao, and L.-Q. Chu, "Long-range surface plasmon resonance sensors fabricated with plasma polymerized fluorocarbon thin films," *Sensors and Actuators B: Chemical*, vol. 215, pp. 368–372, 2015.

[68] O. Krupin, C. Wang, and P. Berini, "Selective capture of human red blood cells based on blood group using long-range surface plasmon waveguides," *Biosensors and Bioelectronics*, vol. 53, pp. 117–122, 2014.

[69] W. R. Wong, S. D. Sekaran, F. R. M. Adikan, and P. Berini, "Detection of dengue ns1 antigen using long-range surface plasmon waveguides," *Biosensors and Bioelectronics*, vol. 78, pp. 132–139, 2016.

[70] H. Shi, Z. Liu, X. Wang, J. Guo, L. Liu, L. Luo, J. Guo, H. Ma, S. Sun, and Y. He, "A symmetrical optical waveguide based surface plasmon resonance biosensing system," *Sensors and Actuators B: Chemical*, vol. 185, pp. 91–96, 2013.

[71] H. Zhang, Y. Chen, X. Feng, X. Xiong, S. Hu, Z. Jiang, J. Dong, W. Zhu, W. Qiu, H. Guan *et al.*, "Long-range surface plasmon resonance sensor based on side-polished fiber for biosensing applications," *IEEE Journal of Selected Topics in Quantum Electronics*, vol. 25, no. 2, pp. 1–9, 2019.

[72] M. Dakss, L. Kuhn, P. Heidrich, and B. Scott, "Grating coupler for efficient excitation of optical guided waves in thin films," *Applied physics letters*, vol. 16, no. 12, pp. 523–525, 1970.

[73] Z. Lai, Y. Wang, N. Allbritton, G.-P. Li, and M. Bachman, "Label-free biosensor by protein grating coupler on planar optical waveguides," *Optics letters*, vol. 33, no. 15, pp. 1735–1737, 2008.

[74] N. Kim, I.-S. Park, and W.-Y. Kim, "Salmonella detection with a direct-binding optical grating coupler immunosensor," *Sensors and Actuators B: Chemical*, vol. 121, no. 2, pp. 606–615, 2007.

[75] P. K. Sahoo, S. Sarkar, and J. Joseph, "High sensitivity guided-mode-resonance optical sensor employing phase detection," *Scientific reports*, vol. 7, no. 1, p. 7607, 2017.

[76] J. Schmid, W. Sinclair, J. García, S. Janz, J. Lapointe, D. Poitras, Y. Li, T. Mischki, G. Lopinski, P. Cheben *et al.*, "Silicon-on-insulator guided mode resonant grating for evanescent field molecular sensing," *Optics express*, vol. 17, no. 20, pp. 18 371–18 380, 2009.

[77] F. Kehl, G. Etlinger, T. E. Gartmann, N. S. Tscharner, S. Heub, and S. Follonier, "Introduction of an angle interrogated, mems-based, optical waveguide grating system for label-free biosensing," *Sensors and Actuators B: Chemical*, vol. 226, pp. 135–143, 2016.

[78] X. Wei and S. M. Weiss, "Guided mode biosensor based on grating coupled porous silicon waveguide," *Optics express*, vol. 19, no. 12, pp. 11 330–11 339, 2011.

[79] P. Kozma, A. Hámori, S. Kurunczi, K. Cottier, and R. Horvath, "Grating coupled optical waveguide interferometer for label-free biosensing," *Sensors and Actuators B: Chemical*, vol. 155, no. 2, pp. 446–450, 2011.

[80] A. Mizutani, S. Urakawa, and H. Kikuta, "Highly sensitive refractive index sensor using a resonant grating waveguide on a metal substrate," *Applied Optics*, vol. 54, no. 13, pp. 4161–4166, 2015.

[81] H.-Y. Li, W.-C. Hsu, K.-C. Liu, Y.-L. Chen, L.-K. Chau, S. Hsieh, and W.-H. Hsieh, "A low cost, label-free biosensor based on a novel double-sided grating waveguide coupler with sub-surface cavities," *Sensors and Actuators B: Chemical*, vol. 206, pp. 371–380, 2015.

[82] M. Paulsen, S. Jahns, and M. Gerken, "Intensity-based readout of resonant-waveguide grating biosensors: Systems and nanostructures," *Photonics and Nanostructures-Fundamentals and Applications*, vol. 26, pp. 69–79, 2017.

[83] G. J. Triggs, Y. Wang, C. P. Reardon, M. Fischer, G. J. Evans, and T. F. Krauss, "Chirped guided-mode resonance biosensor," *Optica*, vol. 4, no. 2, pp. 229–234, 2017.

[84] Y. Takashima, K. Kusaba, M. Haraguchi, and Y. Naoi, "Highly sensitive refractive index sensor using dual resonance in subwavelength grating/waveguide with normally incident optical geometry," *IEEE Sensors Journal*, 2019.

[85] Y. Wu, Y. Meng, B. Yakupoglu, and M. Adams, "A metamaterial/liquid-core waveguide microfluidic optical sensor," *Sensors and Actuators A: Physical*, vol. 300, p. 111592, 2019.

[86] X. Shu, L. Zhang, and I. Bennion, "Sensitivity characteristics of long-period fiber gratings," *Journal of Lightwave Technology*, vol. 20, no. 2, pp. 255–266, 2002.

[87] S. Sridevi, K. Vasu, S. Asokan, and A. Sood, "Sensitive detection of c-reactive protein using optical fiber bragg gratings," *Biosensors and Bioelectronics*, vol. 65, pp. 251–256, 2015.

[88] R. Queirós, C. Gouveia, J. Fernandes, and P. Jorge, "Evanescent wave dna-aptamer biosensor based on long period gratings for the specific recognition of e. coli outer membrane proteins," *Biosensors and Bioelectronics*, vol. 62, pp. 227–233, 2014.

[89] X. Dong, H. Zhang, B. Liu, and Y. Miao, "Tilted fiber bragg gratings: principle and sensing applications," *Photonic Sensors*, vol. 1, no. 1, pp. 6–30, 2011.

[90] C. Lin, C. Liao, J. Wang, J. He, Y. Wang, Z. Li, T. Yang, F. Zhu, K. Yang, Z. Zhang *et al.*, "Fiber surface bragg grating waveguide for refractive index measurements," *Optics letters*, vol. 42, no. 9, pp. 1684–1687, 2017.

[91] S. J. Mihailov, "Ultrafast laser inscribed fiber bragg gratings for sensing applications," in *Fiber Optic Sensors and Applications XIII*, vol. 9852. International Society for Optics and Photonics, 2016, p. 98520P.

[92] A. Bekmurzayeva, K. Dukenbayev, M. Shaimerdenova, I. Bekniyazov, T. Ayupova, M. Sypabekova, C. Molardi, and D. Tosi, "Etched fiber bragg grating biosensor functionalized with aptamers for detection of thrombin," *Sensors*, vol. 18, no. 12, p. 4298, 2018.

[93] L. Marques, F. Hernandez, S. W. James, S. Morgan, M. Clark, R. P. Tatam, and S. Korposh, "Highly sensitive optical fibre long period grating biosensor anchored with silica core gold shell nanoparticles," *Biosensors and Bioelectronics*, vol. 75, pp. 222–231, 2016.

[94] G. Zhu, M. Zhang, L. Lu, X. Lou, M. Dong, and L. Zhu, "Metal-organic framework/enzyme coated optical fibers as waveguide-based biosensors," *Sensors and Actuators B: Chemical*, vol. 288, pp. 12–19, 2019.

[95] F. Esposito, L. Sansone, C. Taddei, S. Campopiano, M. Giordano, and A. Iadicicco, "Ultrasensitive biosensor based on long period grating coated with polycarbonate-graphene oxide multilayer," *Sensors and Actuators B: Chemical*, vol. 274, pp. 517–526, 2018.

[96] B. Jiang, K. Zhou, C. Wang, Q. Sun, G. Yin, Z. Tai, K. Wilson, J. Zhao, and L. Zhang, "Label-free glucose biosensor based on enzymatic graphene oxide-functionalized tilted fiber grating," *Sensors and Actuators B: Chemical*, vol. 254, pp. 1033–1039, 2018.

[97] C. Ribaut, V. Voisin, V. Malachovská, V. Dubois, P. Mégret, R. Wattiez, and C. Caucheteur, "Small biomolecule immunosensing with plasmonic optical fiber grating sensor," *Biosensors and Bioelectronics*, vol. 77, pp. 315–322, 2016.

[98] T. Guo, F. Liu, X. Liang, X. Qiu, Y. Huang, C. Xie, P. Xu, W. Mao, B.-O. Guan, and J. Albert, "Highly sensitive detection of urinary protein variations using tilted fiber grating sensors with plasmonic nanocoatings," *Biosensors and Bioelectronics*, vol. 78, pp. 221–228, 2016.

[99] T. Guo, F. Liu, Y. Liu, N.-K. Chen, B.-O. Guan, and J. Albert, "In-situ detection of density alteration in non-physiological cells with polarimetric tilted fiber grating sensors," *Biosensors and Bioelectronics*, vol. 55, pp. 452–458, 2014.

[100] Y. Ji, Y. Chung, D. Sprinzak, M. Heiblum, D. Mahalu, and H. Shtrikman, "An electronic mach–zehnder interferometer," *Nature*, vol. 422, no. 6930, p. 415, 2003.

[101] B. Luff, J. S. Wilkinson, J. Piehler, U. Hollenbach, J. Ingenhoff, and N. Fabricius, "Integrated optical mach-zehnder biosensor," *Journal of lightwave technology*, vol. 16, no. 4, p. 583, 1998.

[102] T. Yadav, R. Narayanaswamy, M. A. Bakar, Y. M. Kamil, and M. Mahdi, "Single mode tapered fiber-optic interferometer based refractive index sensor and its application to protein sensing," *Optics express*, vol. 22, no. 19, pp. 22 802–22 807, 2014.

[103] M. Janik, M. Koba, A. Celebańska, W. J. Bock, and M. Śmietana, "Live e. coli bacteria label-free sensing using a microcavity in-line mach-zehnder interferometer," *Scientific Reports*, vol. 8, no. 1, p. 17176, 2018.

[104] A. Al-Jawdah, A. Nabok, R. Jarrah, A. Holloway, A. Tsargorodska, E. Takacs, and A. Szekacs, "Mycotoxin biosensor based on optical planar waveguide," *Toxins*, vol. 10, no. 7, p. 272, 2018.

[105] X. Sun, L. Thylén, and L. Wosinski, "Hollow hybrid plasmonic mach–zehnder sensor," *Optics letters*, vol. 42, no. 4, pp. 807–810, 2017.

[106] P. Muellner, E. Melnik, G. Koppitsch, J. Kraft, F. Schrank, and R. Hainberger, "Cmos-compatible si3n4 waveguides for optical biosensing," *Procedia engineering*, vol. 120, pp. 578–581, 2015.

[107] E. Melnik, P. Muellner, G. C. Mutinati, G. Koppitsch, F. Schrank, R. Hainberger, and M. Laemmerhofer, "Local functionalization of cmos-compatible si3n4 mach-zehnder interferometers with printable functional polymers," *Sensors and Actuators B: Chemical*, vol. 236, pp. 1061–1068, 2016.

[108] M. Hofmann, Y. Xiao, S. Sherman, U. Gleissner, T. Schmidt, and H. Zappe, "Asymmetric mach–zehnder interferometers without an interaction window in polymer foils for refractive index sensing," *Applied optics*, vol. 55, no. 5, pp. 1124–1131, 2016.

[109] A. Bastos, C. Vicente, R. Oliveira-Silva, N. Silva, M. Tacão, J. Costa, M. Lima, P. André, and R. Ferreira, "Integrated optical mach-zehnder interferometer based on organic-inorganic hybrids for photonics-on-a-chip biosensing applications," *Sensors*, vol. 18, no. 3, p. 840, 2018.

[110] P. Dumais, C. L. Callender, J. P. Noad, and C. J. Ledderhof, "Integrated optical sensor using a liquid-core waveguide in a mach-zehnder interferometer," *Optics express*, vol. 16, no. 22, pp. 18 164–18 172, 2008.

[111] A. Psarouli, A. Botsialas, A. Salapatas, G. Stefanitsis, D. Nikita, G. Jobst, N. Chaniotakis, D. Goustouridis, E. Makarona, P. S. Petrou *et al.*, "Fast label-free detection of c-reactive protein using broad-band mach-zehnder interferometers integrated on silicon chips," *Talanta*, vol. 165, pp. 458–465, 2017.

[112] K. Misiakos, I. Raptis, A. Salapatas, E. Makarona, A. Botsialas, M. Hoekman, R. Stoffer, and G. Jobst, "Broad-band mach-zehnder interferometers as high performance refractive index sensors: Theory and monolithic implementation," *Optics express*, vol. 22, no. 8, pp. 8856–8870, 2014.

[113] Y. Jung, S. Lee, B. H. Lee, and K. Oh, "Ultracompact in-line broadband mach-zehnder interferometer using a composite leaky hollow-optical-fiber waveguide," *Optics letters*, vol. 33, no. 24, pp. 2934–2936, 2008.

[114] Q. Liu, X. Tu, K. W. Kim, J. S. Kee, Y. Shin, K. Han, Y.-J. Yoon, G.-Q. Lo, and M. K. Park, "Highly sensitive mach–zehnder interferometer biosensor based on silicon nitride slot waveguide," *Sensors and Actuators B: Chemical*, vol. 188, pp. 681–688, 2013.

[115] X. Sun, D. Dai, L. Thylén, and L. Wosinski, "High-sensitivity liquid refractive-index sensor based on a mach-zehnder interferometer with a double-slot hybrid plasmonic waveguide," *Optics express*, vol. 23, no. 20, pp. 25 688–25 699, 2015.

[116] V. Bhardwaj and V. K. Singh, "Fabrication and characterization of cascaded tapered mach-zehnder interferometer for refractive index sensing," *Sensors and Actuators A: Physical*, vol. 244, pp. 30–34, 2016.

[117] X. Tu, J. Song, T.-Y. Liow, M. K. Park, J. Q. Yiying, J. S. Kee, M. Yu, and G.-Q. Lo, "Thermal independent silicon-nitride slot waveguide biosensor with high sensitivity," *Optics express*, vol. 20, no. 3, pp. 2640–2648, 2012.

[118] Y. Xiao, M. Hofmann, Z. Wang, S. Sherman, and H. Zappe, "Design of all-polymer asymmetric mach–zehnder interferometer sensors," *Applied optics*, vol. 55, no. 13, pp. 3566–3573, 2016.

[119] K. Misiakos, I. Raptis, E. Makarona, A. Botsialas, A. Salapatas, P. Oikonomou, A. Psarouli, P. Petrou, S. Kakabakos, K. Tukkiniemi *et al.*, "All-silicon monolithic mach-zehnder interferometer as a refractive index and bio-chemical sensor," *Optics express*, vol. 22, no. 22, pp. 26 803–26 813, 2014.

[120] Y. Xiao, S. A. Mendez, M. Hofmann, M. Gauch, H. Ehlers, D. Ristau, C. Mueller, and H. Zappe, "Sensitivity enhancement of polymeric mach–zehnder interferometers by use of thin high-index films," *Sensors and Actuators A: Physical*, 2017.

[121] T. Chalyan, R. Guider, L. Pasquardini, M. Zanetti, F. Falke, E. Schreuder, R. Heideman, C. Pederzolli, and L. Pavesi, "Asymmetric mach–zehnder interferometer based biosensors for aflatoxin m1 detection," *Biosensors*, vol. 6, no. 1, p. 1, 2016.

[122] R. J. van Gulik, B. M. de Boer, and P. J. Harmsma, "Refractive index sensing using a three-port interferometer and comparison with ring resonators," *IEEE Journal of Selected Topics in Quantum Electronics*, vol. 23, no. 2, pp. 433–439, 2017.

[123] Y. Zheng, T. Lang, T. Shen, and C. Shen, "Simple immunoglobulin g sensor based on thin core single-mode fiber," *Optical Fiber Technology*, vol. 41, pp. 104–108, 2018.

[124] Z. Li, C. Liao, D. Chen, J. Song, W. Jin, G.-D. Peng, F. Zhu, Y. Wang, J. He, and Y. Wang, "Label-free detection of bovine serum albumin based on an in-fiber mach-zehnder interferometric biosensor," *Optics express*, vol. 25, no. 15, pp. 17 105–17 113, 2017.

[125] B.-T. Wang and Q. Wang, "An interferometric optical fiber biosensor with high sensitivity for igg/anti-igg immunosensing," *Optics Communications*, vol. 426, pp. 388–394, 2018.

[126] H. Yu, L. Xiong, Z. Chen, Q. Li, X. Yi, Y. Ding, F. Wang, H. Lv, and Y. Ding, "Ultracompact and high sensitive refractive index sensor based on mach–zehnder interferometer," *Optics and Lasers in Engineering*, vol. 56, pp. 50–53, 2014.

[127] Y. Zhao, Y. Zhang, H.-f. Hu, Y. Yang, M. Lei, and S.-n. Wang, "High-sensitive mach-zehnder interferometers based on no-core optical fiber with large lateral offset," *Sensors and Actuators A: Physical*, vol. 281, pp. 9–14, 2018.

[128] H. Li, H. Li, F. Meng, X. Lou, and L. Zhu, "All-fiber mzi sensor based on seven-core fiber and fiber ball symmetrical structure," *Optics and Lasers in Engineering*, vol. 112, pp. 1–6, 2019.

[129] B. Song, H. Zhang, B. Liu, W. Lin, and J. Wu, "Label-free in-situ real-time dna hybridization kinetics detection employing microfiber-assisted mach-zehnder interferometer," *Biosensors and Bioelectronics*, vol. 81, pp. 151–158, 2016.

[130] X.-R. Dong, X.-Y. Sun, D.-K. Chu, K. Yin, Z. Luo, C. Zhou, C. Wang, Y.-W. Hu, and J.-A. Duan, "Microcavity mach–zehnder interferometer sensors for refractive index sensing," *IEEE Photonics Technology Letters*, vol. 28, no. 20, pp. 2285–2288, 2016.

[131] T. Yoshino, K. Kurosawa, K. Itoh, and T. Ose, "Fiber-optic fabry-perot interferometer and its sensor applications," *IEEE Transactions on Microwave Theory and Techniques*, vol. 30, no. 10, pp. 1612–1621, 1982.

[132] M. Hirsch, D. Majchrowicz, P. Wierzba, M. Weber, M. Bechelany, and M. Jędrzejewska-Szczerska, "Low-coherence interferometric fiber-optic sensors with potential applications as biosensors," *Sensors*, vol. 17, no. 2, p. 261, 2017.

[133] J. Tian, Y. Lu, Q. Zhang, and M. Han, "Microfluidic refractive index sensor based on an all-silica in-line fabry–perot interferometer fabricated with microstructured fibers," *Optics express*, vol. 21, no. 5, pp. 6633–6639, 2013.

[134] S. C. Warren-Smith, R. M. André, J. Dellith, T. Eschrich, M. Becker, and H. Bartelt, "Sensing with ultra-short fabry-perot cavities written into optical micro-fibers," *Sensors and Actuators B: Chemical*, vol. 244, pp. 1016–1021, 2017.

[135] X. Ni, S. Fu, and Z. Zhao, "Thin-fiber-based fabry–pérot cavity for monitoring microfluidic refractive index," *IEEE Photonics Journal*, vol. 8, no. 3, pp. 1–7, 2016.

[136] C. Liao, T. Hu, and D. Wang, "Optical fiber fabry-perot interferometer cavity fabricated by femtosecond laser micromachining and fusion splicing for refractive index sensing," *Optics express*, vol. 20, no. 20, pp. 22 813–22 818, 2012.

[137] B. Xu, Y. Yang, Z. Jia, and D. Wang, "Hybrid fabry-perot interferometer for simultaneous liquid refractive index and temperature measurement," *Optics express*, vol. 25, no. 13, pp. 14 483–14 493, 2017.

[138] H. Zhu, J.-J. He, L. Shao, and M. Li, "Ultra-high sensitivity optical sensors based on cascaded two fabry-perot interferometers," *Sensors and Actuators B: Chemical*, vol. 277, pp. 152–156, 2018.

[139] E. J. Post, "Sagnac effect," *Reviews of Modern Physics*, vol. 39, no. 2, p. 475, 1967.

[140] X. Li, L. V. Nguyen, Y. Zhao, H. Ebendorff-Heidepriem, and S. C. Warren-Smith, "High-sensitivity sagnac-interferometer biosensor based on exposed core microstructured optical fiber," *Sensors and Actuators B: Chemical*, vol. 269, pp. 103–109, 2018.

[141] S. Gao, L.-P. Sun, J. Li, L. Jin, Y. Ran, Y. Huang, and B.-O. Guan, "High-sensitivity dna biosensor based on microfiber sagnac interferometer," *Optics express*, vol. 25, no. 12, pp. 13 305–13 313, 2017.

[142] X.-Z. Wang and Q. Wang, "A high-birefringence microfiber sagnac-interferometer biosensor based on the vernier effect," *Sensors*, vol. 18, no. 12, p. 4114, 2018.

[143] Y. Tian, W. Wang, N. Wu, X. Zou, and X. Wang, "Tapered optical fiber sensor for label-free detection of biomolecules," *Sensors*, vol. 11, no. 4, pp. 3780–3790, 2011.

[144] Q. Liu, S. Li, H. Chen, J. Li, and Z. Fan, "High-sensitivity plasmonic temperature sensor based on photonic crystal fiber coated with nanoscale gold film," *Applied Physics Express*, vol. 8, no. 4, p. 046701, 2015.

[145] Y. Huang, Z. Tian, L.-P. Sun, D. Sun, J. Li, Y. Ran, and B.-O. Guan, "High-sensitivity dna biosensor based on optical fiber taper interferometer coated with conjugated polymer tentacle," *Optics express*, vol. 23, no. 21, pp. 26 962–26 968, 2015.

[146] L.-P. Sun, J. Li, Y. Tan, S. Gao, L. Jin, and B.-O. Guan, "Bending effect on modal interference in a fiber taper and sensitivity enhancement for refractive index measurement," *Optics express*, vol. 21, no. 22, pp. 26 714–26 720, 2013.

[147] A. B. González Guerrero, *Bimodal waveguide interferometer device based on silicon photonics technology for label-free and high sensitive biosensing*. Universitat Autònoma de Barcelona,, 2013.

[148] Y. Liang, M. Zhao, Z. Wu, and G. Morthier, "Bimodal waveguide interferometer ri sensor fabricated on low-cost polymer platform," *IEEE Photonics Journal*, vol. 11, no. 2, pp. 1–8, 2019.

[149] K. E. Zinoviev, A. B. González-Guerrero, C. Domínguez, and L. M. Lechuga, "Integrated bimodal waveguide interferometric biosensor for label-free analysis," *Journal of Lightwave Technology*, vol. 29, no. 13, pp. 1926–1930, 2011.

[150] J. Maldonado, A. B. González-Guerrero, C. Domínguez, and L. M. Lechuga, "Label-free bimodal waveguide immunosensor for rapid diagnosis of bacterial infections in cirrhotic patients," *Biosensors and Bioelectronics*, vol. 85, pp. 310–316, 2016.

[151] Y. Cardona-Maya, A. B. Socorro, I. Del Villar, J. L. Cruz, J. M. Corres, and J. F. Botero-Cadavid, "Label-free wavelength and phase detection based sms fiber immunosensors optimized with cladding etching," *Sensors and Actuators B: Chemical*, vol. 265, pp. 10–19, 2018.

[152] E. Yablonovitch, "Inhibited spontaneous emission in solid-state physics and electronics," *Physical review letters*, vol. 58, no. 20, p. 2059, 1987.

[153] T. Baba, D. Mori, K. Inoshita, and Y. Kuroki, "Light localizations in photonic crystal line defect waveguides," *IEEE Journal of selected topics in quantum electronics*, vol. 10, no. 3, pp. 484–491, 2004.

[154] M. Lee and P. M. Fauchet, "Two-dimensional silicon photonic crystal based biosensing platform for protein detection," *Optics express*, vol. 15, no. 8, pp. 4530–4535, 2007.

[155] V. Toccafondo, J. García-Rupérez, M. Bañuls, A. Griol, J. Castelló, S. Peransi-Llopis, and A. Maquieira, "Single-strand dna detection using a planar photonic-crystal-waveguide-based sensor," *Optics letters*, vol. 35, no. 21, pp. 3673–3675, 2010.

[156] S. Chakravarty, W.-C. Lai, Y. Zou, H. A. Drabkin, R. M. Gemmill, G. R. Simon, S. H. Chin, and R. T. Chen, "Multiplexed specific label-free detection of nci-h358 lung cancer cell line lysates with silicon based photonic crystal microcavity biosensors," *Biosensors and Bioelectronics*, vol. 43, pp. 50–55, 2013.

[157] W. C. Wong, C. C. Chan, J. L. Boo, Z. Y. Teo, Z. Q. Tou, H. B. Yang, C. M. Li, and K. C. Leong, "Photonic crystal fiber surface plasmon resonance biosensor based on protein g immobilization," *IEEE Journal of Selected Topics in Quantum Electronics*, vol. 19, no. 3, pp. 4 602 107–4 602 107, 2013.

[158] N. Skivesen, A. Têtu, M. Kristensen, J. Kjems, L. H. Frandsen, and P. I. Borel, "Photonic-crystal waveguide biosensor," *Optics Express*, vol. 15, no. 6, pp. 3169–3176, 2007.

[159] K. Raman, T. S. Murthy, and G. Hegde, "Fabrication of refractive index tunable polydimethylsiloxane photonic crystal for biosensor application," *Physics Procedia*, vol. 19, pp. 146–151, 2011.

[160] W. Liu, J. Yan, and Y. Shi, "High sensitivity visible light refractive index sensor based on high order mode si 3 n 4 photonic crystal nanobeam cavity," *Optics express*, vol. 25, no. 25, pp. 31 739–31 745, 2017.

[161] K. Aono, S. Aki, K. Sueyoshi, H. Hisamoto, and T. Endo, "Development of optical biosensor based on photonic crystal made of tio2 using liquid phase deposition," *Japanese Journal of Applied Physics*, vol. 55, no. 8S3, p. 08RE01, 2016.

[162] S. Pal, A. R. Yadav, M. A. Lifson, J. E. Baker, P. M. Fauchet, and B. L. Miller, "Selective virus detection in complex sample matrices with photonic crystal optical cavities," *Biosensors and Bioelectronics*, vol. 44, pp. 229–234, 2013.

[163] T. Bolstad, "Fabrication of a silicon photonic crystal biosensor," Master's thesis, Institutt for elektronikk og telekommunikasjon, 2014.

[164] H. Yan, Y. Zou, S. Chakravarty, C.-J. Yang, Z. Wang, N. Tang, D. Fan, and R. T. Chen, "Silicon on-chip bandpass filters for the multiplexing of high sensitivity photonic crystal microcavity biosensors," *Applied physics letters*, vol. 106, no. 12, p. 121103, 2015.

[165] C. Kang, C. T. Phare, Y. A. Vlasov, S. Assefa, and S. M. Weiss, "Photonic crystal slab sensor with enhanced surface area," *Optics express*, vol. 18, no. 26, pp. 27 930–27 937, 2010.

[166] Y. Liu and H. Salemink, "Photonic crystal-based all-optical on-chip sensor," *Optics express*, vol. 20, no. 18, pp. 19 912–19 920, 2012.

[167] Y. Zou, S. Chakravarty, D. N. Kwong, W.-C. Lai, X. Xu, X. Lin, A. Hosseini, and R. T. Chen, "Cavity-waveguide coupling engineered high sensitivity silicon photonic crystal microcavity biosensors with high yield," *IEEE Journal of Selected Topics in Quantum Electronics*, vol. 20, no. 4, pp. 171–180, 2013.

[168] A. Di Falco, L. O'Faolain, and T. Krauss, "Dispersion control and slow light in slotted photonic crystal waveguides," *Applied Physics Letters*, vol. 92, no. 8, p. 083501, 2008.

[169] ——, "Chemical sensing in slotted photonic crystal heterostructure cavities," *Applied physics letters*, vol. 94, no. 6, p. 063503, 2009.

[170] P. Xu, J. Zheng, J. Zhou, Y. Chen, C. Zou, and A. Majumdar, "Multi-slot photonic crystal cavities for high-sensitivity refractive index sensing," *Optics express*, vol. 27, no. 3, pp. 3609–3616, 2019.

[171] D. Yang, H. Tian, and Y. Ji, "Photonic crystal nanoslotted parallel quadrabeam integrated cavity for refractive index sensing with high figure of merit," *Photonics and Nanostructures-Fundamentals and Applications*, vol. 15, pp. 124–129, 2015.

[172] P. B. Deotare, M. W. McCutcheon, I. W. Frank, M. Khan, and M. Lončar, "High quality factor photonic crystal nanobeam cavities," *Applied Physics Letters*, vol. 94, no. 12, p. 121106, 2009.

[173] X. Zhang, G. Zhou, P. Shi, H. Du, T. Lin, J. Teng, and F. S. Chau, "On-chip integrated optofluidic complex refractive index sensing using silicon photonic crystal nanobeam cavities," *Optics letters*, vol. 41, no. 6, pp. 1197–1200, 2016.

[174] Q. Quan, I. B. Burgess, S. K. Tang, D. L. Floyd, and M. Loncar, "High-q, low index-contrast polymeric photonic crystal nanobeam cavities," *Optics express*, vol. 19, no. 22, pp. 22 191–22 197, 2011.

[175] G. A. Rodriguez, P. Markov, A. P. Cartwright, M. H. Choudhury, F. O. Afzal, T. Cao, S. I. Halimi, S. T. Retterer, I. I. Kravchenko, and S. M. Weiss, "Photonic crystal nanobeam biosensors based on porous silicon," *Optics Express*, vol. 27, no. 7, pp. 9536–9549, 2019.

[176] C. Wang, Q. Quan, S. Kita, Y. Li, and M. Lončar, "Single-nanoparticle detection with slot-mode photonic crystal cavities," *Applied Physics Letters*, vol. 106, no. 26, p. 261105, 2015.

[177] B. Wang, M. A. Dündar, R. Nötzel, F. Karouta, S. He, and R. W. van der Heijden, "Photonic crystal slot nanobeam slow light waveguides for refractive index sensing," *Applied Physics Letters*, vol. 97, no. 15, p. 151105, 2010.

[178] Y. Zhang, S. Han, S. Zhang, P. Liu, and Y. Shi, "High-q and high-sensitivity photonic crystal cavity sensor," *IEEE Photonics Journal*, vol. 7, no. 5, pp. 1–6, 2015.

[179] P. Russell, "Photonic crystal fibers," *science*, vol. 299, no. 5605, pp. 358–362, 2003.

[180] A. A. Rifat, F. Haider, R. Ahmed, G. A. Mahdiraji, F. M. Adikan, and A. E. Miroshnichenko, "Highly sensitive selectively coated photonic crystal fiber-based plasmonic sensor," *Optics letters*, vol. 43, no. 4, pp. 891–894, 2018.

[181] G. Amouzad Mahdiraji, D. M. Chow, S. Sandoghchi, F. Amirkhan, E. Dermosesian, K. S. Yeo, Z. Kakaei, M. Ghomeishi, S. Y. Poh, S. Yu Gang *et al.*, "Challenges and solutions in fabrication of silica-based photonic crystal fibers: An experimental study," *Fiber and Integrated Optics*, vol. 33, no. 1-2, pp. 85–104, 2014.

[182] Q. Xie, Y. Chen, X. Li, Z. Yin, L. Wang, Y. Geng, and X. Hong, "Characteristics of d-shaped photonic crystal fiber surface plasmon resonance sensors with different side-polished lengths," *Applied Optics*, vol. 56, no. 5, pp. 1550–1555, 2017.

[183] Y. Chen, Q. Xie, X. Li, H. Zhou, X. Hong, and Y. Geng, "Experimental realization of d-shaped photonic crystal fiber spr sensor," *Journal of Physics D: Applied Physics*, vol. 50, no. 2, p. 025101, 2016.

[184] T. Wu, Y. Shao, Y. Wang, S. Cao, W. Cao, F. Zhang, C. Liao, J. He, Y. Huang, M. Hou *et al.*, "Surface plasmon resonance biosensor based on gold-coated side-polished hexagonal structure photonic crystal fiber," *Optics express*, vol. 25, no. 17, pp. 20 313–20 322, 2017.

[185] A. A. Rifat, R. Ahmed, G. A. Mahdiraji, and F. M. Adikan, "Highly sensitive d-shaped photonic crystal fiber-based plasmonic biosensor in visible to near-ir," *IEEE Sensors Journal*, vol. 17, no. 9, pp. 2776–2783, 2017.

[186] E. Marcatili, "Bends in optical dielectric guides," *Bell Labs Technical Journal*, vol. 48, no. 7, pp. 2103–2132, 1969.

[187] H. Li and X. Fan, "Characterization of sensing capability of optofluidic ring resonator biosensors," *Applied Physics Letters*, vol. 97, no. 1, p. 011105, 2010.

[188] Y. Shin, A. P. Perera, J. S. Kee, J. Song, Q. Fang, G.-Q. Lo, and M. K. Park, "Label-free methylation specific sensor based on silicon microring resonators for detection and quantification of dna methylation biomarkers in bladder cancer," *Sensors and Actuators B: Chemical*, vol. 177, pp. 404–411, 2013.

[189] M. Calvo, S. Guerber, G. Beaudin, M. Canva, P. R. Romeo, C. Baudot, F. Bœuf, P. G. Charette, R. Orobtchouk, and S. Monfray, "Ring resonator designed for biosensing applications manufactured on 300 mm soi in an industrial environment," *Japanese Journal of Applied Physics*, vol. 58, no. SB, p. SBBE02, 2019.

[190] E. Valera, W. W. Shia, and R. C. Bailey, "Development and validation of an immunosensor for monocyte chemotactic protein 1 using a silicon photonic microring resonator biosensing platform," *Clinical biochemistry*, vol. 49, no. 1-2, pp. 121–126, 2016.

[191] S. TalebiFard, S. Schmidt, W. Shi, W. Wu, N. A. Jaeger, E. Kwok, D. M. Ratner, and L. Chrostowski, "Optimized sensitivity of silicon-on-insulator (soi) strip waveguide resonator sensor," *Biomedical optics express*, vol. 8, no. 2, pp. 500–511, 2017.

[192] R. Guider, D. Gandolfi, T. Chalyan, L. Pasquardini, A. Samusenko, G. Pucker, C. Pederzolli, and L. Pavesi, "Design and optimization of sion ring resonator-based biosensors for aflatoxin m1 detection," *Sensors*, vol. 15, no. 7, pp. 17 300–17 312, 2015.

[193] G. A. Rodriguez, S. Hu, and S. M. Weiss, "Porous silicon ring resonator for compact, high sensitivity biosensing applications," *Optics express*, vol. 23, no. 6, pp. 7111–7119, 2015.

[194] X. Tu, S.-L. Chen, C. Song, T. Huang, and L. J. Guo, "Ultrahigh q polymer microring resonators for biosensing applications," *IEEE Photonics Journal*, 2019.

[195] M. K. Park, J. S. Kee, J. Y. Quah, V. Netto, J. Song, Q. Fang, E. M. La Fosse, and G.-Q. Lo, "Label-free aptamer sensor based on silicon microring resonators," *Sensors and Actuators B: Chemical*, vol. 176, pp. 552–559, 2013.

[196] G. Gaur, S. Hu, R. L. Mernaugh, I. I. Kravchenko, S. T. Retterer, and S. M. Weiss, "Label-free detection of herceptin® using suspended silicon microring resonators," *Sensors and Actuators B: Chemical*, vol. 275, pp. 394–401, 2018.

[197] G. Griffel, "Vernier effect in asymmetrical ring resonator arrays," *IEEE Photonics Technology Letters*, vol. 12, no. 12, pp. 1642–1644, 2000.

[198] T. Claes, W. Bogaerts, and P. Bienstman, "Vernier-cascade silicon photonic label-free biosensor with very large sensitivity and low-cost interrogation," in *SPIE NanoScience+ Engineering*. International Society for Optics and Photonics, 2011, pp. 80 990R–80 990R.

[199] Y. Chen, F. Yu, C. Yang, J. Song, L. Tang, M. Li, and J.-J. He, "Label-free biosensing using cascaded double-microring resonators integrated with microfluidic channels," *Optics Communications*, vol. 344, pp. 129–133, 2015.

[200] J. Hu and D. Dai, "Cascaded-ring optical sensor with enhanced sensitivity by using suspended si-nanowires," *IEEE Photonics Technology Letters*, vol. 23, no. 13, pp. 842–844, 2011.

[201] Y. Liu, Y. Li, M. Li, and J.-J. He, "High-sensitivity and wide-range optical sensor based on three cascaded ring resonators," *Optics Express*, vol. 25, no. 2, pp. 972–978, 2017.

[202] Y. Liang, Q. Liu, Z. Wu, G. Morthier, and M. Zhao, "Cascaded-microrings biosensors fabricated on a polymer platform," *Sensors*, vol. 19, no. 1, p. 181, 2019.

[203] Z. Xie, Z. Cao, Y. Liu, Q. Zhang, J. Zou, L. Shao, Y. Wang, J. He, and M. Li, "Highly-sensitive optical biosensor based on equal fsr cascaded microring resonator with intensity interrogation for detection of progesterone molecules," *Optics Express*, vol. 25, no. 26, pp. 33 193–33 201, 2017.

[204] J. Liu, X. Zhou, Z. Qiao, J. Zhang, C. Zhang, T. Xiang, L. Shui, Y. Shi, and L. Liu, "Integrated optical chemical sensor based on an soi ring resonator using phase-interrogation," *IEEE Photonics Journal*, vol. 6, no. 5, pp. 1–7, 2014.

[205] T. Claes, J. G. Molera, K. De Vos, E. Schacht, R. Baets, and P. Bienstman, "Label-free biosensing with a slot-waveguide-based ring resonator in silicon on insulator," *IEEE Photonics journal*, vol. 1, no. 3, pp. 197–204, 2009.

[206] T. Taniguchi, A. Hirowatari, T. Ikeda, M. Fukuyama, Y. Amemiya, A. Kuroda, and S. Yokoyama, "Detection of antibody-antigen reaction by silicon nitride slot-ring biosensors using protein g," *Optics Communications*, vol. 365, pp. 16–23, 2016.

[207] X. Sun, D. Dai, L. Thylén, and L. Wosinski, "Double-slot hybrid plasmonic ring resonator used for optical sensors and modulators," in *Photonics*, vol. 2, no. 4. Multidisciplinary Digital Publishing Institute, 2015, pp. 1116–1130.

[208] S. Shopova, R. Rajmangal, S. Holler, and S. Arnold, "Plasmonic enhancement of a whispering-gallery-mode biosensor for single nanoparticle detection," *Applied Physics Letters*, vol. 98, no. 24, p. 243104, 2011.

[209] M. D. Baaske, M. R. Foreman, and F. Vollmer, "Single-molecule nucleic acid interactions monitored on a label-free microcavity biosensor platform," *Nature nanotechnology*, vol. 9, no. 11, p. 933, 2014.

[210] S. Avino, A. Krause, R. Zullo, A. Giorgini, P. Malara, P. De Natale, H. P. Loock, and G. Gagliardi, "Direct sensing in liquids using whispering-gallery-mode droplet resonators," *Advanced Optical Materials*, vol. 2, no. 12, pp. 1155–1159, 2014.

[211] M. Anderson, E. O'Brien, E. Grayek, J. Hermansen, and H. Hunt, "The detection of helicobacter hepaticus using whispering-gallery mode microcavity optical sensors," *Biosensors*, vol. 5, no. 3, pp. 562–576, 2015.

[212] Y. Luo, X. Chen, M. Xu, Z. Chen, and X. Fan, "Optofluidic glucose detection by capillary-based ring resonators," *Optics & Laser Technology*, vol. 56, pp. 12–14, 2014.

[213] K. H. Kim and X. Fan, "Surface sensitive microfluidic optomechanical ring resonator sensors," *Applied Physics Letters*, vol. 105, no. 19, p. 191101, 2014.

[214] L. Ren, X. Wu, M. Li, X. Zhang, L. Liu, and L. Xu, "Ultrasensitive label-free coupled optofluidic ring laser sensor," *Optics letters*, vol. 37, no. 18, pp. 3873–3875, 2012.

[215] L. Ren, X. Zhang, X. Guo, H. Wang, and X. Wu, "High-sensitivity optofluidic sensor based on coupled liquid-core laser," *IEEE Photonics Technology Letters*, vol. 29, no. 8, pp. 639–642, 2017.

[216] F. Khozeymeh and M. Razaghi, "Characteristics optimization in single and dual coupled silicon-on-insulator ring (disk) photonic biosensors," *Sensors and Actuators B: Chemical*, vol. 281, pp. 998–1008, 2019.

[217] M. Li, X. Wu, L. Liu, X. Fan, and L. Xu, "Self-referencing optofluidic ring resonator sensor for highly sensitive biomolecular detection," *Analytical chemistry*, vol. 85, no. 19, pp. 9328–9332, 2013.

[218] G. Testa, C. Collini, L. Lorenzelli, and R. Bernini, "Planar silicon-polydimethylsiloxane optofluidic ring resonator sensors," *IEEE Photonics Technology Letters*, vol. 28, no. 2, pp. 155–158, 2016.

[219] G. Gao, Y. Zhang, H. Zhang, Y. Wang, Q. Huang, and J. Xia, "Air-mode photonic crystal ring resonator on silicon-on-insulator," *Scientific reports*, vol. 6, p. 19999, 2016.

[220] D. Urbonas, A. Balčytis, K. Vaškevičius, M. Gabalis, and R. Petruškevičius, "Air and dielectric bands photonic crystal microringresonator for refractive index sensing." *Optics Letters*, vol. 41, no. 15, pp. 3655–3658, 2016.

[221] S. M. Lo, S. Hu, G. Gaur, Y. Kostoulas, S. M. Weiss, and P. M. Fauchet, "Photonic crystal microring resonator for label-free biosensing," *Optics express*, vol. 25, no. 6, pp. 7046–7054, 2017.

[222] J. Lao, L. Han, Z. Wu, X. Zhang, Y. Huang, Y. Tang, and T. Guo, "Gold nanoparticle-functionalized surface plasmon resonance optical fiber biosensor: In situ detection of thrombin with 1 nm detection limit," *Journal of Lightwave Technology*, 2018.

[223] K. Qin, S. Hu, S. T. Retterer, I. I. Kravchenko, and S. M. Weiss, "Slow light mach–zehnder interferometer as label-free biosensor with scalable sensitivity," *Optics letters*, vol. 41, no. 4, pp. 753–756, 2016.

[224] R. Sumi, N. D. Gupta, and B. K. Das, "Integrated optical mach-zehnder interferometer with a sensing arm of sub-wavelength grating waveguide in soi," in *2017 IEEE SENSORS*, 2017, pp. 1–3.

[225] A. Khan, O. Krupin, E. Lisicka-Skrzek, and P. Berini, "Mach-zehnder refractometric sensor using long-range surface plasmon waveguides," *Applied Physics Letters*, vol. 103, no. 11, p. 111108, 2013.

[226] X. Jiang, Y. Chen, F. Yu, L. Tang, M. Li, and J.-J. He, "High-sensitivity optical biosensor based on cascaded mach–zehnder interferometer and ring resonator using vernier effect," *Optics letters*, vol. 39, no. 22, pp. 6363–6366, 2014.

[227] S. Schmidt, J. Flueckiger, W. Wu, S. M. Grist, S. T. Fard, V. Donzella, P. Khumwan, E. R. Thompson, Q. Wang, P. Kulik *et al.*, "Improving the performance of silicon photonic rings, disks, and bragg gratings for use in label-free biosensing," in *Biosensing and Nanomedicine VII*, vol. 9166. International Society for Optics and Photonics, 2014, p. 91660M.

[228] H. Yan, L. Huang, X. Xu, S. Chakravarty, N. Tang, H. Tian, and R. T. Chen, "Unique surface sensing property and enhanced sensitivity in microring resonator biosensors based on subwavelength grating waveguides," *Optics express*, vol. 24, no. 26, pp. 29 724–29 733, 2016.

[229] J. Flueckiger, S. Schmidt, V. Donzella, A. Sherwali, D. M. Ratner, L. Chrostowski, and K. C. Cheung, "Sub-wavelength grating for enhanced ring resonator biosensor," *Optics express*, vol. 24, no. 14, pp. 15 672–15 686, 2016.

[230] L. Huang, H. Yan, X. Xu, S. Chakravarty, N. Tang, H. Tian, and R. T. Chen, "Improving the detection limit for on-chip photonic sensors based on subwavelength grating racetrack resonators," *Optics express*, vol. 25, no. 9, pp. 10 527–10 535, 2017.

[231] E. Luan, H. Yun, L. Laplatine, Y. Dattner, D. M. Ratner, K. C. Cheung, and L. Chrostowski, "Enhanced sensitivity of subwavelength multibox waveguide microring resonator label-free biosensors," *IEEE Journal of Selected Topics in Quantum Electronics*, vol. 25, no. 3, pp. 1–11, 2019.

[232] Z. Zhang, G. I. Ng, T. Hu, H. Qiu, X. Guo, W. Wang, M. S. Rouifed, C. Liu, J. Sia, J. Zhou *et al.*, "Mid-infrared sensor based on a suspended microracetrack resonator with lateral subwavelength-grating metamaterial cladding," *IEEE Photonics Journal*, vol. 10, no. 2, pp. 1–8, 2018.

[233] Q. Wang, W. Zhao, B. Wang, H. Hu, and J. Li, "A high sensitivity refractive index sensor based on photonic crystal fibre mach–zehnder interferometer," *Journal of Modern Optics*, vol. 64, no. 16, pp. 1639–1647, 2017.

[234] J.-N. Wang and J.-L. Tang, "Photonic crystal fiber mach-zehnder interferometer for refractive index sensing," *Sensors*, vol. 12, no. 3, pp. 2983–2995, 2012.

[235] Q. Wang, L. Kong, Y. Dang, F. Xia, Y. Zhang, Y. Zhao, H. Hu, and J. Li, "High sensitivity refractive index sensor based on splicing points tapered smf-pcf-smf structure mach-zehnder mode interferometer," *Sensors and Actuators B: Chemical*, vol. 225, pp. 213–220, 2016.

[236] Y. Zhao, X.-g. Li, L. Cai, and Y. Yang, "Refractive index sensing based on photonic crystal fiber interferometer structure with up-tapered joints," *Sensors and Actuators B: Chemical*, vol. 221, pp. 406–410, 2015.

[237] J. E. Betancur-Ochoa, V. P. Minkovich, and Y. J. Montagut-Ferizzola, "Special photonic crystal modal interferometer for highly sensitive biosensing," *Journal of Lightwave Technology*, vol. 35, no. 21, pp. 4747–4751, 2017.

[238] Y. Zhao, F. Xia, and J. Li, "Sensitivity-enhanced photonic crystal fiber refractive index sensor with two waist-broadened tapers," *Journal of Lightwave Technology*, vol. 34, no. 4, pp. 1373–1379, 2016.

[239] L. Melo, G. Burton, P. Kubik, and P. Wild, "Refractive index sensor based on inline mach-zehnder interferometer coated with hafnium oxide by atomic layer deposition," *Sensors and Actuators B: Chemical*, vol. 236, pp. 537–545, 2016.

[240] H. Du, X. Sun, Y. Hu, X. Dong, and J. Zhou, "High sensitive refractive index sensor based on cladding etched photonic crystal fiber mach-zehnder interferometer," *Photonic Sensors*, pp. 1–9, 2019.

[241] W. C. Wong, W. Zhou, C. C. Chan, X. Dong, and K. C. Leong, "Cavity ringdown refractive index sensor using photonic crystal fiber interferometer," *Sensors and Actuators B: Chemical*, vol. 161, no. 1, pp. 108–113, 2012.

[242] T. Wang and M. Wang, "Fabry–pérot fiber sensor for simultaneous measurement of refractive index and temperature based on an in-fiber ellipsoidal cavity," *IEEE Photonics Technology Letters*, vol. 24, no. 19, pp. 1733–1736, 2012.

[243] X. Liu, M. Jiang, Q. Sui, S. Luo, and X. Geng, "Optical fiber fabry–perot interferometer for microorganism growth detection," *Optical Fiber Technology*, vol. 30, pp. 32–37, 2016.

[244] X. Liu, M. Jiang, T. Dong, Q. Sui, and X. Geng, "Label-free immunosensor based on optical fiber fabry–perot interferometer," *IEEE Sensors Journal*, vol. 16, no. 20, pp. 7515–7520, 2016.

[245] D. Wu, Y. Huang, J.-Y. Fu, and G.-Y. Wang, "Fiber fabry–perot tip sensor based on multimode photonic crystal fiber," *Optics Communications*, vol. 338, pp. 288–291, 2015.

[246] Y. Zhao, X.-G. Li, L. Cai, and Y.-N. Zhang, "Measurement of ri and temperature using composite interferometer with hollow-core fiber and photonic crystal fiber," *IEEE transactions on instrumentation and measurement*, vol. 65, no. 11, pp. 2631–2636, 2016.

[247] N. Darwish, D. Caballero, M. Moreno, A. Errachid, and J. Samitier, "Multi-analytic grating coupler biosensor for differential binding analysis," *Sensors and Actuators B: Chemical*, vol. 144, no. 2, pp. 413–417, 2010.

[248] D. Duval, J. Osmond, S. Dante, C. Domínguez, and L. M. Lechuga, "Grating couplers integrated on mach-zehnder interferometric biosensors operating in the visible range," *IEEE Photonics Journal*, vol. 5, no. 2, pp. 3 700 108–3 700 108, 2013.

[249] L. A. Coldren, S. W. Corzine, and M. L. Mashanovitch, *Diode lasers and photonic integrated circuits*. John Wiley & Sons, 2012, vol. 218.

[250] K. Okamoto, *Fundamentals of optical waveguides*. Academic press, 2006.

[251] P. Prabhathan, V. Murukeshan, Z. Jing, and P. V. Ramana, "Compact soi nanowire refractive index sensor using phase shifted bragg grating," *Optics express*, vol. 17, no. 17, pp. 15 330–15 341, 2009.

[252] E. Tolstosheeva, E. Barborini, E. Meyer, M. Shafi, S. Vinati, and W. Lang, "Micropatterning of nanoparticle films by bilayer lift-off," *Journal of Micromechanics and Microengineering*, vol. 24, no. 1, p. 015001, 2013.

[253] V. R. Almeida, Q. Xu, C. A. Barrios, and M. Lipson, "Guiding and confining light in void nanostructure," *Optics letters*, vol. 29, no. 11, pp. 1209–1211, 2004.

[254] M. Yagnyukova, "Modeling, fabrication, and characterization of a bragg slot waveguide with a cavity," Ph.D. dissertation, University of Toronto, 2013.

[255] M. Belt, J. Bovington, R. Moreira, J. F. Bauters, M. J. Heck, J. S. Barton, J. E. Bowers, and D. J. Blumenthal, "Sidewall gratings in ultra-low-loss si 3 n 4 planar waveguides," *Optics express*, vol. 21, no. 1, pp. 1181–1188, 2013.

[256] K. Bescherer, J. A. Barnes, and H.-P. Loock, "Absorption measurements in liquid core waveguides using cavity ring-down spectroscopy," *Analytical chemistry*, vol. 85, no. 9, pp. 4328–4334, 2013.

[257] K. S. Lee, S. Y. Yoon, K. H. Lee, S. B. Kim, H. J. Sung, and S. S. Kim, "Optofluidic particle manipulation in a liquid-core/liquid-cladding waveguide," *Optics express*, vol. 20, no. 16, pp. 17 348–17 358, 2012.

[258] P. Dumais, C. L. Callender, J. P. Noad, and C. J. Ledderhof, "Integrated liquid core waveguides for nonlinear optics," *Applied Physics Letters*, vol. 90, no. 10, p. 101101, 2007.

[259] A. Messica, A. Greenstein, and A. Katzir, "Theory of fiber-optic, evanescent-wave spectroscopy and sensors," *Applied Optics*, vol. 35, no. 13, pp. 2274–2284, 1996.

[260] X. Li, J. Wu, A. Liu, Z. Li, Y. Soew, H. Huang, K. Xu, and J. Lin, "A liquid waveguide based evanescent wave sensor integrated onto a microfluidic chip," *Applied Physics Letters*, vol. 93, no. 19, p. 193901, 2008.

[261] R. Bernini, G. Testa, L. Zeni, and P. M. Sarro, "Integrated optofluidic mach–zehnder interferometer based on liquid core waveguides," *Applied Physics Letters*, vol. 93, no. 1, p. 011106, 2008.

[262] G. Testa, G. Persichetti, P. M. Sarro, and R. Bernini, "A hybrid silicon-pdms optofluidic platform for sensing applications," *Biomedical optics express*, vol. 5, no. 2, pp. 417–426, 2014.

[263] A. Datta, I.-Y. Eom, A. Dhar, P. Kuban, R. Manor, I. Ahmad, S. Gangopadhyay, T. Dallas, M. Holtz, H. Temkin *et al.*, "Microfabrication and characterization of teflon af-coated liquid core waveguide channels in silicon," *IEEE Sensors Journal*, vol. 3, no. 6, pp. 788–795, 2003.

[264] O. J. Schueller, X.-M. Zhao, G. M. Whitesides, S. P. Smith, and M. Prentiss, "Fabrication of liquid-core waveguides by soft lithography," *Advanced Materials*, vol. 11, no. 1, pp. 37–41, 1999.

[265] G. Testa, G. Persichetti, and R. Bernini, "Liquid core arrow waveguides: A promising photonic structure for integrated optofluidic microsensors," *Micromachines*, vol. 7, no. 3, p. 47, 2016.

[266] G. Testa, C. Collini, L. Lorenzelli, and R. Bernini, "Planar silicon-polydimethylsiloxane optofluidic ring resonator sensors," *IEEE Photonics Technology Letters*, vol. 28, no. 2, pp. 155–158, 2015.

[267] C. M. Watts, X. Liu, and W. J. Padilla, "Metamaterial electromagnetic wave absorbers," *Advanced materials*, vol. 24, no. 23, pp. OP98–OP120, 2012.

[268] J. Hao, J. Wang, X. Liu, W. J. Padilla, L. Zhou, and M. Qiu, "High performance optical absorber based on a plasmonic metamaterial," *Applied Physics Letters*, vol. 96, no. 25, p. 251104, 2010.

[269] S. Li, X. Ai, R. Wu, and J. Chen, "Experimental demonstration of a metal–dielectric metamaterial refractive index sensor," *Optics & Laser Technology*, vol. 100, pp. 304–308, 2018.

[270] W. Zhou, K. Li, C. Song, P. Hao, M. Chi, M. Yu, and Y. Wu, "Polarization-independent and omnidirectional nearly perfect absorber with ultra-thin 2d subwavelength metal grating in the visible region," *Optics express*, vol. 23, no. 11, pp. A413–A418, 2015.

[271] J. Lei, B. Ji, and J. Lin, "High-performance tunable plasmonic absorber based on the metal-insulator-metal grating nanostructure," *Plasmonics*, vol. 12, no. 1, pp. 151–156, 2017.

[272] J. Wu, C. Zhou, H. Cao, and A. Hu, "Polarization-dependent and-independent spectrum selective absorption based on a metallic grating structure," *Optics Communications*, vol. 309, pp. 57–63, 2013.

[273] X. D. Hoa, A. Kirk, and M. Tabrizian, "Towards integrated and sensitive surface plasmon resonance biosensors: a review of recent progress," *Biosensors and bioelectronics*, vol. 23, no. 2, pp. 151–160, 2007.

[274] Y. Cui, Y. He, Y. Jin, F. Ding, L. Yang, Y. Ye, S. Zhong, Y. Lin, and S. He, "Plasmonic and metamaterial structures as electromagnetic absorbers," *Laser & Photonics Reviews*, vol. 8, no. 4, pp. 495–520, 2014.

[275] W. Yue, Z. Wang, Y. Yang, L. Chen, A. Syed, K. Wong, and X. Wang, "Electron-beam lithography of gold nanostructures for surface-enhanced raman scattering," *Journal of Micromechanics and Microengineering*, vol. 22, no. 12, p. 125007, 2012.

[276] I. Johnston, D. McCluskey, C. Tan, and M. Tracey, "Mechanical characterization of bulk sylgard 184 for microfluidics and microengineering," *Journal of Micromechanics and Microengineering*, vol. 24, no. 3, p. 035017, 2014.

[277] D. J. Kang, C. M. Song, and D. J. Song, "Junction contraction for a t-shaped microchannel to enhance mixing," *Mechanics Research Communications*, vol. 40, pp. 63–68, 2012.

[278] N. Zhong, X. Zhu, Q. Liao, Y. Wang, R. Chen, and Y. Sun, "Effects of surface roughness on optical properties and sensitivity of fiber-optic evanescent wave sensors," *Applied optics*, vol. 52, no. 17, pp. 3937–3945, 2013.

[279] R. A. Watts, T. W. Preist, and J. R. Sambles, "Sharp surface-plasmon resonances on deep diffraction gratings," *Physical review letters*, vol. 79, no. 20, p. 3978, 1997.

[280] J. Wu, C. Zhou, J. Yu, H. Cao, S. Li, and W. Jia, "Te polarization selective absorber based on metal-dielectric grating structure for infrared frequencies," *Optics Communications*, vol. 329, pp. 38–43, 2014.

Appendix A

Fabrication process

Table A.1: EBL steps for depositing 20 nm Cr on 1×1 cm SOI wafer.

Step 1	Prebaked on the hot plate at 180°C for 90 seconds.
Step 2	70 nm 495 PMMA A2 was spin coated on the wafer at 2500 rpm for 45 seconds.
Step 3	Baked the wafer on the hot plate at 180°C for 5 minutes.
Step 4	72 nm 950 PMMA A2 was spin coated on the wafer at 3000 rpm for 45 seconds.
Step 5	Baked the wafer on the hot plate at 180°C for 5 minutes.
Step 6	Exposure by E-line e-beam lithography at 30 KV: area dose 240 μC/cm^2.
Step 7	Developed the wafer for 70 seconds by using MIBK:IPA=1:3 Developer.

Table A.2: Silicon mold for PDMS channel.

Step 1	Prebaked the wafer in an oven at 90°C for 30 minutes.
Step 2	Transfered the wafer to the HMDS bell jar for 10 minutes.
Step 3	AZ 9245 was spin coated on the wafer at 2200 rpm for 25 seconds.
Step 4	Baked the wafer on the hotplate at 110°C for 90 seconds.
Step 5	Exposure time for 30 seconds on channel 2 of Suss aligner (2 mW/cm^2).
step 6	Developed the wafer for 90 seconds by using 3:1 DI water AZ 400K Developer.

Table A.3: Fabrication of PDMS channel.

Step 1	PDMS base and curing agent were mixed to a ratio of 10:1.
Step 2	Transfered the silicon mold to the TMCS bell jar for 10 minutes.
Step 3	Poured the mixture of PDMS base and curing agent to the mold.
Step 4	Placed the silicon mold in an oven to cure at 80°C for 3 hours.
Step 5	Peeled the PDMS replica away from the silicon mold.
step 6	Diced the PDMS replica into 1cm×1cm PDMS samples.

Table A.4: PDMS sample and Glass sample bonding.

Step 1	Both the glass samples and the PDMS samples were treated by ethanol and blown dry.
Step 2	Aligned under a microscope, made three of the five channels covered by the metamaterial.
Step 3	The assembly was moved to the oven to bake at 80°C for 3 hours.

Table A.5: EBL steps for depositing 80 nm Au on Glass wafer.

Step 1	Prebaked on the hot plate at 180°C for 90 seconds.
Step 2	260nm PMMA A4 was spin coated on the wafer at 2500 rpm for 60 seconds.
Step 3	Baked the wafer on the hot plate at 180°C for 90 seconds.
Step 4	Exposure by E-line e-beam lithography at 20 KV: area dose 150 μC/cm^2.
Step 5	Developed the wafer for 70 seconds by using MIBK:IPA=1:3 Developer.
step 6	Rinse: 20 seconds at IPA.